nature biotechnology

Article

https://doi.org/10.1038/s41587-026-03107-2

High-fidelity intravital imaging of biological dynamics with latent-space-enhanced digital adaptive optics

Received: 7 July 2025

Accepted: 25 March 2026

Published online: 23 April 2026

Check for updates

Yunmin Zeng[1,2,3], Qi Zhang[1,3], Yihong Xiao[4], Shidong Wu[5], Seonghoon Kim[1,3,6], Yunhao Zhang[7], Mingrui Wang[1,3], Yuanlong Zhang[3,8,9], Xinyang Li[3,4], Zhi Lu[2,3,10] ✉, Jiamin Wu[1,3,4,11] ✉ & Qionghai Dai[3,4,11] ✉

Intravital fluorescence microscopy is hampered by optical aberrations arising from heterogeneous distributions of the refractive index. Adaptive optics (AO) methods are either costly and slow, requiring additional hardware, or inaccurate due to lack of wavefront information in multiple angular directions. Here we present a latent-space-enhanced digital AO (LEAO) method that uses wave-optics priors embedded in high-dimensional spatial–angular data and semantically disentangles their representations in the latent space. LEAO achieves more than sixfold higher aberration estimation accuracy than the existing approach (coordinate-based neural representations for computational AO). It also exhibits strong robustness across different system configurations and imaging conditions, achieving almost an order of magnitude higher accuracy than iterative digital AO under extreme conditions such as a low signal-to-noise ratio of 3.4 dB. We experimentally demonstrate that LEAO improves diverse biological observations in vivo, such as large-scale tracking of T cells across an entire lymph node, multiregional neural recording in mouse cortex and long-term monitoring of neutrophil activation, extravasation and clearing through mouse intact skull after traumatic brain injury.

Fluorescence optical microscopy has remained a mainstream technique for probing the intricate and versatile world of cells and tissues, making tremendous contributions to immunology[1], neuroscience[2] and cell biology[3]. However, optical aberration induced by the non-uniform distribution of the refractive index across deep tissues or manufacturing flaws in the optical system leads to the distortion of the light wavefront and the subsequent degradation of imaging performance in fluorescence microscopy[4]. Without proper estimation and correction of the aberration, observations will be hindered and many downstream tasks, such as tracking and spike inference, cannot be accurately performed[5,6].

To correct the distorted wavefront caused by thick tissues, multiple types of adaptive optics (AO) methods have been proposed, commonly categorized into hardware AO, computational AO and the combination of both. Hardware AO uses phase-modulating elements such as deformable mirrors to compensate for aberrations, but this increases the complexity of the optical system, and the deformable mirrors can

[1]Department of Automation, Beijing National Research Center for Information Science and Technology, Tsinghua University, Beijing, China. [2]Department of Psychological and Cognitive Sciences, Tsinghua University, Beijing, China. [3]Institute for Brain and Cognitive Sciences, Tsinghua University, Beijing, China. [4]College of Artificial Intelligence, Tsinghua University, Beijing, China. [5]School of Information Science and Technology, Fudan University, Shanghai, China. [6]Hangzhou Zhuoxi Institute of Brain and Intelligence, Hangzhou, China. [7]Weiyang College, Tsinghua University, Beijing, China. [8]School of Life Science, Tsinghua University, Beijing, China. [9]IDG/McGovern Institute for Brain Research, Tsinghua University, Beijing, China. [10]Zhejiang Hehu Technology, Hangzhou, China. [11]Beijing Visual Science and Translational Eye Research Institute (BERI), Beijing, China. ✉e-mail: luzhi@tsinghua.edu.cn; wujiamin@tsinghua.edu.cn; qhdai@tsinghua.edu.cn

https://doi.org/10.1038/s41587-026-03107-2

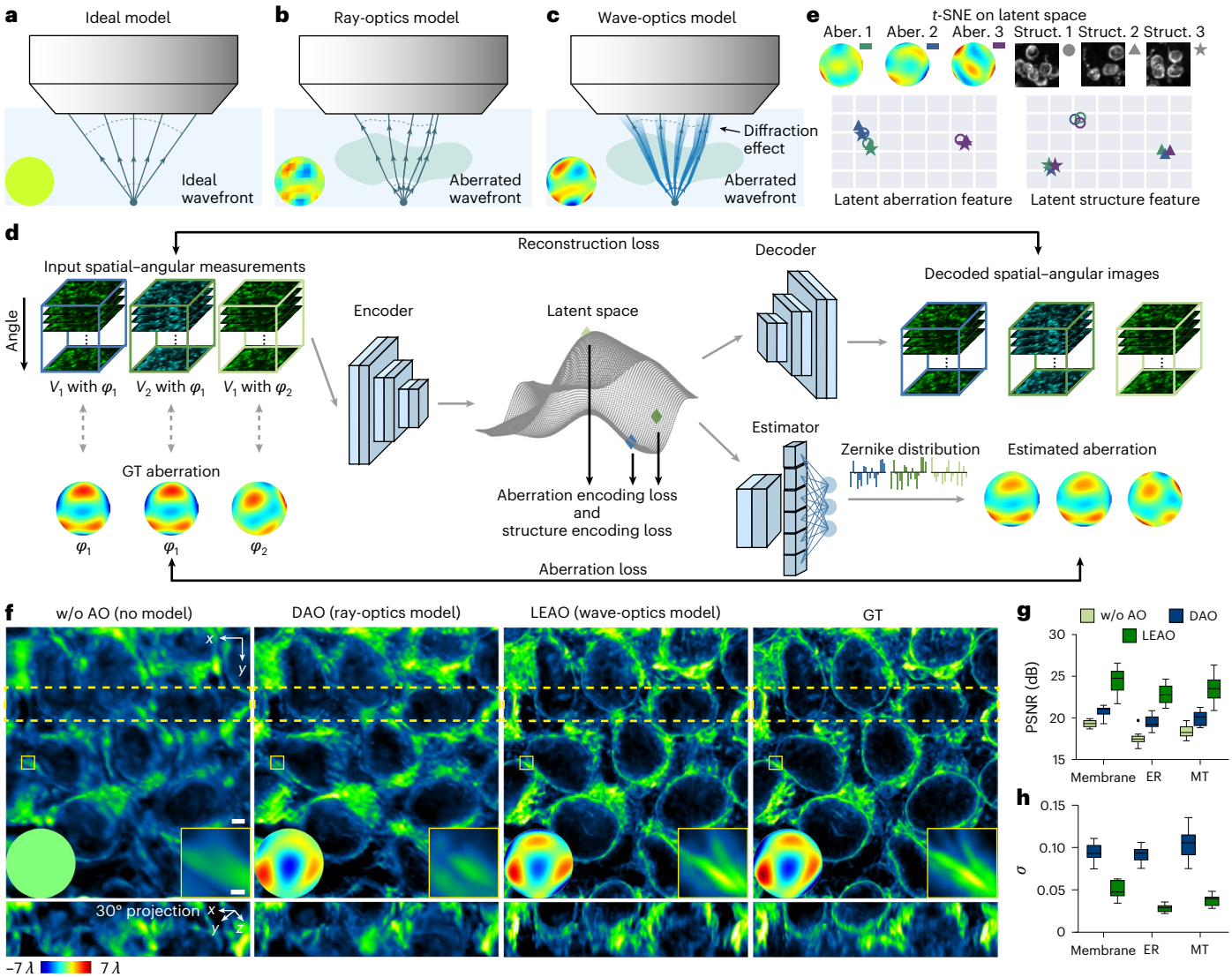

Fig. 1 | Methodology and performance of LEAO. a,**b**,**c**, The ideal model (**a**), ray-optics model (**b**) and wave-optics model (**c**) of imaging wavefronts affected by aberrations. **d**, Framework of LEAO. Through optimization in the latent space using latent loss, feature distances are minimized for inputs sharing the same aberration or structure and maximized for those with different aberrations or structures. **e**, *t*-SNE analysis of latent features extracted from nine measurements, comprising three types of sample structures, each contaminated by three different aberrations. **f**, Two-directional MIPs of endoplasmic reticulum (ER) images without AO (first column), with DAO (second column) and with LEAO (third column). Zoomed-in regions of the yellow solid box are shown at lower-right. Regions corresponding to the 30° projection are marked by a yellow dashed line. Estimated aberration wavefronts are displayed in the insets. The GT image is shown in the right column. **g**, PSNR of images obtained by methods without AO, with DAO and with LEAO on three types of structures including cell membrane, ER and microtubule (MT) ($n = 10$ simulated data stacks for each type of structure). **h**, Normalized residual aberration σ (Methods) estimated by DAO and LEAO ($n = 10$ simulated data stacks for each type of structure). Boxplot format: center line, medians; limits, 75% and 25%; whiskers, the larger value between the largest data point and the 75th percentiles plus 1.5× the interquartile range (IQR) and the smaller value between the smallest data point and the 25th percentiles minus 1.5× the IQR; outliers, data points larger than the upper whisker or smaller than the lower whisker. Scale bars: 20 µm (**f**), 4 µm (zoomed-in regions in **f**). Aber., aberration; Struct., structure; *t*-SNE, *t*-distributed stochastic neighbor embedding; w/o, without.

perform only discrete compensation based on ray optics, leading to decreased accuracy (Supplementary Fig. 1)[7]. Furthermore, during wavefront estimation, direct sensing requires the formation of a 'guide star'[8,9], which may not always be feasible, and indirect sensing without a wavefront sensor[10,11] grows more time-consuming if dealing with higher correction modes and more complicated looping strategies. In contrast to hardware AO, deep learning computational AO approaches[12–15] preserve imaging throughput by deducing the wavefront directly from acquired images and then applying digital compensation during post-processing. Although they require no additional budget or time, these approaches can only deal with small aberrations, typically less than 1 λ, due to a lack of spatial–angular information, which is crucial for decoding wavefront distortion. Recent years have witnessed the emergence of a framework called digital AO (DAO) scanning light-field mutual iterative tomography[16], which synergistically combines hardware-based AO with computational AO methodologies. DAO makes use of light-field microscopy (LFM) spatial–angular data that physically decouple multi-angular information at the hardware level; it algorithmically enables iterative computation of disparities between angular dimensions for aberration estimation. However, it works under simplified ray-optics approximations while neglecting full wave-optics physical models, resulting in limited AO accuracy (Supplementary Fig. 2). A more effective tool is needed to use embedded wave-optics priors in high-dimensional microscopy measurements. Neural networks have

been proven to be capable feature extractors[17–19] and have the potential to characterize physics-aware aberration representations from spatial–angular measurements. Probing the features extracted by deep learning methods can be beneficial for a wide range of tasks, from detecting hidden variables in dynamical systems[20] to identifying semantic disentanglement in single inferotemporal face patch neurons[21].

Here we present LEAO, a latent-space-enhanced digital AO method in which an autoencoder is employed to utilize physical priors embedded in LFM spatial–angular measurements and represent them as high-dimensional features in the latent space while preserving wave-optics properties. A customized latent loss is then applied to encourage the disentangling of latent features encoding structural information and aberration wavefronts, the latter of which can be individually decoded by a well-designed estimator. After the joint optimization of the autoencoder and estimator by iterative training, our method is able to accurately estimate aberrations encoded in spatial–angular measurements. Comprehensive simulations confirmed that our method achieved accuracy at least six times higher than a representative deep-learning-based approach, coordinate-based neural representations for computational AO (CoCoA)[12], in cases with a large aberration magnitude from 1 λ to 5 λ. Another advantage of LEAO is its strong robustness in various challenging conditions. In the presence of Gaussian noise and photon shot noise, LEAO can tolerate a fluorescence photon count three times lower than DAO, with uncompromised aberration estimation accuracy until the signal-to-noise ratio (SNR) drops below 3.4 dB. The performance of LEAO is stable with different spatial sampling rates and across five different system modalities, covering almost all light-field-based systems. LEAO also shows stability to different angle numbers of spatial–angular measurements, with more than one order of magnitude fewer fluctuations than DAO. Experimental results further demonstrated LEAO's capability to restore high-quality images from aberration contamination. LEAO enabled high-fidelity recording and tracking of around 5,000 T cells simultaneously across an entire mouse lymph node. After the correction of spatially non-uniform aberrations by LEAO, mesoscale analysis of multiregional neural activities was achieved with consistent accuracy at the cortex-wide level. Moreover, we applied LEAO on through-intact-skull (TIS) imaging, which allows for non-invasive visualization of the mouse brain without introducing additional, uncontrolled damage that disrupts the experimental design[22,23]. After correction, we observed long-term, sophisticated processes of neutrophil activation in bone marrow, extravasation outside blood vessels and large-scale influx into the major venous sinus through the intact skull of mice challenged with traumatic brain injury (TBI), which was impossible by previous means due to severe aberrations.

Results

Principle of LEAO

Ideally, with a spatially uniform refractive index, fluorescence emitted from a point source forms a spherical wavefront (Fig. 1a). However, in the presence of refractive index inhomogeneities, light rays emitted at different angles undergo deflections, which can be partially corrected by hardware AO or LFM with DAO, using a Shack–Hartmann sensor or microlens array to collect light and estimate the wavefront based on a simplified geometric ray-optics model (Fig. 1b). The estimated wavefront at the objective pupil plane is essentially treated as an approximation of the discrete angular components based on pupil segmentation[16]. However, this model neglects the diffraction effect in light propagation, which becomes dominant at the micrometer scale. Wave-optics theory should be taken into consideration to accurately reconstruct a continuous aberration wavefront (Fig. 1c).

A straightforward approach is to train a neural network that maps raw spatial–angular measurements directly to the aberration wavefront, implicitly encoding the wave-optics prior in a large training set (Supplementary Fig. 3a). However, this vanilla regressor yields inaccurate aberration estimations and is unstable to changes in sample structure because it fails to explicitly represent the physical priors required for reliable correction and discard unwanted information that impedes accurate estimation. To better utilize wave-optics features, the proposed LEAO encodes spatial–angular measurements into a high-dimensional latent space using a well-designed encoder[24,25] (Fig. 1d and Supplementary Video 1). We crafted an encoder–decoder architecture to project physical priors into the latent space, where features that represent the aberration wavefront and the sample structure can potentially be disentangled, reducing the variance of the estimated aberration when the sample structure changes (Supplementary Fig. 3b–e)[26–28]. An estimator operating on the refined latent space then outputs an accurate aberration wavefront, further aided by a dedicated latent loss computed on data triplets that pulls together similar features and pushes apart dissimilar ones during the iterative training (Supplementary Fig. 3f–h). Collectively, these modules constitute the full network architecture of LEAO (Supplementary Fig. 4). Therefore, in the latent manifold encoding aberrations, features corresponding to the same aberration form a distinct cluster; in the manifold encoding sample structures, features associated with the same structural patterns form another (Fig. 1e and Supplementary Fig. 3i). The recovered wavefront is finally applied at the objective pupil to regenerate wave-optics point spread functions (PSFs), which are incorporated into the three-dimensional (3D) reconstruction[29], thereby generating high-resolution volumes with improved fidelity (Supplementary Figs. 3j,k and 5a).

We experimentally evaluated the performance achieved by methods without AO, with DAO and with LEAO on spatial–angular measurements of diverse biological structures (Fig. 1f–h and Supplementary Fig. 6). Results without AO exhibited severe structural distortion and blurring due to uncorrected aberrations. DAO only partially recovered structural details due to limited aberration estimation accuracy. In contrast, LEAO produced the reconstructions with high fidelity and contrast, comparable to the ground truth (GT). Statistical analysis further confirmed that LEAO achieved an aberration estimation accuracy at least two times higher than DAO, along with superior reconstruction performance across multiple biological structures.

Fig. 2 | LEAO achieved superior aberration estimation accuracy across a wide aberration range and maintained robust performance on different SNRs, angle numbers, sampling frequencies and imaging modalities. a, Results of CoCoA, DAO and LEAO with aberration RMS of 1 λ and 2 λ. Regions corresponding to the 30° projection are marked by a yellow dashed line. **b**, GT (two-directional MIPs). **c**, Aberration wavefronts estimated by CoCoA, DAO, LEAO and GT for aberration RMS from 1 λ to 5 λ. **d**, Normalized residual aberration σ and SSIM evaluation (n = 10 data stacks). Line, mean value. Shade, s.d. **e**, MIPs by DAO and LEAO with SNRs = 8.9 dB and 12.1 dB. Estimated aberration wavefronts are shown in insets, with GT at lower-right. **f**, Enlarged images of the marked area in **e**. **g**, PSNR and σ evaluation comparing LEAO and DAO at different SNRs (n = 10 data stacks). **h**, Two-directional MIPs by DAO, LEAO and GT at DAO's optimal angle number of 43. Aberration wavefronts are shown in insets. **i**, σ and SSIM of LEAO and DAO on the sample in **h** at different angle numbers. **j**, σ and SSIM on a larger dataset (n = 10 data stacks). **k**, Concatenated MIPs by LEAO and GT on data with sampling rate of 9.5 μm and 3.2 μm. **l**, PSNR and σ of LEAO at different sampling rates (n = 10 data stacks). **m**, Aberration wavefronts estimated by LEAO and DAO on different spatial–angular modalities with simulated neurons (Data Availability). **n**, σ and SSIM evaluation comparing LEAO and DAO on different spatial–angular modalities (n = 10 data stacks). Boxplot format: center line, medians; limits, 75% and 25%; whiskers, the larger value between the largest data point and the 75th percentiles plus 1.5× IQR and the smaller value between the smallest data point and the 25th percentiles minus 1.5× IQR; outliers, data points larger than the upper whisker or smaller than the lower whisker. Scale bars: 20 μm (**a**,**b**,**e**,**h**,**k**), 8 μm (**f**). 2pSAM, two-photon synthetic aperture microscopy; csLFM, confocal sLFM.

https://doi.org/10.1038/s41587-026-03107-2

Benchmarking of LEAO

Conventional AO methods suffer from performance degradation in intravital microenvironments. We present comprehensive benchmarking experiments with LEAO under simulated in vivo scenarios including variations in aberration magnitude, noise level, angle number and sampling frequency across different LFM modalities, demonstrating its superiority and robustness enabled by the wave-optics-based latent-space-enhanced design.

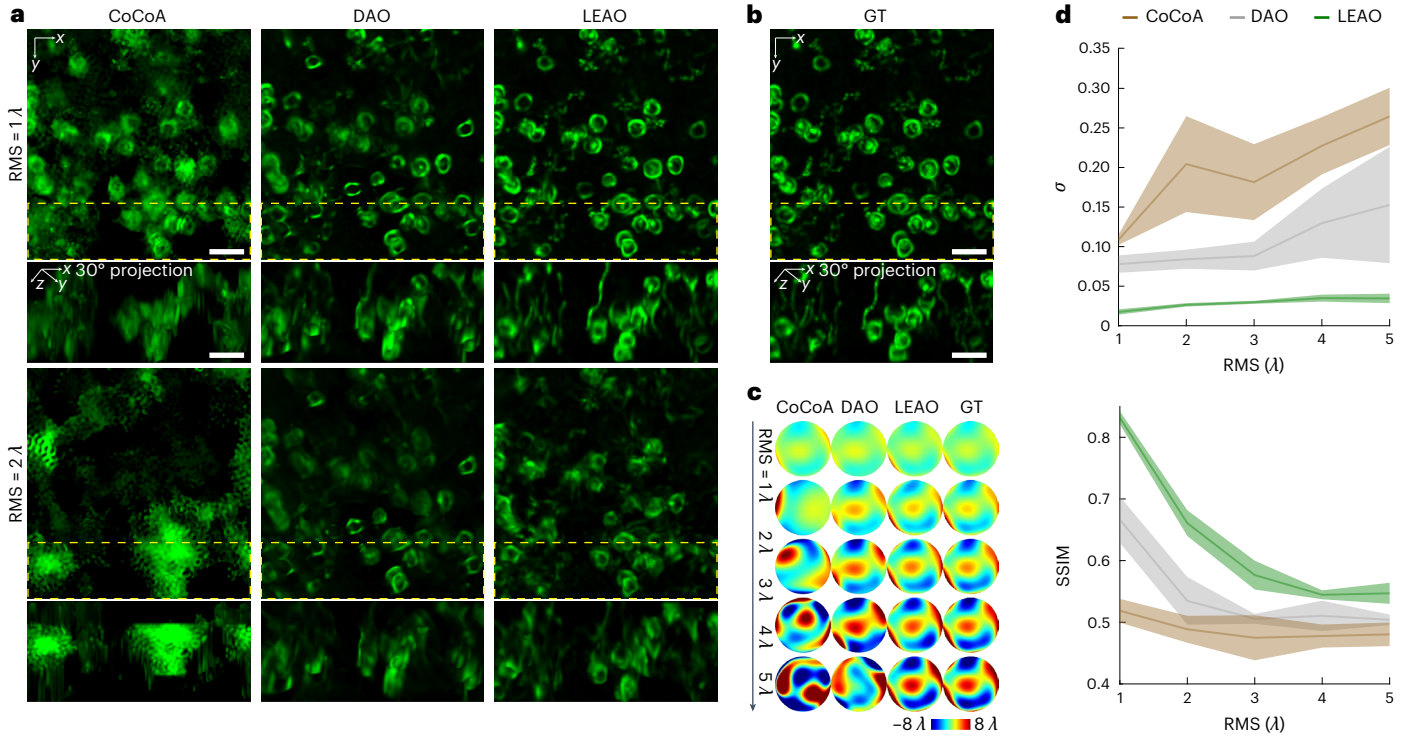

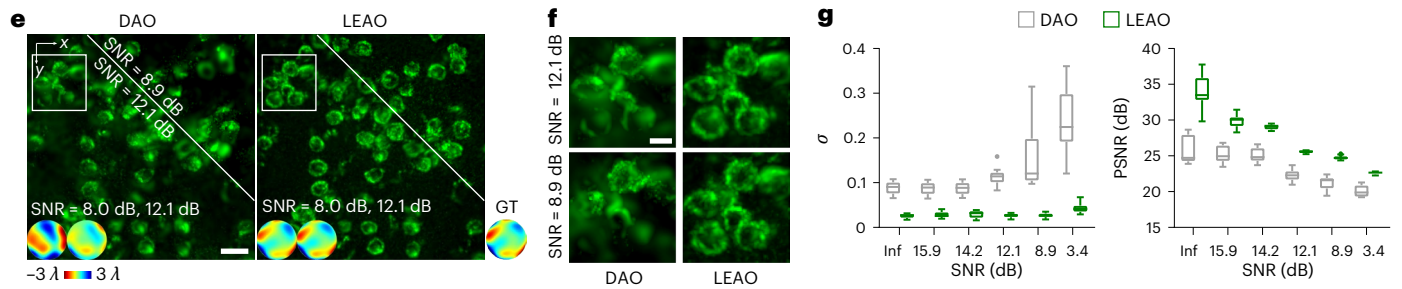

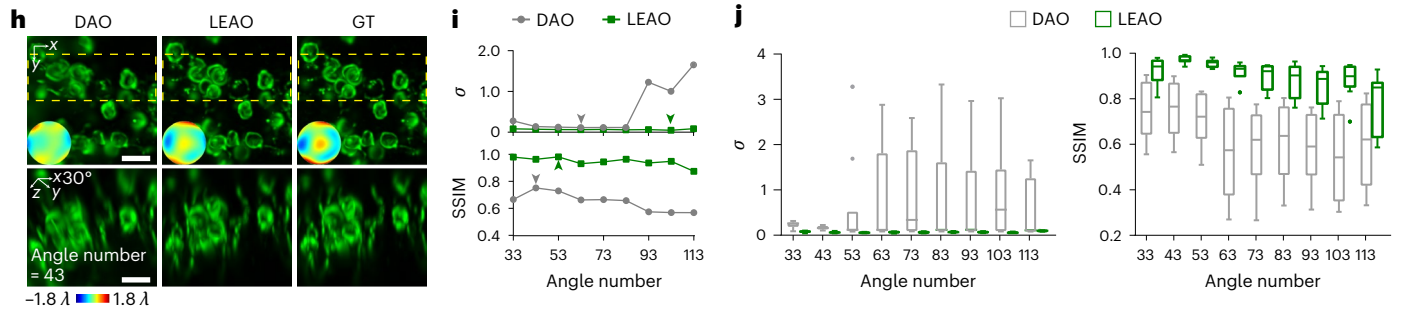

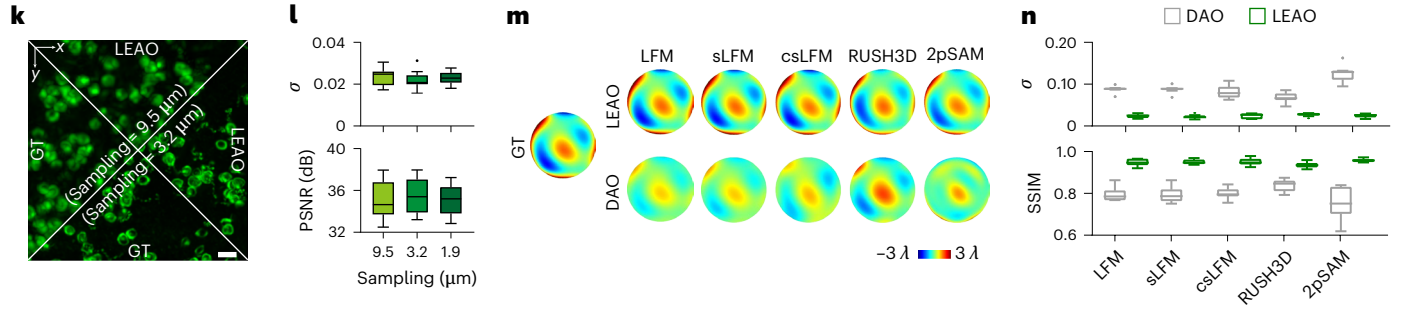

https://doi.org/10.1038/s41587-026-03107-2

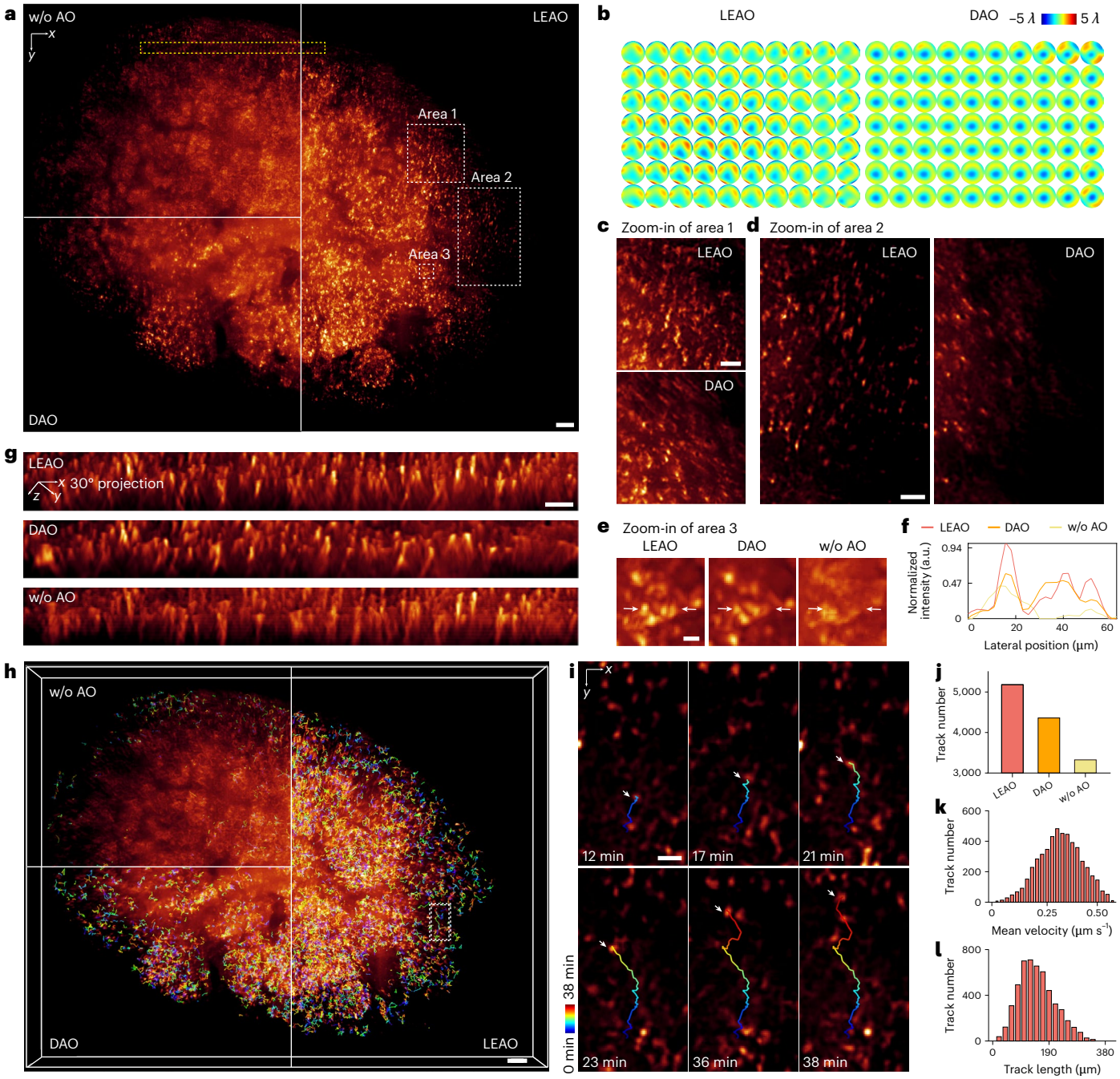

Fig. 3 | LEAO enables high-resolution imaging of approximately 5,000 T cells across an entire mouse lymph node. a, MIP of T cells in a 4 × 3 mm² mouse lymph node with LEAO, with DAO and without AO. **b**, Estimated aberration wavefronts for LEAO and DAO. The whole FOV was divided into 10 × 7 tiles. **c**–**e**, Enlarged images of the areas marked by white dashed box in **a**: area 1 (**c**), area 2 (**d**), area 3 (**e**). **f**, Intensity profiles along the lines marked by white arrow in **e**. LEAO can separate adjacent T cells distorted by aberration with higher peak values, whereas DAO and without AO reconstructions cannot. **g**, Directional MIPs of the area marked by yellow dashed box in **a**. **h**, Color-coded temporal tracks of T cells across a duration of 38 min estimated from results with LEAO, with DAO and without AO. **i**, A representative trajectory of a single cell from LEAO, overlaid on the timelapse MIPs. The region is marked by white dashed box in **h**. **j**, Identified trajectory number obtained by the methods with LEAO, with DAO and without AO. **k**,**l**, Histogram of track mean velocity (**k**) and track length (**l**) obtained by LEAO. Scale bars: 140 μm (**a**,**h**), 70 μm (**c**,**d**,**g**,**i**), 20 μm (**e**).

Large aberrations arising from thick biological samples with inhomogeneous refractive indices remain an undesirable threat to fluorescence imaging in mammals, such as the imaging of immune cells in lymph nodes or information flow in the mouse cortex[30,31]. Conventional AO approaches such as DAO often yield inaccurate aberration estimations due to the limitations of ray-optics-based modeling (Supplementary Fig. 2), and other computational approaches such as CoCoA are efficient only when dealing with small aberrations, typically less than 1 λ. LEAO rises to this extreme case and shows reliable performance by effectively processing a wide range of aberration magnitudes ranging from 1 λ to 5 λ (Fig. 2a–d and Supplementary Fig. 7). In this simulation, we applied aberrations with fixed magnitude but random distribution (Methods) on 3D neural imaging and evaluated the resulting reconstructions. The same optical system parameters were used for wide-field imaging (CoCoA) and light-field imaging (DAO, LEAO) with minimal adaptations. LEAO consistently produced high-fidelity

structural details with finer contrast resembling the GT, even in cases where the aberrations were too severe for CoCoA to recover meaningful content (Fig. 2a,b). Across all levels of input aberration magnitudes, LEAO achieved residual aberration values at least six times lower than those of CoCoA and three times lower than those of DAO and maintained superior image quality (Fig. 2c,d). In addition, empowered by wave-optics priors, LEAO can maintain robust aberration estimation even under unknown aberration magnitudes. When trained on datasets with multilevel aberration magnitudes, it avoids the performance drop seen in single-level models when facing mismatched aberration levels. This generalizability makes LEAO well-suited for intravital data with complex, unpredictable aberrations (Supplementary Fig. 8).

Environmental perturbations, flaws in detection sensors and the stochastic nature of photon emission inevitably introduce noise into fluorescence microscopy[32,33], which degrades the performance of AO methods. We evaluated LEAO under progressively lower peak photon counts in the presence of mixed Poisson and Gaussian noise (Methods) and calculated the SNR of each peak photon count for easier understanding (Fig. 2e–g and Supplementary Fig. 9). Although DAO exhibited markedly higher residual aberrations at 12.1 dB, leading to blurred, distorted reconstructions (Fig. 2e,f), LEAO maintained high aberration estimation accuracy, with a slight drop at 3.4 dB (Fig. 2g), demonstrating a threefold tolerance improvement in low fluorescence photon count compared to DAO. In terms of image quality, LEAO achieved the same peak SNR (PSNR) at 8.9 dB as DAO on clean data. Moreover, LEAO was insensitive to random noise patterns (Supplementary Fig. 10). We applied random noise of the same level on a clean sample repeatedly, producing ten noisy samples. LEAO produced outputs with minimal variance across these trials, all closely resembling the reconstruction from the clean input.

Different imaging configurations lead to different angle numbers for LFM measurements. Even within one configuration, due to factors such as severe aberrations or misalignment of optical components, using either too many or too few angular images negatively impacts the aberration estimation (Supplementary Fig. 11a)[34]. Therefore, identifying the optimal angle number becomes a critical yet labor-intensive task. In DAO's ray-optics-based modeling, aberration estimation is highly sensitive to the number of angular views. LEAO overcomes this limitation by fully incorporating wave-optics modeling and latent space into its design, ensuring robust performance across varying angular configurations (Fig. 2h–j and Supplementary Fig. 11b–d). DAO required different optimal angle numbers for different samples, resulting in large variance in residual aberration and structural similarity (SSIM). In contrast, LEAO remained consistent across all angle numbers with orders-of-magnitude fewer fluctuations, except for a slight performance drop at an angle number of 113 due to degraded quality at the pupil edge (Fig. 2j). Even at DAO's optimal configuration, LEAO delivered superior reconstruction with a cleared background, more accurate structure and finer details, such as thin dendrites (Fig. 2h,i).

In addition, different spatial–angular imaging systems exhibit varying spatial sampling rates, which poses challenges for deep-learning-based methods. Unlike conventional neural networks relying on brute-force fitting, LEAO exploits a latent-space-enhanced design, enabling accurate aberration estimation and high-fidelity structural recovery across a wide range of sampling rates. Specifically, we evaluated LEAO on LFM data with a spatial sampling rate of 9.5 µm, 3.2 µm and 1.9 µm. Quantitative results demonstrate that LEAO remained robust to variations in spatial sampling without imposing stringent requirements on measurement resolution (Fig. 2k,l and Supplementary Fig. 12).

We also validated LEAO's compatibility with various spatial–angular modalities, ranging from one-photon to two-photon systems and spanning different fields of view (FOVs), including traditional LFM[35], scanning LFM (sLFM)[16], confocal sLFM[36], real-time ultralarge-scale high-resolution 3D mesoscope (RUSH3D)[37] and two-photon synthetic aperture microscopy[38]. LEAO consistently outperformed DAO in aberration estimation accuracy across all modalities, demonstrating stable and robust performance (Fig. 2m,n).

Moreover, to validate the fidelity of LEAO on experimentally captured biological data, we set up a system with removable phase masks and conducted experiments with thin mouse brain slices (Methods). By inserting the phase mask, we were able to introduce artificially designed aberrations. LEAO was demonstrated to estimate accurate aberration wavefronts from brain slices contaminated by induced aberrations and restore comparable image quality to the GT captured without aberration (Supplementary Fig. 13). Furthermore, *t*-distributed stochastic neighbor embedding analysis on the latent space validated the disentanglement of LEAO on experimental data (Supplementary Fig. 14).

Demonstration of LEAO on large-scale T cell tracking across an entire mouse lymph node

High-fidelity mesoscale observation of immune cells is fundamental for immunology[30,39]. In particular, visualizing the spatial distribution and dynamics of T cells, which play central roles in pathogen recognition, formation of immunological memory and regulation of autoimmunity, can unveil key mechanisms of immune responses. However, attempts to track the dynamic movements of T cells across the entire mouse lymph node face substantial challenges. Although we previously developed RUSH3D[37] for mesoscale imaging, large aberrations caused by peripheral degradation in the expanded FOV and the tissue thickness severely reduce image quality and prevent us from gaining further understanding of the lymph node as a whole. Conventional AO methods fall short due to their reliance on a ray-optics-based model, which treats each angular measurement as a discrete segment of the wavefront and neglects diffraction effects during light propagation, limiting the resolution of aberration estimation. In contrast, the proposed LEAO addresses these limitations by integrating a wave-propagation model with latent-space-enhanced feature extraction and disentanglement.

To demonstrate this, we tested LEAO on real intravital data acquired using RUSH3D, capturing the large-scale dynamics of T cells across an entire mouse lymph node over an FOV of 4 mm × 3 mm (Fig. 3a). The whole FOV was divided into 10 × 7 tiles (Fig. 3b). Trained on datasets with random aberrations, LEAO accurately corrected the aberration across the imaging volume, enabling a more reliable and higher-contrast observation of mesoscale cell populations (Supplementary Video 2). Specifically, the results without AO exhibited elongated cell bodies and severe contrast loss. DAO partially alleviated distortions but often

Fig. 4 | LEAO enables high-fidelity mesoscale recording of multiregional neural activities in mouse cortex with spatially non-uniform aberrations. **a**, MIPs of the s.d. volume of a 4.6 × 3.4 × 0.6 mm^3 mouse cortex with LEAO, with DAO and without AO. **b**, Regions of the area marked by white box I in **a**, displayed as two-directional MIPs. **c**, Estimated aberration wavefronts by DAO and LEAO on the 10 × 7 spatial tiles and by LEAO (untiled) on the whole FOV. **d**, The representative neuronal patterns from different spatial regions processed without AO, with LEAO (untiled) and with LEAO. **e**, Enlarged regions of the area marked by white boxes II and III in **a**. The regions marked by red line in area II correspond to the right-bottom regions marked by red line in **d**. The regions marked by a yellow line in area III correspond to the central regions marked by a yellow line in **d**. Aberration wavefronts are shown in the insets. **f**, Two-directional MIPs of s.d. volumes over a time of 1,122.5 s, obtained by methods without AO and with LEAO, respectively. Five neurons are manually selected and marked by white arrows. Estimated aberration wavefronts, corresponding Fourier spectrums and enlarged regions are shown in the insets. **g**, $\triangle F/F$ traces of the neurons in **f**. **h**, Neuron number from the area in **f** identified by the CNMF algorithm. **i**, Histogram of extracted spikes from the area in **f** by the CNMF algorithm. **j**, All neuronal traces extracted from the area in **f**. Scale bars: 140 µm (**a**,**b**,**e**,**f**), 40 µm (**d**, zoom-in regions in **b**,**f**).

https://doi.org/10.1038/s41587-026-03107-2

failed or introduced artifacts in regions with exceptionally large and complex aberrations due to inaccurate estimations (Fig. 3c–e). By comparison, LEAO consistently provided better contrast and resolution, especially near the FOV boundaries where DAO showed minimal improvement. Intensity profiles at one such peripheral area revealed that LEAO successfully restored and separated blurred cells that could not be resolved previously, greatly enhancing the spatial resolution and contrast (Fig. 3f). Improvements were also evident along the axial direction (Fig. 3g). Enhanced visual quality contributed to the locating and tracking of T cell activities (Fig. 3h,i). Large-scale statistical analysis of more than 5,000 trajectories in terms of velocity and track length was performed with confidence (Fig. 3j–l). Therefore, LEAO facilitates high-accuracy aberration estimation and subsequent high-fidelity reconstruction for in vivo fluorescence imaging.

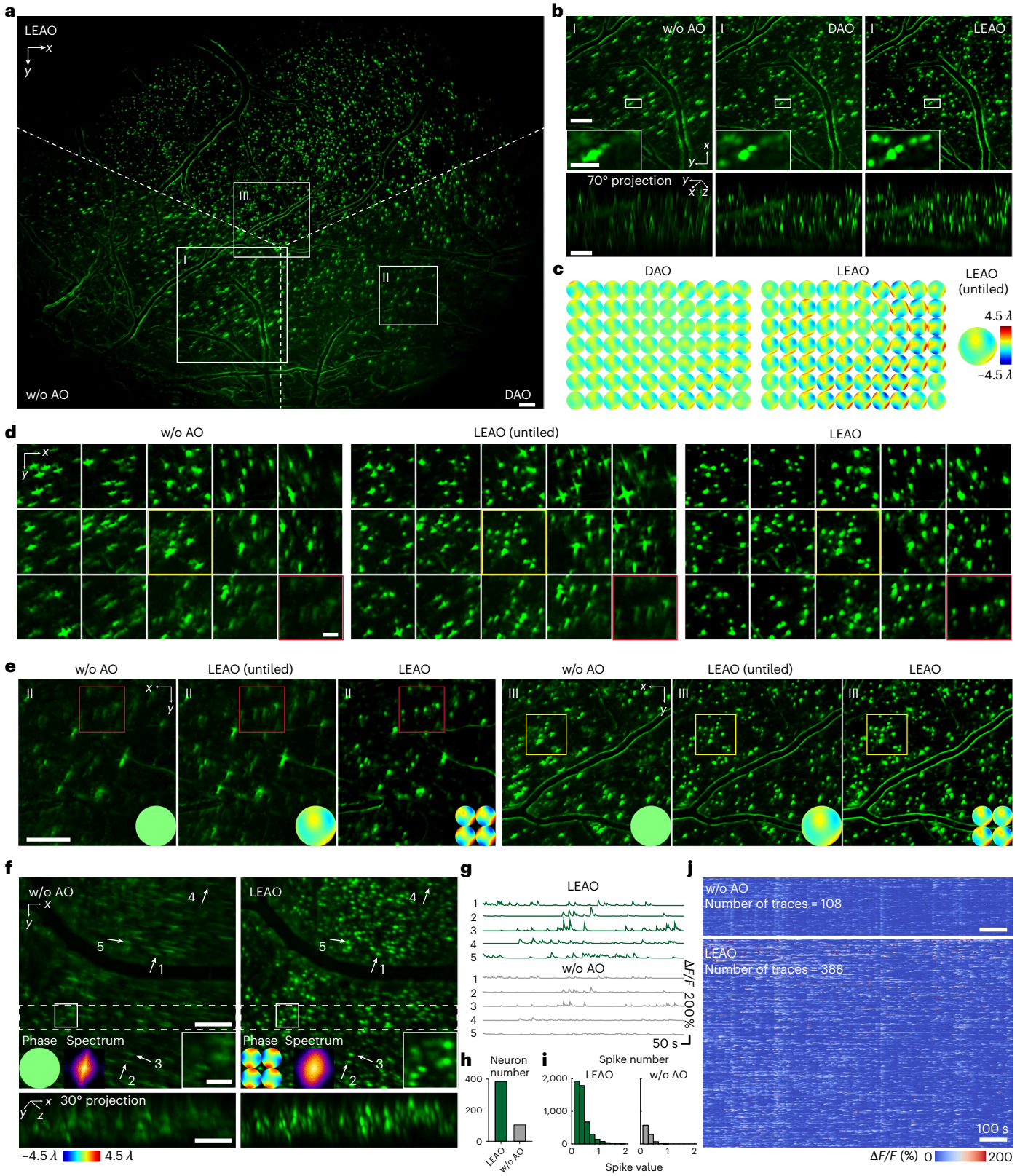

High-fidelity mesoscale analysis of multiregional neural activities by spatially varying LEAO

Here we demonstrated LEAO's ability to accurately compensate for large spatially varying aberrations across mouse brain cortex with an FOV of 4.6 × 3.4 mm^2 (Supplementary Video 3). Severe distortion and loss of spatial resolution were caused by the presence of large aberrations. To achieve accurate correction, the full FOV was divided into 10 × 7 tiles, within which the aberration could be assumed to be approximately uniform. Enhanced by the latent-space-distilled wave-optics aberration information, LEAO successfully restored the spatial resolution both laterally and axially, whereas DAO failed, especially in peripheral regions (Fig. 4a–c). When treating the entire FOV as a whole, untiled LEAO still performed well in the central tile. However, in edge tiles, the reconstruction quality declined due to a mismatch between the estimated aberration and the actual aberration (Fig. 4d,e). Correction of spatially varying aberrations allowed for high-fidelity recording of neural activity and subsequent calcium signal analysis. Compared to the results without aberration correction, LEAO enabled higher spatial resolution and contrast, revealing clear neuronal morphology (Fig. 4f). Neural activities were extracted from a continuous recording over 1,000 s (Methods). Before aberration correction, neurons appeared enlarged and distorted, with many overlapping and merging or fading into the background due to poor contrast. After applying LEAO, neuronal positions and contours were effectively restored. As a result, temporal traces of representative neurons by LEAO showed higher peaks, with a more than threefold increase in the number of detectable neurons (Fig. 4g,h). LEAO also enabled more identified spikes and higher amplitudes (Fig. 4i,j). Comparison of LEAO estimation results on two mice imaged by the same system confirmed that the aberrations were mainly sample-induced (Supplementary Fig. 15).

Long-term observation of large-scale neutrophil response in mice after TBI through intact skull

To assess LEAO under the demanding conditions of TIS imaging, which introduces substantial aberrations with the presence of a thick, curved skull combined with chemical gels, we recorded neutrophil activity in mice with and without TBI for around 10 h (Supplementary Video 4). A closed head injury was established using an air gun[40] (Fig. 5a and Methods). This approach preserved the skull, its bone marrow, skull blood vessel and possibly the recently reported bone marrow–brain vascular channel[41], which are typically lost or damaged in open-skull preparations. Imaging of the neutrophil activity inside the above intact structures was conducted 4 h after the injury. Experimentally, severe aberrations were present in large FOV TIS imaging at the mesoscale, which can be accurately estimated by LEAO (Fig. 5b). LEAO successfully removed the distortion due to aberrations, restored the high-density neutrophil distribution from noisy raw data and enabled high-fidelity visualization of the neutrophil response with a marked improvement in the number of recognized neutrophil cells compared to results without AO (Fig. 5c,d and Supplementary Fig. 16). Neutrophil adhesion to the blood vessel wall and subsequent extravasation in response to inflammation were observed owing to the large, mesoscale FOV (Fig. 5e). Notably, intense gathering of neutrophils occurred in regions where the coronal suture (CS) and superior sagittal sinus (SSS) should be located (Fig. 5f). This may be due to several reasons. First, the SSS and CS overlap, with densely vascularized regions where neutrophils can be rapidly recruited due to inflammation. Second, the SSS and CS are sensitive to mechanical stress, and TBI may cause local neutrophil leakage. Third, the SSS and CS highly coincide with lymphatic vessel distribution, and this phenomenon is in accordance with the recent discovery regarding meningeal lymphatic drainage in the central nervous system, in which immune cells migrate through a meningeal pathway[42–45]. Such large-scale dynamics with preserved bone marrow have rarely been captured in vivo. Previous studies were limited either by aberration-constrained FOV or by tissue damage brought by open-skull surgery. LEAO overcame these challenges by enabling continuous, cell-level visualization without such limitations. In control mice, on the other hand, neutrophil migration toward the SSS and CS or activation within bone marrow were minimal (Fig. 5g–j). Temporal analysis confirmed the attenuated immune response in control mice compared to TBI mice (Fig. 5k). Quantitatively, TBI mice exhibited a steeper and more pronounced increase in cell density within SSS and CS regions compared to controls. Owing to the well-preserved skull structure, analysis focusing on the skull bone marrow could be carried out. An obvious density peak was observed in the frontal skull where bone marrow vessels are abundant, likely reflecting neutrophil activation in response to injury. On the other hand, frontal skull cell density in control mice showed a slight but continuous decline over time, presumably due to photobleaching, cell metabolism or migration to other areas. A similar density peak emerged in extravasation areas of TBI mice, where neutrophils initially accumulated and were subsequently cleared. Although control mice also showed slight extravasation, possibly from incidental bleeding, the cell density in extravasation areas gradually decreased. Additionally, the higher cell velocity in the frontal skull and extravasation areas of TBI mice compared to controls further supported these observations (Fig. 5l).

Discussion

In this work, we report LEAO, a wave-propagation digital AO framework utilizing latent-space-enhanced learning that introduces multiple theoretical innovations. Benefiting from the wave-optics-based modeling, LEAO outperforms conventional ray-optics-based AO methods. Central to LEAO is an autoencoder that extracts latent features from spatial–angular measurements, paired with an estimator that utilizes these features to infer aberration wavefronts with accuracy and stability (Supplementary Fig. 3). Furthermore, disentanglement of the latent representations of aberration and structural information improves interpretability and enables more precise corrections. As a result, LEAO demonstrates resilience to key experiment variables such as the magnitude of aberrations, the number of angular views, noise and the spatial sampling rate. Quantitatively, an accuracy sixfold higher than other approaches is achieved. We validated its performance across diverse biological contexts, including T cells in lymph nodes, neurons in mouse cortex and neutrophils imaged through the mouse intact skull over large depth. These simulations and experiments consistently demonstrate LEAO's practicability in producing reliable reconstructions from versatile in vivo LFM measurements. Researchers may be concerned about the generalization capability, which we addressed through transfer learning. We showed that LEAO can be quickly transferred to new structures and system setups while requiring only 2.5% of the training data and with 2–3 orders-of-magnitude reduction in training time (Supplementary Figs. 17 and 18). Ablation studies confirmed that the translatability was rooted in the scheme of latent-space disentangling, distilling aberration priors from sample-dependent information (Supplementary Fig. 19). It should also be noted that direct

Fig. 5 | LEAO combats large TIS-induced aberrations to continuously observe sophisticated neutrophil responses for more than 10 h in mice challenged with TBI. a, Schematic of the observation of TBI by a TIS window. **b**, Aberration wavefronts estimated by LEAO. **c**, Recognized cell number with LEAO and no AO at different time points. **d**, MIPs of neutrophil and blood vessel by LEAO. Enlarged images show the raw measurement, no AO and LEAO. **e**, Tracking of a neutrophil extravasation. **f**, Tracking of a neutrophil migration toward the CS. **g**,**h**, Time-coded projections of the recordings from a TBI mouse (**g**) and a control mouse (**h**). **i**,**j**, MIPs of a TBI mouse (**i**) and control mouse(**j**) at the initial (0 min) and final (632 min) time points. **k**, Curves of cell density in selected areas marked by boxes with the corresponding color in **g** and **h**. **l**, Curves of cell velocity in selected areas. Line, mean value. Shade, s.d. Number of cells used are provided in Source Data. Scale bars: 200 μm (**d**,**g**,**h**), 400 μm (**i**,**j**), 30 μm (**e**,**f**, zoom-in regions of **d**,**e**).

https://doi.org/10.1038/s41587-026-03107-2

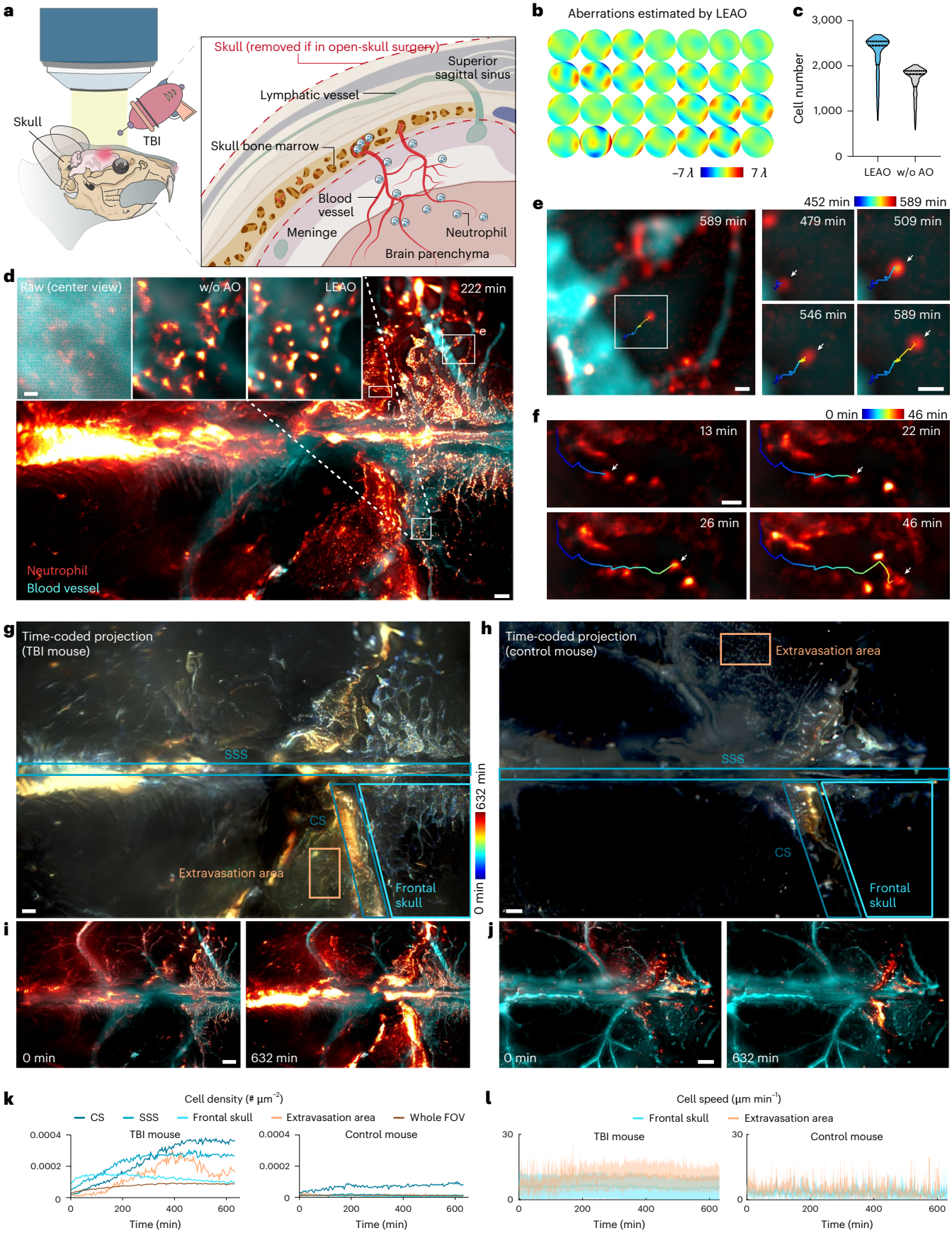

generalization without fine-tuning has already achieved higher accuracy than DAO. However, to ensure performance, every experiment conducted in this paper was either trained from scratch or transferred from a pretrained model (Supplementary Table 1).

LEAO represents a distinct technological advancement that uses spatial–angular imaging, wave-optics latent modeling and deep learning, setting it apart from existing approaches. Among recent deep-learning-based AO methods, CoCoA is advanced in its performance and generalization ability due to the self-supervised scheme[12]. However, CoCoA requires recalculating the PSF at each training iteration using the newly estimated aberration. This constraint renders it impractical for spatial–angular imaging, as computing high-dimensional PSFs typically exceeds 10 min per iteration. This limits the use of CoCoA to wide-field-based imaging, which can only deal with small aberrations, because wide-field microscopy is intrinsically more sensitive to aberrations than LFM (Supplementary Fig. 20). The same constraint applies for most popular blind deconvolution methods[46,47], as they are also based on two-dimensional (2D) wide-field imaging (Supplementary Fig. 21). Another method based on spatial–angular imaging with LFM, called wave-optics DAO (wDAO), which we previously developed, also claims to operate under a wave-optics prior[37]. wDAO estimates the aberration wavefront from phase gradients iteratively derived through a shift-to-wavefront-gradients function. However, the method relies solely on shift information between angular measurements. In contrast, LEAO utilizes high-dimensional latent features extracted directly from LFM spatial–angular measurements to infer aberrations. In addition, wDAO is limited to a one-time system calibration due to its computationally intensive iterative algorithm, making it unsuitable for dynamic or sample-specific aberration correction. As a result, its performance notably degrades when faced with variable sample-induced aberrations (Supplementary Fig. 22). Only LEAO can effectively and efficiently correct large aberrations by manipulating latent space representations and incorporating physical priors, thereby enabling robust performance in complex, real intravital environments. Furthermore, LEAO is highly compatible with existing strategies for spatial–angular imaging and can be readily combined with them. For example, pairing LEAO with specialized LFM modalities such as confocal LFM would enable simultaneous aberration correction, background rejection and optical sectioning[36,48–50]. Head-mounted LFM techniques already permit volumetric imaging at substantial depth in freely moving rodents but suffer from severe aberrations due to their miniaturized optics[51]. Integration with LEAO is expected to produce a marked improvement in imaging quality. Image enhancement techniques such as deblurring can be applied on LEAO-corrected images to further increase visual quality (Supplementary Fig. 5b).

Nevertheless, LEAO has several limitations. First, its generalization ability is not perfect. When applied to unseen sample types or systems, LEAO requires a brief fine-tuning phase to retain accuracy, which is not performed in real time (Supplementary Figs. 17 and 18). The required amount of data and time may increase with the level of discrepancy between the pretrained model and the target model, but we estimated the time cost to be about 5 min. A larger model trained across various sample types may eventually enable direct application to new data without additional training. Second, although we have accommodated LEAO to various experimental factors including noise, aberration magnitude variation, angle number, sampling rate and so on, a mismatch of simulated and experimental conditions will still exist. Degradations caused by factors outside of LEAO's design cannot be corrected. For example, it cannot fully recover resolution or imaging depth loss due to scattering, because the scattering model[52] is not considered in our current physical model of aberration formation (Methods). This issue may be addressed by adopting multiphoton excitation[53] or imaging strategies that incorporate scattering models[52]. Also, LEAO does not correct degradations that cannot be modeled as phase changes in the pupil plane. For example, motion blur caused by sample movement or image degradation resulting from evaporation in water-immersion objectives falls outside the correction capability of LEAO. As of now, we do not include a mechanism for the correction of sample motion. Third, LEAO relies on an iterative algorithm for reconstruction. Deep-learning methods that replace the time-consuming algorithmic pipeline of LFM reconstruction can run concurrently with LEAO, yielding reconstructions that are both rapid and high-fidelity[54–56]. Fourth, although we have conducted both simulated and experimental analyses on the disentanglement of the latent space, structure-dependent distortions such as scattering may still interfere with the disentangling process. Despite these challenges, LEAO's robust aberration correction based on physical priors and latent-space-enhanced deep learning is expected to facilitate widespread applications in intravital mesoscale imaging and multiscale subcellular investigations.

Online content

Any methods, additional references, Nature Portfolio reporting summaries, source data, extended data, supplementary information, acknowledgements, peer review information; details of author contributions and competing interests; and statements of data and code availability are available at https://doi.org/10.1038/s41587-026-03107-2.

References

1. Nasir-Moin, M. et al. Localization of protoporphyrin IX during glioma-resection surgery via paired stimulated Raman histology and fluorescence microscopy. *Nat. Biomed. Eng.* **8**, 672–688 (2024).
2. Kanatani, S. et al. Whole-brain spatial transcriptional analysis at cellular resolution. *Science* **386**, 907–915 (2024).
3. Sylwestrak, E. L., Rajasethupathy, P., Wright, M. A., Jaffe, A. & Deisseroth, K. Multiplexed intact-tissue transcriptional analysis at cellular resolution. *Cell* **164**, 792–804 (2016).
4. Ji, N. Adaptive optical fluorescence microscopy. *Nat. Methods* **14**, 374–380 (2017).
5. Peng, B. et al. Practical guidelines for cell segmentation models under optical aberrations in microscopy. *Comput. Struct. Biotechnol. J.* **26**, 23–39 (2024).
6. Chen, W. et al. In vivo volumetric imaging of calcium and glutamate activity at synapses with high spatiotemporal resolution. *Nat. Commun.* **12**, 6630 (2021).
7. Hampson, K. M. et al. Adaptive optics for high-resolution imaging. *Nat. Rev. Methods Prim.* **1**, 1–26 (2021).
8. Velasco, M. G. M. et al. 3D super-resolution deep-tissue imaging in living mice. *Optica* **8**, 442–450 (2021).
9. Wang, K. et al. Rapid adaptive optical recovery of optimal resolution over large volumes. *Nat. Methods* **11**, 625–628 (2014).
10. Schubert, M. C. et al. Deep intravital brain tumor imaging enabled by tailored three-photon microscopy and analysis. *Nat. Commun.* **15**, 7383 (2024).
11. Streich, L. et al. High-resolution structural and functional deep brain imaging using adaptive optics three-photon microscopy. *Nat. Methods* **18**, 1253–1258 (2021).
12. Kang, I., Zhang, Q., Yu, S. X. & Ji, N. Coordinate-based neural representations for computational adaptive optics in widefield microscopy. *Nat. Mach. Intell.* **6**, 714–725 (2024).
13. Hu, Q. et al. Universal adaptive optics for microscopy through embedded neural network control. *Light Sci. Appl.* **12**, 270 (2023).
14. Zhang, Y. et al. Conformal convolutional neural network (CCNN) for single-shot sensorless wavefront sensing. *Opt. Express* **28**, 19218 (2020).
15. Guo, M. et al. Deep learning-based aberration compensation improves contrast and resolution in fluorescence microscopy. *Nat. Commun.* **16**, 313 (2025).
16. Wu, J. et al. Iterative tomography with digital adaptive optics permits hour-long intravital observation of 3D subcellular dynamics at millisecond scale. *Cell* **184**, 3318–3332 (2021).

17. Jogin, M. et al. Feature extraction using convolution neural networks (CNN) and deep learning. In *Proc. 3rd International Conference on Recent Trends in Electronics, Information & Communication Technology* https://doi.org/10.1109/RTEICT42901.2018.9012507 (IEEE, 2018).
18. Liang, H., Sun, X., Sun, Y. & Gao, Y. Text feature extraction based on deep learning: a review. *EURASIP J. Wirel. Commun. Netw.* **2017**, 211 (2017).
19. Shaheen, F., Verma, B. & Asafuddoula, M. D. Impact of automatic feature extraction in deep learning architecture. In *Proc. International Conference on Digital Image Computing: Techniques and Applications* https://doi.org/10.1109/DICTA.2016.7797053 (IEEE, 2016).
20. Chen, B. et al. Automated discovery of fundamental variables hidden in experimental data. *Nat. Comput. Sci.* **2**, 433–442 (2022).
21. Higgins, I. et al. Unsupervised deep learning identifies semantic disentanglement in single inferotemporal face patch neurons. *Nat. Commun.* **12**, 6456 (2021).
22. Zhang, C. et al. A large, switchable optical clearing skull window for cerebrovascular imaging. *Theranostics* **8**, 2696–2708 (2018).
23. Silasi, G., Xiao, D., Vanni, M. P., Chen, A. C. N. & Murphy, T. H. Intact skull chronic windows for mesoscopic wide-field imaging in awake mice. *J. Neurosci. Methods* **267**, 141–149 (2016).
24. de Haan, K., Rivenson, Y., Wu, Y. & Ozcan, A. Deep-learning-based image reconstruction and enhancement in optical microscopy. *Proc. IEEE* **108**, 30–50 (2020).
25. Reichstein, M. et al. Deep learning and process understanding for data-driven Earth system science. *Nature* **566**, 195–204 (2019).
26. Mathieu, E., Rainforth, T., Siddharth, N. & Teh, Y. W. Disentangling disentanglement in variational autoencoders. In *Proc. 36th International Conference on Machine Learning* (eds Chaudhuri, K. & Sugiyama, M.) 4402–4412 (PMLR, 2019).
27. Brahma, P. P., Wu, D. & She, Y. Why deep learning works: a manifold disentanglement perspective. *IEEE Trans. Neural Netw. Learn. Syst.* **27**, 1997–2008 (2016).
28. Zheng, Z. & Sun, L. Disentangling latent space for VAE by label relevant/irrelevant dimensions. In *Proc. IEEE/CVF Conference on Computer Vision and Pattern Recognition* 12192–12201 (2019).
29. Lu, Z. et al. Phase-space deconvolution for light field microscopy. *Opt. Express* **27**, 18131–18145 (2019).
30. Liu, D. et al. T–B-cell entanglement and ICOSL-driven feed-forward regulation of germinal centre reaction. *Nature* **517**, 214–218 (2015).
31. Mao, T. et al. Long-range neuronal circuits underlying the interaction between sensory and motor cortex. *Neuron* **72**, 111–123 (2011).
32. Meiniel, W., Olivo-Marin, J.-C. & Angelini, E. D. Denoising of microscopy images: a review of the state-of-the-art, and a new sparsity-based method. *IEEE Trans. Image Process.* **27**, 3842–3856 (2018).
33. Mandracchia, B. et al. Fast and accurate sCMOS noise correction for fluorescence microscopy. *Nat. Commun.* **11**, 94 (2020).
34. Liang, C.-K., Lin, T.-H., Wong, B.-Y., Liu, C. & Chen, H. H. Programmable aperture photography: multiplexed light field acquisition. In *ACM SIGGRAPH 2008 papers* https://doi.org/10.1145/1399504.1360654 (ACM, 2008).
35. Prevedel, R. et al. Simultaneous whole-animal 3D imaging of neuronal activity using light-field microscopy. *Nat. Methods* **11**, 727–730 (2014).
36. Lu, Z. et al. Long-term intravital subcellular imaging with confocal scanning light-field microscopy. *Nat. Biotechnol.* **43**, 569–580 (2025).
37. Zhang, Y. et al. Long-term mesoscale imaging of 3D intercellular dynamics across a mammalian organ. *Cell* **187**, 6104–6122 (2024).
38. Zhao, Z. et al. Two-photon synthetic aperture microscopy for minimally invasive fast 3D imaging of native subcellular behaviors in deep tissue. *Cell* **186**, 2475–2491 (2023).
39. Qi, H., Cannons, J. L., Klauschen, F., Schwartzberg, P. L. & Germain, R. N. SAP-controlled T–B cell interactions underlie germinal centre formation. *Nature* **455**, 764–769 (2008).
40. Chen, C. et al. A novel simple traumatic brain injury mouse model. *Chin. Neurosurg. J.* **08**, 151–159 (2022).
41. Herisson, F. et al. Direct vascular channels connect skull bone marrow and the brain surface enabling myeloid cell migration. *Nat. Neurosci.* **21**, 1209–1217 (2018).
42. Hauglund, N. L., Kusk, P., Kornum, B. R. & Nedergaard, M. Meningeal lymphangiogenesis and enhanced glymphatic activity in mice with chronically implanted EEG electrodes. *J. Neurosci.* **40**, 2371–2380 (2020).
43. Hershenhouse, K. S., Shauly, O., Gould, D. J. & Patel, K. M. Meningeal lymphatics: a review and future directions from a clinical perspective. *Neurosci. Insights* **14**, 1–9 (2019).
44. Louveau, A. et al. CNS lymphatic drainage and neuroinflammation are regulated by meningeal lymphatic vasculature. *Nat. Neurosci.* **21**, 1380–1391 (2018).
45. Mentis, A.-F. A., Dardiotis, E. & Chrousos, G. P. Apolipoprotein E4 and meningeal lymphatics in Alzheimer disease: a conceptual framework. *Mol. Psychiatry* **26**, 1075–1097 (2021).
46. Jin, M., Roth, S. & Favaro, P. Normalized blind deconvolution. In *Proc. Computer Vision – ECCV 2018* (eds Ferrari, V. et al.) 694–711 (Springer, 2018).
47. Eboli, T., Morel, J.-M. & Facciolo, G. Fast two-step blind optical aberration correction. In *Proc. Computer Vision – ECCV 2022* (eds Avidan, S. et al.) 693–708 (Springer, 2022).
48. Zhang, Z. et al. Imaging volumetric dynamics at high speed in mouse and zebrafish brain with confocal light field microscopy. *Nat. Biotechnol.* **39**, 74–83 (2021).
49. Vogt, N. Volumetric imaging with confocal light field microscopy. *Nat. Methods* **17**, 956–956 (2020).
50. Bai, L. et al. Volumetric voltage imaging of neuronal populations in the mouse brain by confocal light-field microscopy. *Nat. Methods* **21**, 2160–2170 (2024).
51. Skocek, O. et al. High-speed volumetric imaging of neuronal activity in freely moving rodents. *Nat. Methods* **15**, 429–432 (2018).
52. Zhang, Y. et al. Computational optical sectioning with an incoherent multiscale scattering model for light-field microscopy. *Nat. Commun.* **12**, 6391 (2021).
53. Xu, C., Nedergaard, M., Fowell, D. J., Friedl, P. & Ji, N. Multiphoton fluorescence microscopy for in vivo imaging. *Cell* **187**, 4458–4487 (2024).
54. Wagner, N. et al. Deep learning-enhanced light-field imaging with continuous validation. *Nat. Methods* **18**, 557–563 (2021).
55. Wang, Z. et al. Real-time volumetric reconstruction of biological dynamics with light-field microscopy and deep learning. *Nat. Methods* **18**, 551–556 (2021).
56. Lu, Z. et al. Physics-driven self-supervised learning for fast high-resolution robust 3D reconstruction of light-field microscopy. *Nat. Methods* **22**, 1545–1555 (2025).

Methods

Experimental setup

Experiments in Figs. 3–5 were conducted using the previously developed RUSH3D system[37], a compact, single-cell-resolution 3D mesoscope with a 0.5 numerical aperture (NA) objective, an angular resolution of 15 × 15 and scanning of 3 × 3. For the lymph node imaging in Fig. 3, we used a multicolor light-emitting diode (LDI-7-488, 89 North); a microlens array of 69-µm pitch, 393.3-µm focal length; and a 12-bit camera with 7,920 pixels × 6,004 pixels, 4.6-µm pixel size (CMV50000, CMOSIS). The effective system magnification is 5.761. For the mouse brain neuronal imaging in Fig. 4, we used a laser diode illuminator (LDI-PRIME 15070, 89 North); a customized objective lens with NA of 0.5; a microlens array of 56.4-µm pitch, 499-µm focal length; and a complementary metal-oxide-semiconduct (CMOS) camera (QHYCCD QHY411). The effective system magnification is 9.25. For TIS imaging in Fig. 5, we used the same laser and camera as in Fig. 4, along with another customized objective lens with NA of 0.5. The microlens array is of 56.4-µm pitch and 444-µm focal length. The effective system magnification rate is 7.85. Details regarding imaging samples, labels, excitation wavelength and additional experimental parameters are provided in Supplementary Table 2.

In Fig. 2m,n, we simulated five different systems to demonstrate LEAO's compatibility with various spatial–angular imaging setups. We list the parameters used in respective systems here. The LFM has a 1.05-NA objective with refractive index of 1.33; a microlens array of 136.5-µm pitch, 2,800-µm focal length; 21 × 21 angular resolution; and a system magnification rate of 43.067. The sLFM configuration is the same as that of LFM except for adding a 3 × 3 scanning scheme. The confocal scanning LFM configuration is the same as that of sLFM except for adding a line-confocal illumination with a slit size of 11-times Airy units of the whole-objective NA to reject background fluorescence. The RUSH3D has a 0.5-NA objective with refractive index of 1; a microlens array of 69-µm pitch, 393.3-µm focal length; an angular resolution of 15 × 15 with scanning of 3 × 3; and a system magnification rate of 5.761. The two-photon synthetic aperture microscopy has a 1.05-NA objective with refractive index of 1.33, a pinhole size of 50 µm (α = 0.1), an angular resolution of 13 and a system magnification rate of 18.

In Supplementary Figs. 13 and 14, we used an LFM system with removable phase masks to introduce designed aberration wavefronts. The system has a 0.5-NA objective with refractive index of 1; a microlens array of 100-µm pitch, 2,100 µm focal length; and 15 × 15 angular resolution. The magnification rate is 20. A phase mask made of Corning 7980 glass installed on a translation mount (TXYZ05, LBTEK) can be inserted or removed at the pupil plane of the emission light. By spatially modulating the optical path, the phase mask modifies the wavefront according to a custom design.

Network architectures of LEAO

In this work, we proposed a three-part network architecture for feature extraction and aberration estimation. The input to our network is the spatial–angular measurements from LFM, and the output is the decoded spatial–angular images and the estimated aberration wavefronts. The decoded spatial–angular images are used to compute the reconstruction loss to enable the feature extraction process of the encoder–decoder branch, which enhances the estimation accuracy and generalization ability of the network, compared to using only a vanilla regressor (Supplementary Figs. 3 and 17). The encoder $\mathcal{E}$ performs dimension reduction on the input data (size angle × height × width pixels) to form latent features (size of $C \times \text{height}/2^{\text{ds}} \times \text{width}/2^{\text{ds}}$ pixels, where C denotes the channel number of 2D convolution layers and is usually set to 64, and ds denotes the downsampling block number in the network, usually set to 3). Then, all features are fed to the decoder $\mathcal{D}$ and features encoding aberration (usually half of the features) are fed to the estimator $\mathcal{P}$. The decoder $\mathcal{D}$ retrieves the spatial–angular images (size of angle × height × width pixels) from the dimensionally reduced latent features, and the estimator $\mathcal{P}$ outputs the Zernike coefficients (size 17 pixels unless otherwise specified), which are then turned into an aberration wavefront by linearly combining the selected Zernike polynomials according to the estimated coefficients. Reconstruction loss is formed as the mean squared error of the input spatial–angular data and the output spatial–angular data. Aberration loss is the mean squared error of the actual aberration wavefront introduced into the imaging process and the estimated aberration wavefront.

In the first stage of training, joint optimization of the encoder, decoder and estimator is achieved through alternative training of the encoder–decoder and encoder–estimator branches. A validation dataset is introduced to monitor the convergence of the network. When the validation loss between the GT aberration wavefronts and the estimated aberration wavefronts no longer decreases for ten epochs, we conclude that the feature extraction is completed and the training enters the second stage, where the latent loss starts to be computed. Latent loss $\mathcal{L}_{\text{L}}$ consists of aberration-encoding loss $\mathcal{L}_{\text{A}}$ and structure-encoding loss $\mathcal{L}_{\text{S}}$:

$$\mathcal{L}_{\text{L}} = \mathcal{L}_{\text{A}} + \mathcal{L}_{\text{S}} \tag{1}$$

To encourage feature disentangling, we specifically incorporated a data triplet strategy using a simulated dataset[57]. Three spatial–angular measurements $S_{1,1}$, $S_{2,1}$ and $S_{1,2}$ are jointly required to compute the latent loss (Supplementary Fig. 3g). Among them, two stacks $S_{1,1}$ and $S_{1,2}$ share the same structure V_1, and the other stack $S_{2,1}$ is formed by another structure V_2. Two stacks $S_{1,1}$ and $S_{2,1}$ share the same aberration wavefront φ_1, and $S_{1,2}$ is degraded by another aberration φ_2. Their latent features $\mathcal{E}(S_{1,1})$, $\mathcal{E}(S_{2,1})$ and $\mathcal{E}(S_{1,2})$ are each split along the channel dimension into two components: the aberration-encoding component $\mathcal{E}_{\text{A}}(S_{1,1})$, $\mathcal{E}_{\text{A}}(S_{2,1})$ and $\mathcal{E}_{\text{A}}(S_{1,2})$ and the structure-encoding component $\mathcal{E}_{\text{S}}(S_{1,1})$, $\mathcal{E}_{\text{S}}(S_{2,1})$ and $\mathcal{E}_{\text{S}}(S_{1,2})$. The aberration-encoding loss $\mathcal{L}_{\text{A}}$ is computed using the former component, and structure-encoding loss $\mathcal{L}_{S}$ is computed using the latter:

$$\mathcal{L}_{\text{A}} = \max\left(0, \text{MSE}\left(\mathcal{E}_{\text{A}}(S_{1,1}), \mathcal{E}_{\text{A}}(S_{2,1})\right) - \text{MSE}\left(\mathcal{E}_{\text{A}}(S_{1,1}), \mathcal{E}_{\text{A}}(S_{1,2})\right) + \text{margin}\right) \tag{2}$$

$$\mathcal{L}_{\text{S}} = \max\left(0, \text{MSE}\left(\mathcal{E}_{\text{S}}(S_{1,1}), \mathcal{E}_{\text{S}}(S_{1,2})\right) - \text{MSE}\left(\mathcal{E}_{\text{S}}(S_{1,1}), \mathcal{E}_{\text{S}}(S_{2,1})\right) + \text{margin}\right) \tag{3}$$

where $\max(\cdot,\cdot)$ is an operator that returns the larger one of two input values, $\text{MSE}(\cdot,\cdot)$ computes the mean squared error between its inputs and margin is a hyperparameter to control the extent to which dissimilar features are separated, typically set to 1 in our experiments[58,59]. The incorporation of the latent loss leads to a continued decrease in validation loss, as effective disentanglement of latent features helps suppress irrelevant information and improves aberration estimation accuracy (Supplementary Fig. 3h). The convergence of the validation loss serves as a criterion for terminating the training process. The well-trained model exhibits high aberration estimation accuracy with a well-disentangled latent space (Supplementary Fig. 3i–k).

The detailed network structure is illustrated in Supplementary Fig. 4. The encoder consists of two initial convolutional layers, followed by a series of residual groups, the number of which is typically set to three (except for Supplementary Fig. 23, which uses six). Each residual group contains multiple (usually two, except for Supplementary Fig. 23, which uses eight) residual channel attention blocks (RCABs) and a max pooling operation for downsampling (with a scale factor of 2), except for Supplementary Fig. 23, which applies the max pooling only for the first three residual groups. Each RCAB consists of two convolutional layers, each followed by a leaky ReLU activation and a CA layer. The CA layer performs global average pooling to extract channel-wise statistics, which are then passed through two 1 × 1 convolution layers to produce attention weights. These weights are used to adaptively

recalibrate the feature maps, enhancing the representational capability of the network. The decoder retrieves the input from the latent representation learned by the encoder. It mirrors the encoder's structure, consisting of residual groups containing multiple RCABs and bilinear upsampling operations in place of max pooling. Following upsampling, two additional convolutional layers are applied to generate the final output, which maintains the same spatial dimensions as the input. The estimator branch processes the latent features using three convolutional layers, each followed by a leaky ReLU activation, to extract aberration-relevant information. The resulting feature maps are then subjected to a global average pooling to yield a compact feature vector, which is subsequently passed through a fully connected layer to produce a vector corresponding to the estimated Zernike coefficients. The channel number for each convolutional layer is specified in Supplementary Fig. 4.

After inference with LEAO, the estimated aberration wavefront is used to compute the corresponding PSF based on the wave-optics model (Supplementary Fig. 24). Then the PSF is employed in an iterative tomography algorithm to reconstruct a high-resolution 3D volume from the aberrated spatial–angular measurements (Supplementary Fig. 5a)[16]. For spatial–angular measurements with spatially non-uniform aberrations, multiple PSFs are generated corresponding to different spatial tiles. Each tile is reconstructed individually, and the resulting volumes are subsequently fused into a single volume using a sigmoid-function-based image fusion method[60].

Simulation of aberrated spatial–angular measurements

All training spatial–angular measurements were generated by applying aberrated PSFs on 3D volumes following a wave-optics forward imaging model (Supplementary Fig. 24). A set of Zernike coefficients $\{c_k\}_k$ $(k = 1, \ldots, K)$ were generated randomly following $c_k \sim U([a_k, b_k])$ $(1 \le k \le K)$, where $U([a_k, b_k])$ is a uniform distribution on $[a_k, b_k]$. Then the aberration at the pupil plane was generated by

$$\phi(r,\theta) = \sum_{k=1}^{K} c_k Z_k(r,\theta) \tag{4}$$

where $Z_k(r,\theta)$ is the kth Zernike polynomial under American National Standards Institute indexing[61]. To be more specific, the polynomials are defined as

$$Z_j(r,\theta) = Z_n^m(r,\theta) = \begin{cases} R_n^m(r)\cos(m\theta), & m \ge 0, \\ R_n^{|m|}(r)\sin(|m|\theta), & m < 0, \end{cases} \tag{5}$$

where j is a positive index following

$$j = \frac{n(n+2)+m}{2} + 1 \tag{6}$$

and R_n^m is defined as

$$R_n^m(r) = \sum_{s=0}^{(n-m)/2} \frac{(-1)^s (n-s)!}{s!\left(\frac{n+m}{2}-s\right)!\left(\frac{n-m}{2}-s\right)!} r^{n-2s} \tag{7}$$

We listed the Zernike polynomials in order in Supplementary Fig. 25. We set $K = 21$ for all our experiments unless otherwise noted, but LEAO also possesses the ability to solve higher-order aberrations (Supplementary Fig. 23). Coefficients for piston, tilt and defocus modes were set to 0, as they were too low-order and had already been corrected during the system setup. To generate an aberration with a desired root-mean-squared (RMS) value σ_t, we computed the current RMS σ_c of the aberration wavefront and then applied a rescaling

$$\phi_{\text{rescaled}}(r,\theta) = \frac{\sigma_t}{\sigma_c}\phi(r,\theta) \tag{8}$$

Next, an aberrated PSF was generated based on the rescaled aberration and the previously developed spatial–angular imaging model[16,29]. When without aberration, light from a point source (x_1, x_2, x_3) forms the field below at the image plane:

$$U_{\text{ideal}}(y, x_3) = \frac{M_{\text{sys}}}{f_{\text{obj}}^2 \lambda^2} \exp\left(-\mathrm{i}\cdot\frac{2\pi}{\lambda}x_3\right) \int_0^{\theta} \sqrt{\cos\varphi}\exp\left(-\mathrm{i}\frac{4\pi x_3 \sin^2(\varphi/2)}{\lambda}\right) J_0\left(\frac{2\pi \sin(\varphi)}{\lambda}\sqrt{(y_1-x_1)^2+(y_2-x_2)^2}\right)\sin(\varphi)\,\mathrm{d}\varphi, \tag{9}$$

where $y = (y_1, y_2)$ is the position on the image plane, f_{obj} is the focal length of the objective lens, λ is the emission wavelength, M_{sys} is the magnification rate of the optical system, $J_0(\cdot)$ is the 0th-order Bessel function of the first kind, θ is the half-angle of the maximum light cone accepted by the objective and φ is the angle between the light ray and the optical axis. To take the effect of aberration into consideration, we need to apply it to the phase of the Fourier transformation of U_{ideal}, for this is equivalent to applying a continuous wavefront distortion at the pupil plane:

$$U_{\text{aberrated}} = \mathcal{F}^{-1}\left(\mathcal{F}(U_{\text{ideal}})\,\mathrm{e}^{\mathrm{i}\phi_{\text{rescaled}}}\right) \tag{10}$$

where $\mathcal{F}^{-1}$ and $\mathcal{F}$ are the reverse Fourier transform and Fourier transform. After that, following the configuration of a typical light-field system, the light goes through a microlens array $t(y)$ and propagates to the detector plane:

$$U_{\text{detected}}(y', x_3) = \frac{\mathrm{e}^{\mathrm{i}\frac{2\pi n}{\lambda} f_{\mu\text{lens}}}}{\mathrm{i}\frac{2\pi n}{\lambda} f_{\mu\text{lens}}} \int_x U_{\text{aberrated}}(y, x_3) \cdot t(y) \cdot \exp\left\{j\frac{\pi n}{\lambda f_{\text{lens}}}\|y' - y\|_2^2\right\}\mathrm{d}y \tag{11}$$

where y' is the position on the detector plane, n is the refractive index and $f_{\mu\text{lens}}$ is the focal length of the microlens array. Each pixel y' has a relative lateral shift u_0 with respect to one of the microlens array with a center position y_0. Thus, the aberrated PSF can be formed as

$$\text{PSF}(y_0, x_3, u_0) = \int_{x'} \left\| U_{\text{detected}}(y', x_3)\,\text{rect}\left(\frac{y' - y_0 - u_0}{d_s}\right)\right\|_2^2 \mathrm{d}y', \tag{12}$$

where d_s is the sensor pixel size and rect() is the rectangle function.

Aberrated LFM spatial–angular measurements were further obtained by

$$\text{LF}_{m,n}(x,u) = \int_z V_n(x,z) * \text{PSF}_m(x,z,u)\,\mathrm{d}z, 1 \le m \le M, 1 \le n \le N \tag{13}$$

where PSF_m is the mth aberrated PSF, V_n is the nth 3D volume, and * is the 2D convolution with respect to x. $M = 200$ for all our experiments except Supplementary Fig. 23, in which a higher number of PSFs ($M = 600$) is needed to train a model capable of processing higher-order aberrations. N depends on the accessible number of data, typically in the range of 60–200. We typically selected 2,000 $\text{LF}_{m,n}$ for training LEAO, which is empirically chosen and validated to be sufficient (Supplementary Fig. 26). After generation of the training dataset, the wave-optics aberration information is encoded in the spatial–angular measurements, waiting to be extracted by LEAO. Performance was evaluated on ten additional data that were excluded from training. The training data number for each figure is listed in Supplementary Table 1.

When conducting noise experiments, we first linearly adjusted the brightness of the clean simulated data so that the peak photon count,

defined as the 99.9th percentile of all intensity values, was set to the desired value, forming the stack LF. Then we applied additive Gaussian noise of s.d. 4 and a Poisson noise simulating the photon shot noise, forming the stack LF_{noisy}. Different experiments were conducted for decreasing peak photon count. We calculated the SNR of each image by

$$\mathrm{SNR} = 20\log_{10}\left(\frac{||\mathrm{LF}||_2}{||\mathrm{LF} - \mathrm{LF}_{\mathrm{noisy}}||_2}\right) \quad (14)$$

and then defined the SNR of the respective peak photon count to be the average of all SNR values calculated on test data with this peak photon count.

Mouse brain slice imaging

In the mouse brain slice experiments for Supplementary Figs. 13 and 14, 6–8-week Thy1-YFP (JAX 003709) mice were used. After anesthesia and phosphate-buffered saline perfusion, separation of the mouse brain and the skull was completed. Overnight, the brain was fixed with 4% paraformaldehyde at a temperature of 4 °C. Subsequently, with a Leica vibratome (Leica VT1200 S), a coronal section of the mouse brain at 100 µm was made. The sections were mounted in mounting medium (Sigma, catalog no. F4680) for subsequent imaging.

Lymph node imaging

In the lymph node experiment, we followed a previously performed protocol[62]. Specifically, dsRed-expressing OT-II mice were generated by crossing dsRed-expressing mice (JAX 6051) and OT-II mice carrying $OVA_{323\text{-}339}$-specific T cell receptor transgenes (JAX 4194). Using the negative selection CD4 T cell isolation kit (Miltenyi Biotec), OT-II T cells were isolated from OT-II mice. C57BL/6 (JAX 0664) mice were used as recipients and injected with freshly isolated dsRed-expressing OT-II T cells (0.8×10^5 per mouse) and non-fluorescent OT-II T cells (3.2×10^5 per mouse). One hundred thirty µg HEL-OVA antigen, formulated using a 1:1 emulsion with alum adjuvant (Thermo Scientific) and supplemented with 0.5 µg lipopolysaccharide (LPS, Sigma), was used for immune activation in the recipient mice. The HEL-OVA conjugates were synthesized via chemical crosslinking using the HydraLink kit (SoluLink)[39].

All mice were sourced from The Jackson Laboratory and aged 6–12 weeks. Mice were imaged using the RUSH3D microscope after the inguinal lymph node surgery[39,63].

Mouse cortex calcium imaging

Neural activity was imaged in GCaMP6f-expressing mice obtained by interbreeding Rasgrf2-2A-dCre mice with Ai148 (TIT2L-GC6f-ICL-tTA2)-D mice. An 8.0-mm circular craniotomy was made on adult mice (8–16 weeks postnatal) anesthetized with 1.5% (v/v) isoflurane in oxygen. Following excision of the skull segment, a glass coverslip was positioned over the surface and sealed in place, and a titanium headpost was affixed to the skull using dental cement to permit stable head immobilization during imaging. Expression of GCaMP6f in cortical layer 2/3 neurons across the brain was pharmacologically induced via intraperitoneal administration of trimethoprim (0.25 mg per g body weight). After a 14-day post-surgery interval to allow for resolution of inflammatory responses and optical clearing of the cranial window, awake, head-fixed mice were used for RUSH3D calcium imaging.

Neuron extraction and calcium analysis

A region 796 µm × 820 µm in the mouse cortex was manually selected for calcium analysis in Fig. 4. Motion correction and neuron extraction were performed using the Constrained Nonnegative Matrix Factorization (CNMF) algorithm implemented by CaImAn[64]. Raw fluorescence trace F from each neuron was used to calculate $\Delta F/F$ such that

$$\Delta F/F = \frac{F - F_0}{F_0} \quad (15)$$

where F_0 is the median of the temporal trace. Deconvolution was performed[65] to infer the most likely discretized spikes.

TIS window preparation

For the TIS imaging in Fig. 5, 8-week-old wild-type C57BL/6 or BALB/c mice anesthetized via intraperitoneal injection of 250 mg per kg Avertin (tribromoethanol) were placed in a stereotaxic head-fixation apparatus for removal of the scalp and periosteum and clearance of the connective tissues over the skull surface. S1 and S2 solutions were sequentially applied and rinsed off, as described in previous protocols[22]. A transparent UV-curable gel was then applied to the skull surface and cured under UV light for 3 min to form a stable, optically clear polymer window. A custom-made head bar was affixed to the skull using dental cement. To preserve the clarity of the window before imaging, the surface was protected with adhesive tape until the imaging session.

TBI model preparation

A modified toy-gun-based device was used to generate a controlled, mild mechanical impact to the skull as the TBI model (Fig. 5)[40]. A single discharge produced subarachnoid hemorrhage and promoted neutrophil extravasation. The magnitude of the impact was regulated by varying the distance between the skull surface and the gun barrel. Following the impact, the UV-cured gel cranial window remained optically clear and mechanically stable, enabling subsequent intravital imaging.

Mouse neutrophil activity recording

For the neutrophil activity recording in Fig. 5, mice received tail vein injections of a mixture consisting of 10 µl phycoerythrin-conjugated anti-Ly6G antibody for neutrophil labeling (catalog no. 127608, BioLegend, clone 1A8) and 50 µl of 5 mg ml^{-1} Sulfo-Cy5.5-carboxylic acid (catalog no. D10153-5, DuoFluor) for vascular labeling. The mixture was diluted with 90 µl sterile saline buffer. For the TBI mouse model, the injection was administered 4 h post-injury, followed by imaging with the RUSH3D system.

Mice housing conditions

Mice used in this study were maintained under standard laboratory conditions, with unrestricted access to food and water. Animals were kept on a 12-h light–dark schedule in a temperature-controlled environment (~22 °C) with ~50% relative humidity.

Implementation details of LEAO

LEAO was implemented on a PyTorch platform. Network training was performed on paired LFM data stacks and aberration wavefronts. Input data stacks were randomly cropped to extract patches of the desired size. The Adam optimizer was used with parameters $\beta_1 = 0.9, \beta_2 = 0.999$ and $\mathrm{lr} = 10^{-4}$. Detailed training and inference configurations, including training input size, inference input size, convergence epoch, training time and inference time are provided in Supplementary Table 1. All tasks were conducted using an NVIDIA RTX 3090 Ti GPU and an Intel Xeon Gold 6148 processor.

Performance evaluation

Normalized residual aberration σ has been used to quantitatively assess the accuracy of the aberration estimation. To calculate σ, first we need to calculate the RMS error of the residual aberration. RMS is the s.d. of $\Delta\phi = \hat{\phi} - \phi$, the difference between the estimated aberration $\hat{\phi}$ and the GT aberration ϕ:

$$\mathrm{RMS} = \sqrt{\frac{1}{P-1}\sum_{i=1}^{P}\left(\Delta\phi(i) - \frac{1}{P}\sum_{j=1}^{P}\Delta\phi(j)\right)^2} \quad (16)$$

where P is the total number of pixels within the incircle of $\Delta\phi$, and $\Delta\phi(i)$ is the value of the ith pixel in $\Delta\phi$. We maintained the size 199 × 199 for

all aberrations in this paper. This value was empirically set to avoid wasting computation resources (too large) or resulting in inaccurate metrics (too small). Next, normalization is performed so that

$$\sigma = \frac{RMS}{\max(\phi) - \min(\phi)} \quad (17)$$

where $\max(\phi)$ is the maximum value of ϕ and $\min(\phi)$ the minimum.

The direct output of the LEAO network is the aberration wavefront, but a shift-to-phase computation should be conducted to obtain the estimated aberration wavefront of DAO. We generated the wavefronts from DAO's shift maps through planar integration[66]. We simulated the estimated aberration wavefronts of hardware AO to be the discretization of the GT aberration wavefronts. Specifically, we divided the GT aberration wavefront into square patches, the number of which was determined by the actuator number of the deformable mirror, and fit each patch, respectively, using a linear phase profile $\phi(x,y) = ax + by + c$ simulating the piston, tip and tilt of the actuator. The wide-field imaging results of hardware AO were obtained by convolution of the GT sample with the wide-field PSF with residual aberration. The deconvolved hardware AO results were obtained by performing Richardson–Lucy deconvolution on the wide-field imaging results.

PSNR and SSIM were used to evaluate the fidelity of the aberration-corrected volumes. Before calculation, registration was first conducted to align the reconstructions to the GT volume, because shifts were highly possible in the DAO reconstruction. Specifically, the translation transformation matrix was optimized using the imregtform() function in MATLAB using *xy*- and *xz*-maximum intensity projections (MIPs) of the volume. Reconstructions were translated using the imwarp() function and the transformation matrix. Then, all volumes were normalized and fed to the MATLAB functions psnr() and ssim().

All above-mentioned preprocessing before evaluation was conducted on all methods for fair comparison.

Ethics statement

Animal protocol procedures were reviewed and approved by the Institutional Animal Care and Use Committee office of Tsinghua University.

Data analysis

All performance analyses were performed with customized MATLAB (MathWorks, MATLAB R2024a) scripts and Python (v.3.9.7) scripts. All 3D renderings and the tracking in Figs. 3–5 were performed using Imaris (v.9.0).

Statistics and reproducibility

Data shown in Figs. 3 and 4 and Supplementary Videos 2 and 3 are representative of $n = 10$ experiments. Data shown in Fig. 5, Supplementary Figs. 13 and 14 and Supplementary Video 4 are representative of $n = 6$ experiments. Data from other simulation-based figures are representative of $n = 12$ experiments.

Reporting summary

Further information on research design is available in the Nature Portfolio Reporting Summary linked to this article.

Data availability

Downloading links to example data used for demonstrations are available via the GitHub repository at https://github.com/TristaZeng/LEAO (ref. 67). All simulated neuronal data were generated using the Neural Anatomy and Optical Microscopy package and its modifications[68,69]. Other simulated data used the open-source dataset by the Allen Institute (https://www.allencell.org/data-downloading.html#DownloadImageData). Source data are provided with this paper.

Code availability

The Python code for LEAO, several representative pretrained models, as well as the example dataset for training and testing are publicly accessible via the GitHub repository at https://github.com/TristaZeng/LEAO (ref. 67).

References

57. Schroff, F., Kalenichenko, D. & Philbin, J. FaceNet: a unified embedding for face recognition and clustering. In *Proc. IEEE Conference on Computer Vision and Pattern Recognition (CVPR)* https://doi.org/10.1109/CVPR.2015.7298682 (2015).
58. Do, T.-T. et al. A theoretically sound upper bound on the triplet loss for improving the efficiency of deep distance metric learning. In *Proc. IEEE/CVF Conference on Computer Vision and Pattern Recognition (CVPR)* https://doi.org/10.1109/CVPR.2019.01065 (IEEE, 2019).
59. Schultz, M. & Joachims, T. Learning a distance metric from relative comparisons. In *Proc. Advances in Neural Information Processing Systems* (eds Thrun, S. et al.) 41–48 (MIT Press, 2003).
60. Luo, X., Zhang, Z. & Wu, X. Image fusion using region segmentation and sigmoid function. In *Proc. 22nd International Conference on Pattern Recognition* https://doi.org/10.1109/ICPR.2014.190 (IEEE, 2014).
61. Niu, K. & Tian, C. Zernike polynomials and their applications. *J. Opt.* **24**, 123001 (2022).
62. Zhang, Y. et al. Long-term mesoscale imaging of 3D intercellular dynamics across a mammalian organ. *Cell* https://doi.org/10.1016/j.cell.2024.08.026 (2024).
63. Liu, B. & Qi, H. In vivo migration and Tfh cell Interactions. in *T-Follicular Helper Cells* (ed Graca, L.) Ch. 9 (Springer, 2022); https://doi.org/10.1007/978-1-0716-1736-6_9
64. Giovannucci, A. et al. CaImAn an open source tool for scalable calcium imaging data analysis. *Elife* **8**, e38173 (2019).
65. Friedrich, J. & Paninski, L. Fast active set methods for online spike inference from calcium imaging. In *Proc. 30th International Conference on Neural Information Processing System* (eds Lee, D. D. & von Luxburg, U.) 1984–1992 (Curran, 2016).
66. Wu, J. et al. An integrated imaging sensor for aberration-corrected 3D photography. *Nature* **612**, 62–71 (2022).
67. Zeng, Y. Source code for 'High-fidelity intravital imaging of biological dynamics via with latent-space-enhanced digital adaptive optics'. *GitHub* https://github.com/TristaZeng/LEAO (2025).
68. Zhang, Y. et al. Rapid detection of neurons in widefield calcium imaging datasets after training with synthetic data. *Nat. Methods* **20**, 747–754 (2023).
69. Song, A., Gauthier, J. L., Pillow, J. W., Tank, D. W. & Charles, A. S. Neural anatomy and optical microscopy (NAOMi) simulation for evaluating calcium imaging methods. *J. Neurosci. Methods* **358**, 109173 (2021).

Acknowledgements

We thank R. Zhang and S. Li for their help and advice in the visualization. J.W. was supported by Beijing Natural Science Foundation (grant nos. Z240011 and JR25021), Natural Science Foundation of China (grant nos. 62222508 and 62525506) and New Cornerstone Science Foundation through the XPLORER PRIZE. Q.D. was supported by Natural Science Foundation of China (grant no. 62088102) and Beijing Key Laboratory of Cognitive Intelligence. Z.L. was supported by the Young Scientists Fund of Beijing Natural Science Foundation (grant no. 4254114), the National Postdoctoral Program for Innovative Talent (grant no. BX20230174), the Postdoctoral Science Foundation of China (grant no. 2023M741963), the Shuimu Tsinghua Scholar Program (grant no. 2023SM065) and Natural Science Foundation of China (grant no. 62575154). Q.Z. was supported by the

Postdoctoral Science Foundation of China (grant no. 2023M741963) and funding from Tsinghua-Peking Center for Life Sciences.

Author contributions

Q.D., J.W. and Z.L. supervised the project. Yunmin Zeng, Q.D., J.W. and Z.L. designed and initiated the project. Y. Zeng designed detailed implementations, performed the numerical simulation and developed the LEAO framework with conceptual advice from Z.L. Yuanlong Zhang, Z.L. and J.W. designed the biological experiments. Q.Z., Y. Zeng, S.K., Yunhao Zhang and M.W. prepared the samples and conducted biological experiments. Y. Zeng conducted the data processing and statistical analysis. Y.X., S.W. and Y. Zeng conducted the data visualization. Y. Zeng, Z.L., J.W. and Q.D. wrote the manuscript with input from all authors.

Competing interests

Q.D. and J.W. are founders and equity holders of Zhejiang Hehu Technology, which commercializes LEAO, described in this work. Q.D., Y. Zeng, Z.L. and J.W. submitted patent applications related to the LEAO technology described in this work. The other authors declare no competing interests.

Additional information

Supplementary information The online version contains supplementary material available at https://doi.org/10.1038/s41587-026-03107-2.

Correspondence and requests for materials should be addressed to Zhi Lu, Jiamin Wu or Qionghai Dai.

Peer review information *Nature Biotechnology* thanks Qi Hu, Lei Tian and the other, anonymous, reviewer(s) for their contribution to the peer review of this work. Peer reviewer reports are available.

nature portfolio

Corresponding author(s): Zhi Lu, Jiamin Wu, Qionghai Dai

Last updated by author(s): Mar 13, 2026

Reporting Summary

Nature Portfolio wishes to improve the reproducibility of the work that we publish. This form provides structure for consistency and transparency in reporting. For further information on Nature Portfolio policies, see our Editorial Policies and the Editorial Policy Checklist.

Statistics

For all statistical analyses, confirm that the following items are present in the figure legend, table legend, main text, or Methods section.

n/a	Confirmed
☐	☒ The exact sample size (*n*) for each experimental group/condition, given as a discrete number and unit of measurement
☐	☒ A statement on whether measurements were taken from distinct samples or whether the same sample was measured repeatedly
☒	☐ The statistical test(s) used AND whether they are one- or two-sided *Only common tests should be described solely by name; describe more complex techniques in the Methods section.*
☒	☐ A description of all covariates tested
☒	☐ A description of any assumptions or corrections, such as tests of normality and adjustment for multiple comparisons
☐	☒ A full description of the statistical parameters including central tendency (e.g. means) or other basic estimates (e.g. regression coefficient) AND variation (e.g. standard deviation) or associated estimates of uncertainty (e.g. confidence intervals)
☒	☐ For null hypothesis testing, the test statistic (e.g. *F*, *t*, *r*) with confidence intervals, effect sizes, degrees of freedom and *P* value noted *Give P values as exact values whenever suitable.*
☒	☐ For Bayesian analysis, information on the choice of priors and Markov chain Monte Carlo settings
☒	☐ For hierarchical and complex designs, identification of the appropriate level for tests and full reporting of outcomes
☒	☐ Estimates of effect sizes (e.g. Cohen's *d*, Pearson's *r*), indicating how they were calculated

Our web collection on statistics for biologists contains articles on many of the points above.

Software and code

Policy information about availability of computer code

Data collection	All experimental data were acquired using customized acquisition software. All simulated neuronal data were generated using the Neural Anatomy and Optical Microscopy package and its modifications.
Data analysis	All performance analyses were performed with customized MATLAB (MathWorks, MATLAB R2024a) scripts and Python (v3.9.7) scripts. All 3D renderings and the tracking in Figs. 3-5 are performed using Imaris (v9.0). The python codes of LEAO for training and testing are publicly accessible on the GitHub repository (https://github.com/TristaZeng/LEAO).

For manuscripts utilizing custom algorithms or software that are central to the research but not yet described in published literature, software must be made available to editors and reviewers. We strongly encourage code deposition in a community repository (e.g. GitHub). See the Nature Portfolio guidelines for submitting code & software for further information.

Data

Policy information about availability of data

All manuscripts must include a data availability statement. This statement should provide the following information, where applicable:

- Accession codes, unique identifiers, or web links for publicly available datasets
- A description of any restrictions on data availability
- For clinical datasets or third party data, please ensure that the statement adheres to our policy

Downloading links to example data used for demonstrations are available on our GitHub repository (https://github.com/TristaZeng/LEAO). All simulated neuronal

data were generated using the Neural Anatomy and Optical Microscopy package and its modifications67,68. Other simulated data used the open-source dataset by Allen Institute (https://www.allencell.org/data-downloading.html#DownloadImageData). Source data are provided with this paper.

Research involving human participants, their data, or biological material

Policy information about studies with human participants or human data. See also policy information about sex, gender (identity/presentation), and sexual orientation and race, ethnicity and racism.

Reporting on sex and gender	No human research participants in this study.
Reporting on race, ethnicity, or other socially relevant groupings	No human research participants in this study.
Population characteristics	No human research participants in this study.
Recruitment	No human research participants in this study.
Ethics oversight	No human research participants in this study.

Note that full information on the approval of the study protocol must also be provided in the manuscript.

Field-specific reporting

Please select the one below that is the best fit for your research. If you are not sure, read the appropriate sections before making your selection.

☒ Life sciences ☐ Behavioural & social sciences ☐ Ecological, evolutionary & environmental sciences

For a reference copy of the document with all sections, see nature.com/documents/nr-reporting-summary-flat.pdf

Life sciences study design

All studies must disclose on these points even when the disclosure is negative.

Sample size	All sample sizes are stated in the figure legends. Sample sizes were chosen based on previous studies using similar imaging approaches and were sufficient to observe reproducible effects across independent experiments.
Data exclusions	No data were excluded for the analysis.
Replication	Biological data shown in Figs. 3, 4 and Supplementary Videos 2, 3 are representative of n=10 experiments. Biological data shown in Fig. 5, Supplementary Figs. 13, 14 and Supplementary Video. 4 are representative of n=6 experiments. Simulated data are representative of n=12 experiments. All replications successful.
Randomization	Randomization was not used because all samples were derived from the same source and treated identically.
Blinding	Blinding was not relevant to this study, since no group allocation was performed.

Reporting for specific materials, systems and methods

We require information from authors about some types of materials, experimental systems and methods used in many studies. Here, indicate whether each material, system or method listed is relevant to your study. If you are not sure if a list item applies to your research, read the appropriate section before selecting a response.

Materials & experimental systems

n/a	Involved in the study
☐	☒ Antibodies
☒	☐ Eukaryotic cell lines
☒	☐ Palaeontology and archaeology
☐	☒ Animals and other organisms
☒	☐ Clinical data
☒	☐ Dual use research of concern
☒	☐ Plants

Methods

n/a	Involved in the study
☒	☐ ChIP-seq
☒	☐ Flow cytometry
☒	☐ MRI-based neuroimaging

Antibodies

Antibodies used	PE-Ly6G. Supplier: BioLegend. Catalog number: #127608. Clone name: 1A8. Amount: 10μL per mouse.
Validation	The antibody was validated by the manufacturer: https://www.biolegend.com/en-us/products/pe-anti-mouse-ly-6g-antibody-4777

Animals and other research organisms

Policy information about studies involving animals; ARRIVE guidelines recommended for reporting animal research, and Sex and Gender in Research

Laboratory animals	For Fig. 3 and Supplementary Video. 2, dsRed-expressing mice (Jax 6051), OT-II mice (Jax 4194) and C57BL/6 (Jax 0664) mice aged 6-12 weeks were used. For Fig. 4 and Supplementary Video. 3, Rasgrf2-2A-dCre mice and Ai148 (TIT2L-GC6f-ICL-tTA2)-D mice were used. For Fig.5 and Supplementary Video. 4, 8-week-old wild-type C57BL/6 mice were used. For Supplementary Figs. 13, 14, 6-8 weeks Thy1-YFP (JAX: 003709) mice were used.
Wild animals	Not involved in this study.
Reporting on sex	The mice used in this study are male.
Field-collected samples	Not involved in this study.
Ethics oversight	Animal protocol procedures were reviewed and approved by the Institutional Animal Care and Use Committee office of Tsinghua University.

Note that full information on the approval of the study protocol must also be provided in the manuscript.

Plants

Seed stocks	No seed stocks or plant material are used in this study.
Novel plant genotypes	No seed stocks or plant material are used in this study.
Authentication	No seed stocks or plant material are used in this study.

nature biotechnology

Supplementary information

https://doi.org/10.1038/s41587-026-03107-2

High-fidelity intravital imaging of biological dynamics with latent-space-enhanced digital adaptive optics

In the format provided by the authors and unedited

Table of contents

Supplementary Fig. 16	Comparison of TIS imaging results of neutrophils and blood vessels with and without LEAO correction.
Supplementary Fig. 17	Rapid transfer learning of LEAO to a new sample type with a small training dataset.
Supplementary Fig. 18	Rapid transfer learning of LEAO to a new system with a small training dataset.
Supplementary Fig. 19	Ablation study to evaluate the transfer-learning capability of LEAO compared with a vanilla regressor.
Supplementary Fig. 20	Comparison of wide-field and light-field PSFs' intensity robustness to aberrations.
Supplementary Fig. 21	Comparison of LEAO and wide-field blind deconvolution.
Supplementary Fig. 22	Comparison of LEAO with wDAO.
Supplementary Fig. 23	Evaluation of LEAO on aberrations with higher Zernike order.
Supplementary Fig. 24	Diagram of wave-optics forward imaging model for LEAO.
Supplementary Fig. 25	Zernike convention used in LEAO.
Supplementary Fig. 26	Performance of LEAO with increasing number of training data stacks.
Supplementary Table. 1	Implementation details of LEAO
Supplementary Table. 2	Imaging conditions of live-cell experiments
Supplementary Video. 1	The principle of LEAO enables it to correct not only inter-angle disparities but also intra-angle distortions based on wave-optics modeling, whereas DAO is

	limited to correcting only the former under a ray-optics framework.
Supplementary Video. 2	LEAO enables high-fidelity recording and large-scale tracking of ~ 5000 T cells across an entire mouse lymph node.
Supplementary Video. 3	LEAO enables high-fidelity mesoscale recording of multiregional neural activity in mouse cortex after correcting spatially non-uniform aberration.
Supplementary Video. 4	LEAO effectively combats severe aberration induced by the thick skull and polymer gel in TIS imaging, enabling continuous observation of neutrophil inflammatory response and repair process for over 10 hours after TBI in mouse intact skull.

Supplementary Figures

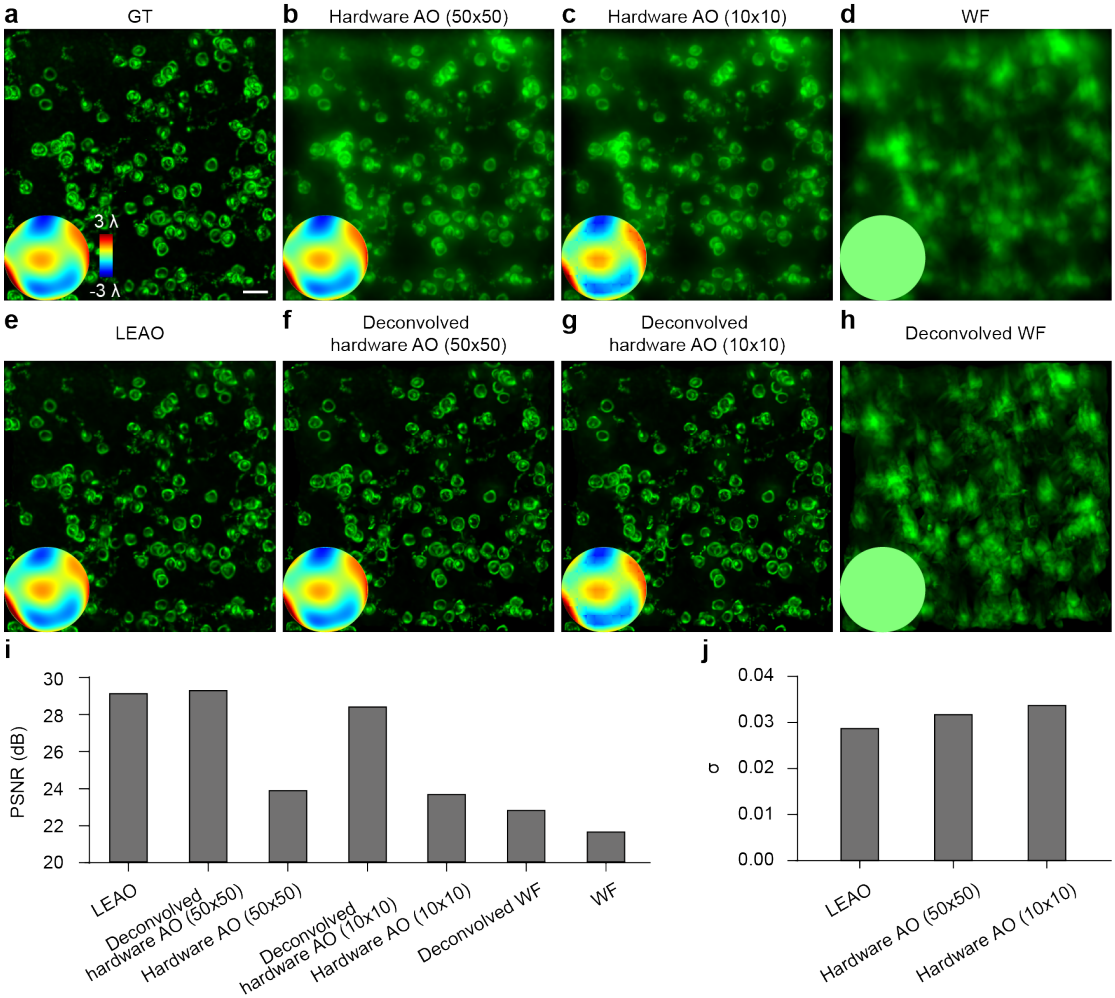

Supplementary Fig. 1 | Comparison of LEAO with closed-loop hardware adaptive optics. **a-h**, MIPs of the ground truth (**a**), wide-field results of hardware AO by 50×50 (**b**) and 10×10 (**c**) deformable mirrors (DM) and the raw aberrated image (**d**), LEAO result (**e**) and the deconvolved wide-field results of 50×50 (**f**), 10×10 (**g**) hardware AO and the raw aberrated image (**h**). Reference ground truth aberration wavefront and aberration wavefronts estimated by each method are shown in the insets. Simulation details of hardware AO could be found in Methods. **i**, PSNR evaluation of the images in **b**-**h**. **j**, Normalized residual aberration $\boldsymbol{\sigma}$ of the aberration wavefronts in **b**, **c**, **e**. Scale bar, 20 μm.

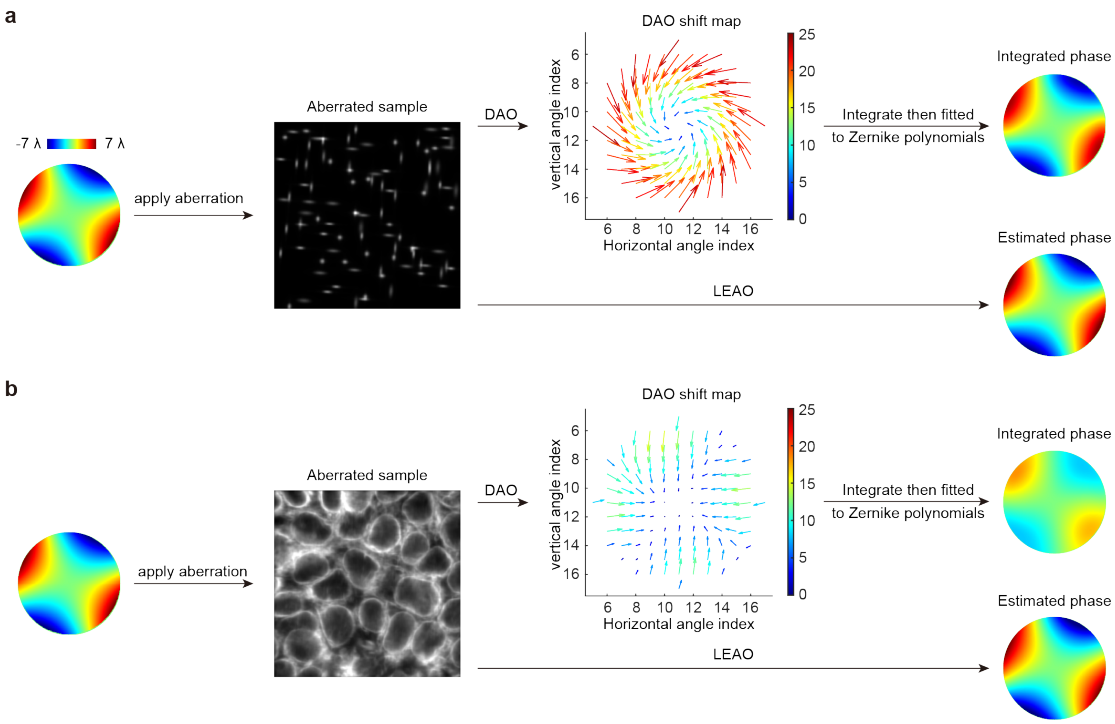

Supplementary Fig. 2 | The estimated phases by DAO and LEAO on two samples with different complexity. a, Both DAO and LEAO accurately yield a phase highly resembling the ground truth. **b**, DAO fails to accurately estimate the shift map of ER with more complicated structure, noise distribution and background fluorescence, leading to an off-amplitude phase estimation, while LEAO preserves the accuracy.

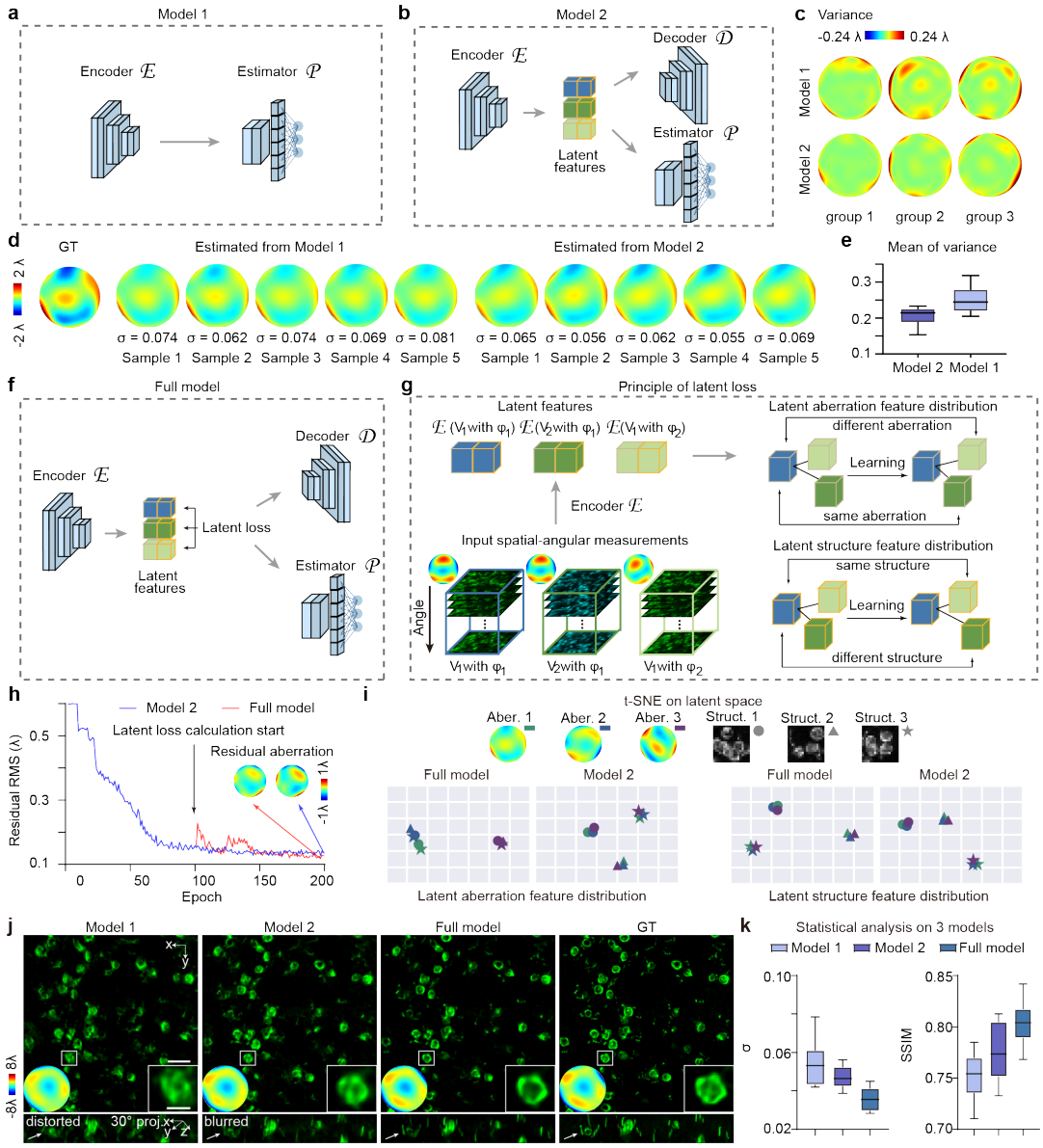

Supplementary Fig. 3 | Ablation study of LEAO architecture. a, The architecture of a vanilla aberration regressor, denoted as Model 1. **b**, The architecture of Model 2, which adds a decoder on the basis of Model 1 to form an auto-encoder branch for feature extraction. **c**, The variance of three representative groups of estimated aberration wavefronts by Model 1 (first row) and Model 2 (second row). Each group contains five estimated aberration wavefronts obtained from five distinct sample structures under the same aberration corruption. A lower variance indicates greater stability in aberration estimation. **d**, The unfolded five estimated aberration wavefronts derived from Model 1 and Model 2, with the ground truth wavefront shown as reference. Normalized residual aberration σ was calculated for each estimation, where lower values and smaller variance indicate better performance. **e**, The quantitative comparison of estimation variance between Model 1 and Model 2 (n = 10 groups, each group contains five estimated aberration wavefronts). Model 2 exhibits lower variance, indicating greater robustness to multifarious sample structures. **f**, The architecture of our LEAO, denoted as Full model, which adds a latent loss on the basis of Model 2. **g**, The principle of latent loss. Latent features extracted from the input LFM triplet are separated into two components encoding aberration and structure, respectively. Through optimization in the latent space using latent loss, feature distances are minimized for inputs sharing the same aberration or structure, and maximized for those with differing aberrations or structures. **h**,

Convergence curves of Model 2 and Full model across different training epochs, indicated by the residual aberration on test dataset. **i**, t-SNE analysis on latent features of Model 2 and Full model. **j**, Two directional maximum intensity projection (MIP) obtained by Model 1 (first column), Model 2 (second column), and Full model (third column). Zoomed-in regions of the white solid box are shown on the right bottom. Estimated aberration wavefronts are displayed in the insets. The ground truth image is shown in the right column with the input aberration. **k**, Normalized residual aberration σ and SSIM obtained by Model 1, Model 2 and Full model (n = 10 data stacks). Boxplot format: center line, medians; limits, 75% and 25%; whiskers, the larger value between the largest data point and the 75th percentiles plus 1.5× the interquartile range (IQR), and the smaller value between the smallest data point and the 25th percentiles minus 1.5× the IQR; outliers, data points larger than the upper whisker or smaller than the lower whisker. Scale bar, 20 μm (**j**), 10 μm (zoom-in regions in **j**).

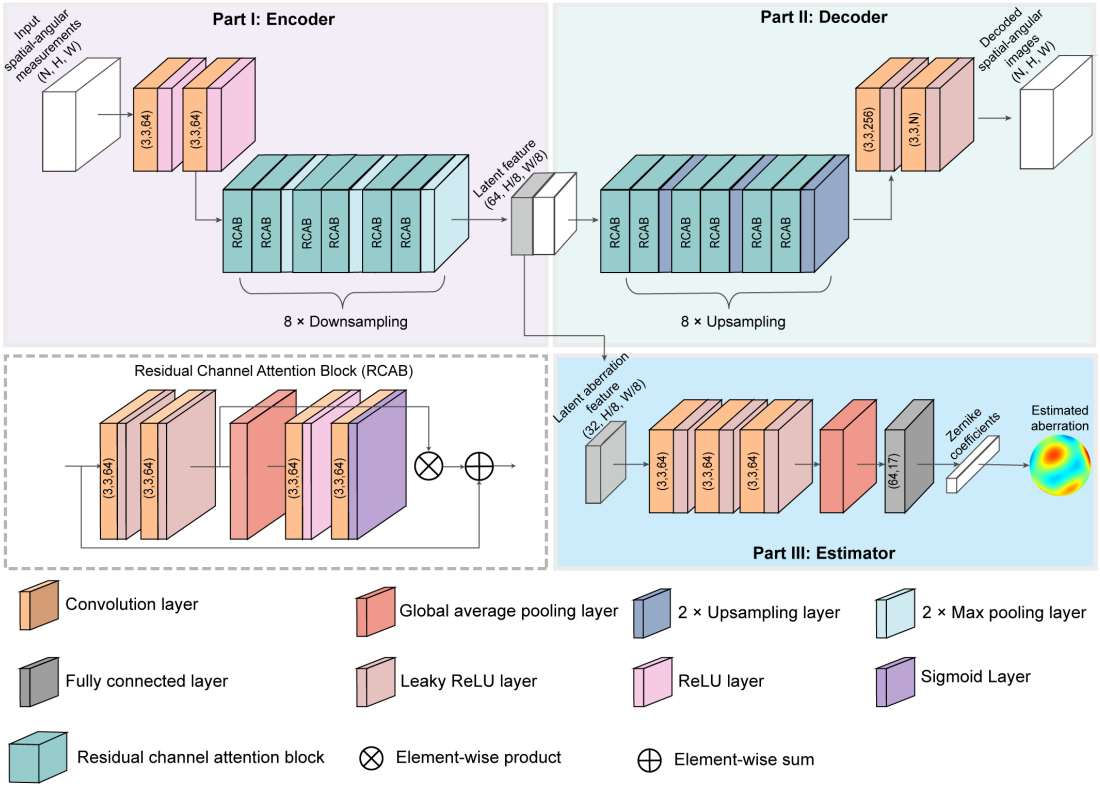

Supplementary Fig. 4 | Network architecture of LEAO. The architecture consists of three parts: an encoder, a decoder and an estimator. Features extracted from input spatial-angular measurements by the encoder-decoder branch are disentangled into representations encoding structure and aberration separately. The estimator then operates on the features encoding aberration to achieve high aberration estimation accuracy and improved robustness to changes in sample structure.

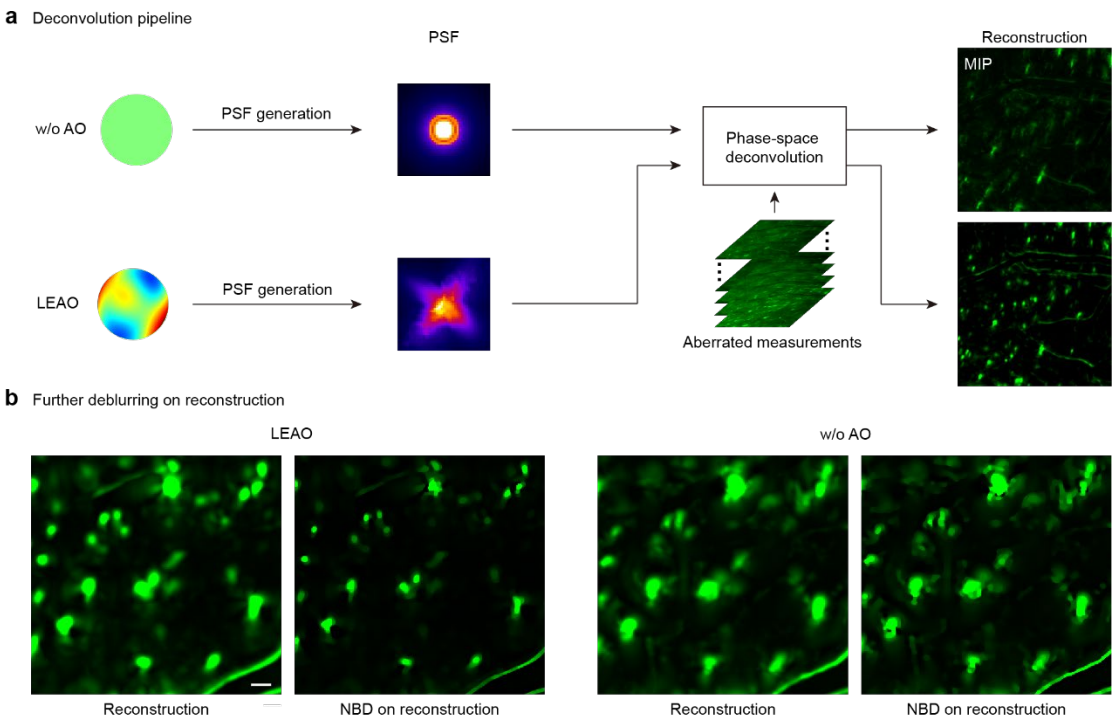

Supplementary Fig. 5 | Deconvolution pipeline and further deblurring results on reconstruction image. a, The deconvolution pipeline of LEAO and w/o AO. w/o AO utilizes ideal 4D phase-space PSFs[1] without aberration, while LEAO puts estimated aberration wavefront into the generation of PSFs. Example PSFs (MIP, center view) of w/o AO and LEAO are shown. With the PSFs, phase-space deconvolution is performed on the aberrated spatial-angular measurements to produce reconstruction results. **b**, MIPs of reconstruction results on mouse cortex from Fig. 4 by LEAO and w/o AO, and Normalized Blind Deconvolution (NBD)[2] on the reconstruction MIPs. This demonstrates blind deblurring techniques can be applied on the reconstruction results obtained through the pipeline in **a** to further enhance the image quality. Scale bar, 20 μm.

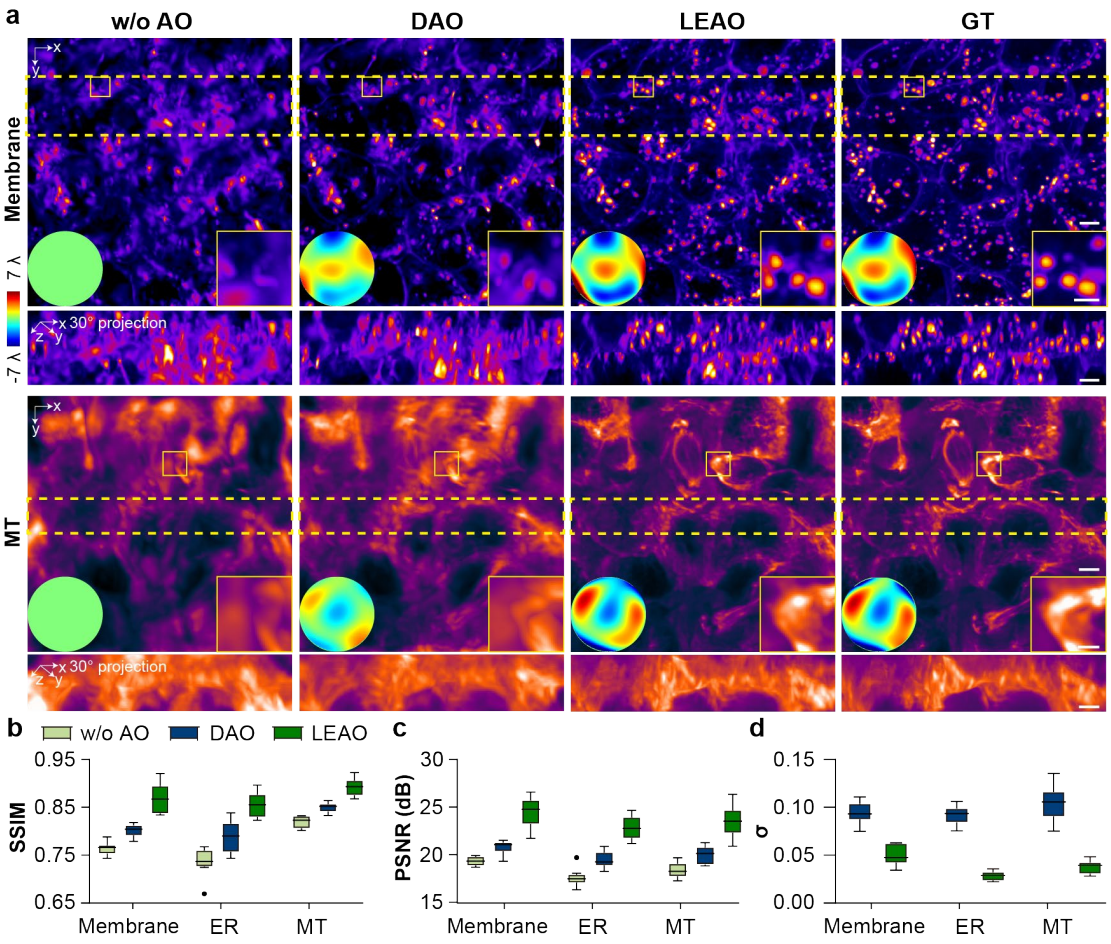

Supplementary Fig. 6 | Evaluation of LEAO on data of punctate and tubular structure. a, Two directional MIPs of cell membrane (first row) and MT (second row) images without AO (first column), with DAO (second column), and with LEAO (third column). Zoomed-in regions of the yellow solid box are shown on the right bottom. Regions corresponding to the 30° projection are marked by yellow dashed line. Estimated aberration wavefronts are displayed in the insets. The ground truth images are shown in the right column. Scale bar, 30 μm, 10 μm (zoom-in). **b**, **c**, SSIM (**b**) and PSNR (**c**) of images obtained by methods without AO, with DAO and with LEAO on three types of structures including cell membrane, ER and MT (n = 10 data stacks). **d**, Normalized residual σ estimated by DAO and LEAO (n = 10 data stacks). Boxplot format: center line, medians; limits, 75% and 25%; whiskers, the larger value between the largest data point and the 75th percentiles plus 1.5× the interquartile range (IQR), and the smaller value between the smallest data point and the 25th percentiles minus 1.5× the IQR; outliers, data points larger than the upper whisker or smaller than the lower whisker.

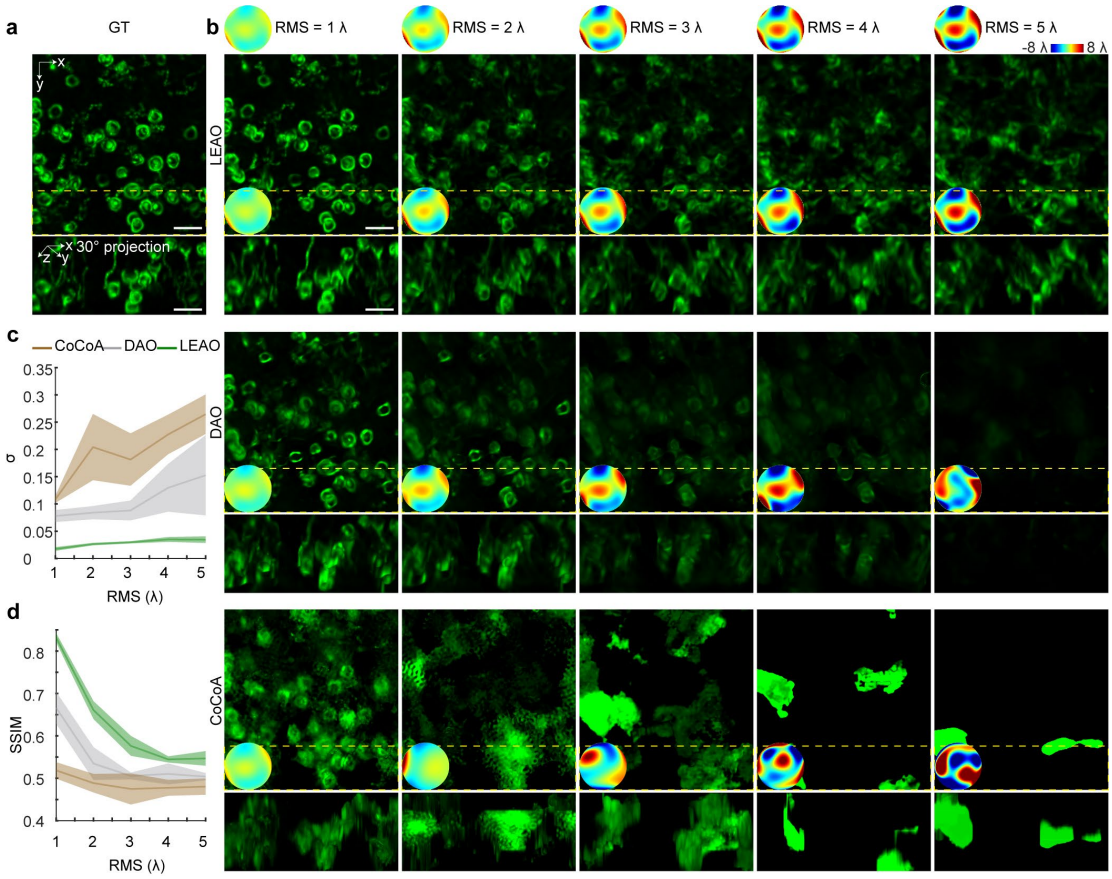

Supplementary Fig. 7 | Evaluation of LEAO's performance at increasing aberration levels. a, **b**, Two directional MIPs of the ground truth (**a**), and obtained by LEAO, DAO and CoCoA with induced aberration RMS ranging from 1 to 5 λ (**b**). Estimated aberration wavefronts are shown in the insets, with ground truth wavefronts displayed at the top. **c**, **d**, Normalized residual aberration σ (**c**) and SSIM (**d**) evaluation (n = 10 data stacks) comparing CoCoA, DAO and LEAO. Lineplot format: center line, mean value; shade, standard deviation. Scale bar, 20 μm.

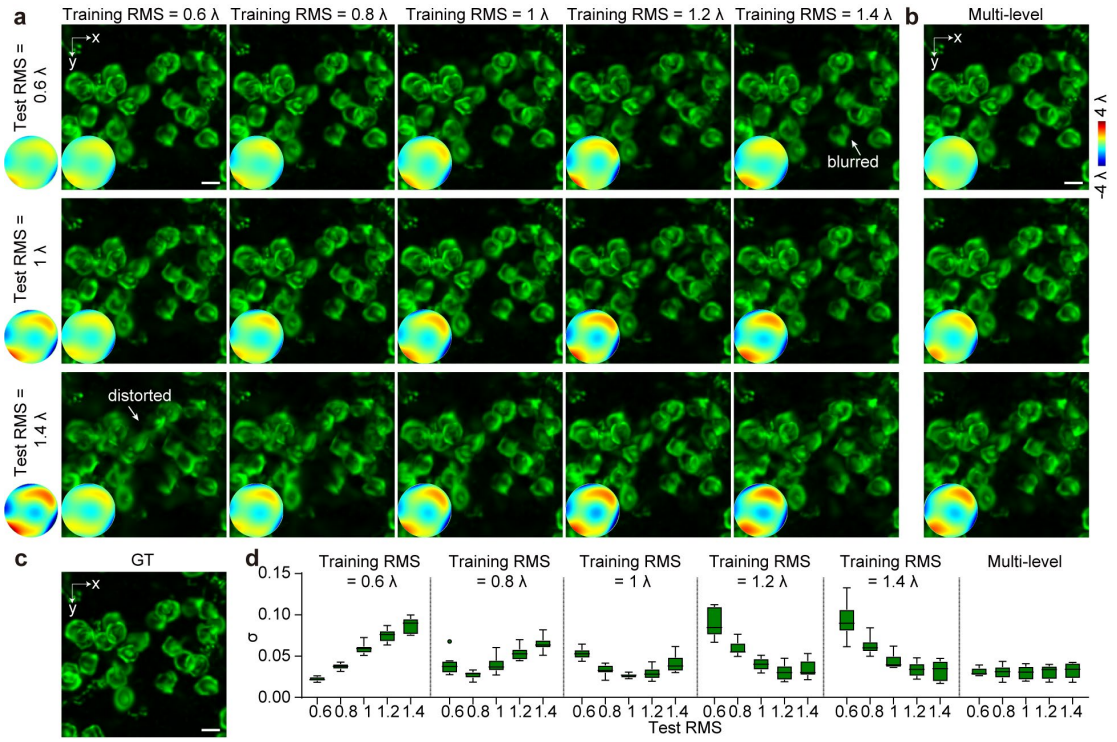

Supplementary Fig. 8 | Evaluation of LEAO on dataset with a wide range of aberration levels. a, MIPs of simulated neuron data obtained by LEAO with induced test aberration RMS of 0.6, 1 and 1.4 λ (from top to bottom). The induced aberration wavefronts are shown on the left. Each row corresponds to an LEAO model trained on a dataset containing only a single-level aberration with RMS of 0.6, 0.8, 1.0, 1.2 or 1.4 λ. Estimated aberration wavefronts by each model on each sample are shown in the insets. The bigger the gap between training and test aberration levels (images further away from the diagonal direction), the worse the aberration estimation accuracy and image quality. **b**, Corresponding results obtained using an LEAO model trained on a dataset containing multi-level aberrations. **c**, Ground truth. **d**, Normalized residual aberration σ for test data with induced aberration RMS from 0.6 to 1.4 λ, evaluated using LEAO models trained on aberration levels from 0.6 to 1.4 λ, respectively. The results obtained by LEAO trained on multiple aberration levels is shown in the right (n = 10 data stacks). Boxplot format: center line, medians; limits, 75% and 25%; whiskers, the larger value between the largest data point and the 75th percentiles plus 1.5× the interquartile range (IQR), and the smaller value between the smallest data point and the 25th percentiles minus 1.5× the IQR; outliers, data points larger than the upper whisker or smaller than the lower whisker. Scale bar, 10 μm.

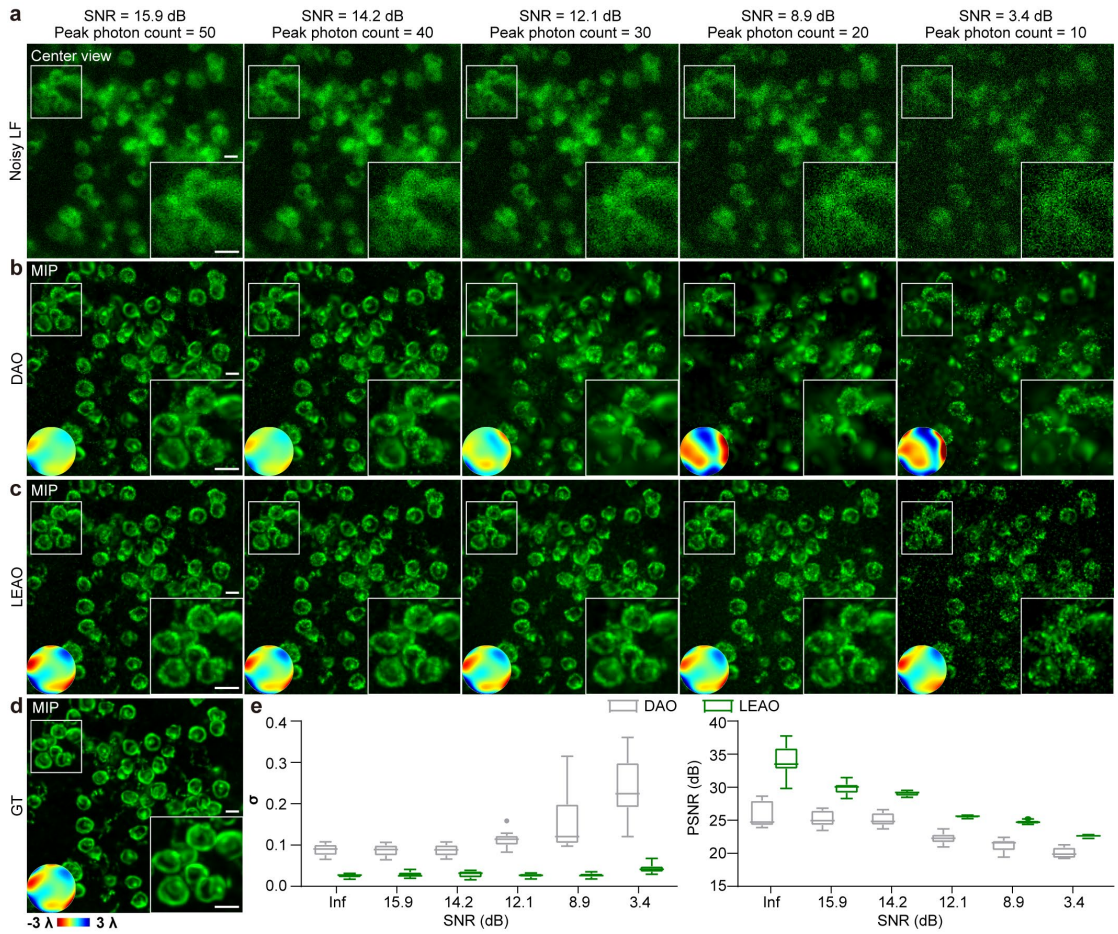

Supplementary Fig. 9 | Evaluation of LEAO's performance at increasing noise levels. a, **b**, **c**, Center views (**a**), MIPs of reconstruction with DAO (**b**) and MIPs of reconstruction with LEAO (**c**) with peak photon count ranging from 50 to 10 (left to right). The peak photon count is defined as the 99.9th percentile of intensity values in the spatial-angular measurements. A Gaussian noise of standard deviation 4 and a Poisson noise simulating the photon shot noise were added. Estimated aberration wavefronts are shown in the insets. **d**, Ground truth counterparts without noise. Aberration wavefronts in **b**-**d** share the same scale bar. **e**, PSNR and Normalized residual aberration σ evaluation comparing LEAO and DAO on noisy spatial-angular measurements with different SNRs (n = 10 data stacks). These statistical analyses validated that LEAO's estimation accuracy does not degrade until an SNR of 3.4 dB is reached. Boxplot format: center line, medians; limits, 75% and 25%; whiskers, the larger value between the largest data point and the 75th percentiles plus 1.5× the interquartile range (IQR), and the smaller value between the smallest data point and the 25th percentiles minus 1.5× the IQR; outliers, data points larger than the upper whisker or smaller than the lower whisker. Scale bar, 10 μm.

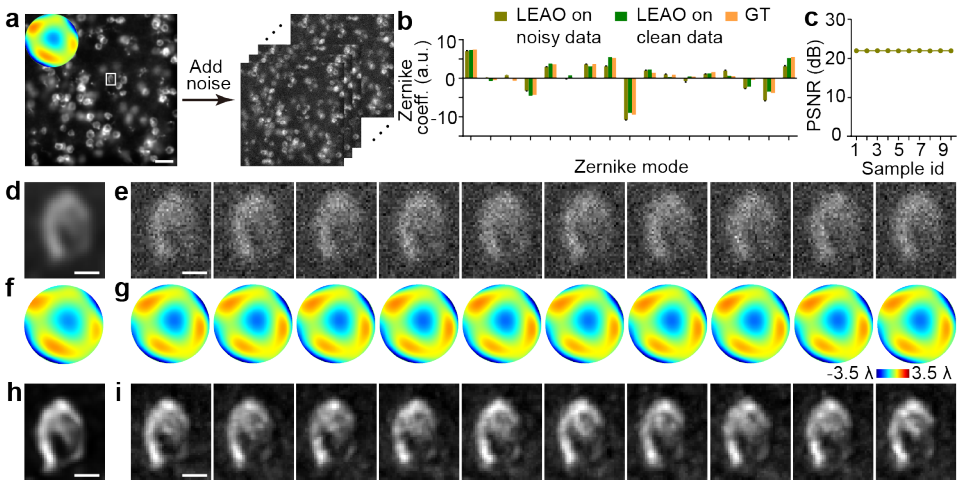

Supplementary Fig. 10 | Evaluation of LEAO's performance stability to random noise. a, Generation of 10 spatial-angular measurements stacks with randomly different noise patterns from the same clean measurement. Only the center view is shown here. Ground truth aberration wavefront is shown on the left top. **b**, Zernike coefficient distribution under ANSI indexing of LEAO on noisy data (n = 10 noisy data, bar plot format: bar, mean value; whisker, standard deviation), LEAO on clean data (n = 1), and ground truth. The index discards the piston, tilt and defocus modes (Methods). **c**, PSNR evaluation of LEAO images with different noise patterns (n = 10 data stacks). **d**, Zoomed-in of the clean area marked by white line in **a**. **e**, Corresponding noisy zoomed-ins. **f**, **g**, Estimated aberration by LEAO on the clean data (**f**) and noisy data (**g**). **h**, **i**, Reconstruction results on clean (**h**) and noisy data (**i**), displayed as MIPs. Both the qualitative and quantitative analysis validate that random noise does not affect the performance of LEAO. Scale bar, 30 μm (**a**), 5 μm (**d**, **e**, **h**, **i**).

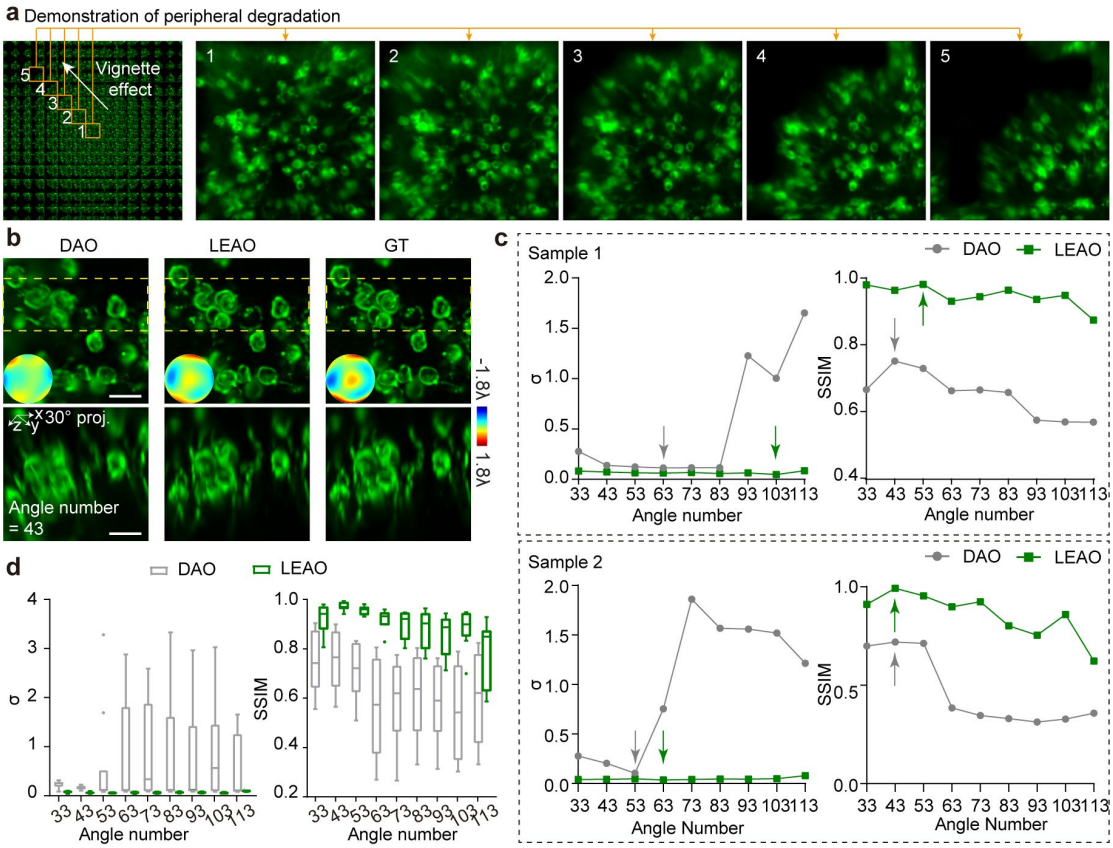

Supplementary Fig. 11 | Evaluation of LEAO's performance on different angle numbers. a, Representative views of the raw spatial-angular measurements. Misalignment of optical elements, aberrations and other factors form the vignette effect, resulting in the nonuniform intensity distribution in peripheral angular measurements. Hence, the optimal angle number for aberration estimation is unknown. **b**, Two directional MIPs obtained by DAO (first column), LEAO (second column) and ground truth (third column) at DAO's optimal angle number of 43. Aberration wavefronts are shown in the insets. **c**, Normalized residual aberration σ and SSIM evaluation comparing LEAO and DAO on two samples at different angle numbers. The grey arrow marks DAO's optimal angle number, and the green arrow marks LEAO's. **d**, Normalized residual aberration σ and SSIM evaluation ($n = 10$ data stacks) comparing LEAO and DAO on a larger test dataset. Boxlot format: center line, medians; limits, 75% and 25%; whiskers, the larger value between the largest data point and the 75th percentiles plus 1.5× the interquartile range (IQR), and the smaller value between the smallest data point and the 25th percentiles minus 1.5× the IQR; outliers, data points larger than the upper whisker or smaller than the lower whisker. Scale bar, 10 μm.

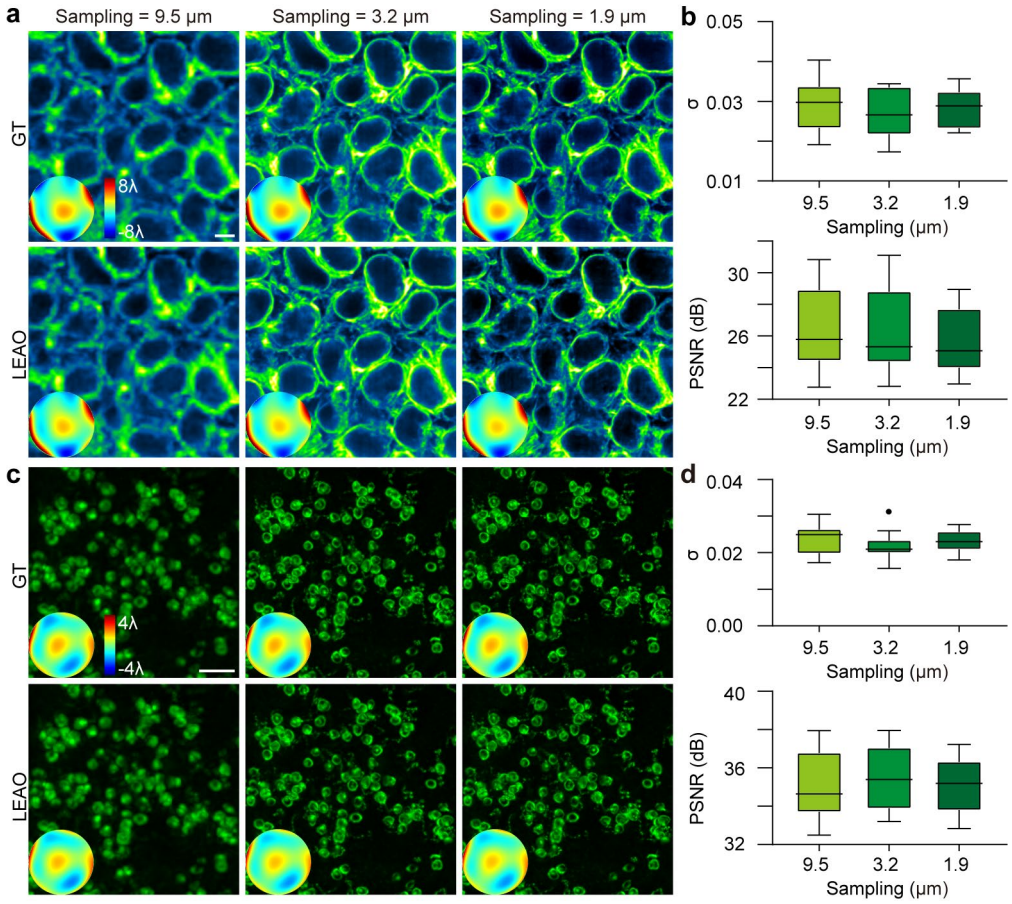

Supplementary Fig. 12 | Evaluation of LEAO's performance at different spatial sampling rates. a, MIPs of ground truth ER data (first row) and LEAO (second row), with spatial sampling rate = 9.5 μm, 3.2 μm and 1.5 μm. Aberration wavefronts are shown in the insets. **b**, Normalized residual aberration σ and PSNR evaluation on ER data (n = 10 data stacks). **c-d**, Corresponding results using simulated neuron data (n = 10 data stacks). Boxplot format: center line, medians; limits, 75% and 25%; whiskers, the larger value between the largest data point and the 75th percentiles plus 1.5× the interquartile range (IQR), and the smaller value between the smallest data point and the 25th percentiles minus 1.5× the IQR; outliers, data points larger than the upper whisker or smaller than the lower whisker. Scale bar, 40 μm.

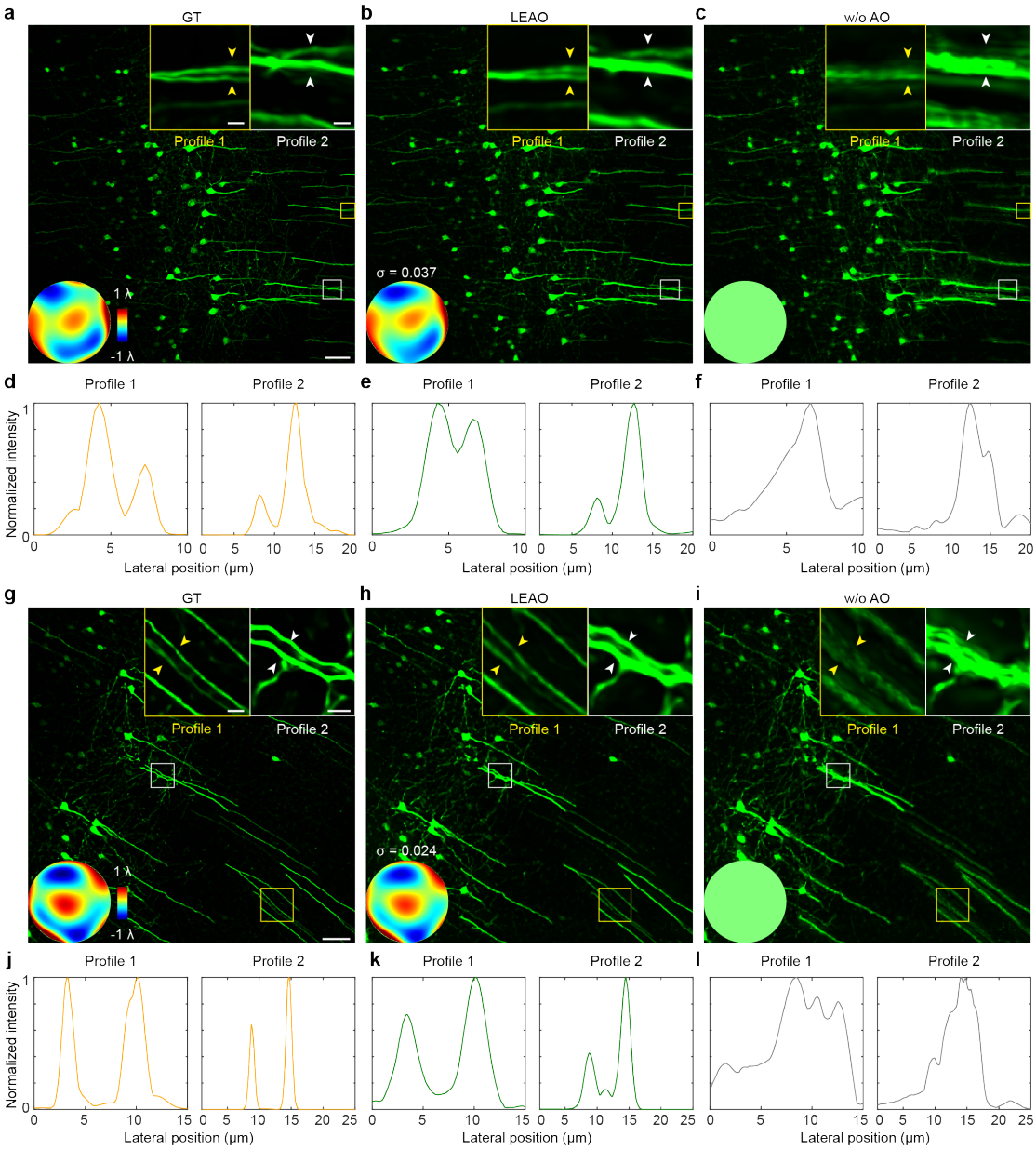

Supplementary Fig. 13 | LEAO on thin brain slices with artificially induced aberrations. **a-c**, MIPs of ground truth (**a**), LEAO (**b**) and w/o AO (**c**). Zoom-in regions are shown on the right top of each image. Ground truth images were reconstructed from aberration-free samples captured without any induced aberrations. Ground truth or estimated aberration wavefronts are shown on the left bottom. **d**, Intensity profiles of the structures marked by yellow (profile 1) and white (profile 2) arrows in **a**. **e**, Intensity profiles of the structures marked by yellow (profile 1) and white (profile 2) arrows in **b**. **f**, Intensity profiles of the structures marked by yellow (profile 1) and white (profile 2) arrows in **c**. **g-i**, MIPs of ground truth (**g**), LEAO (**h**) and w/o AO (**i**), on another sample. **j-l**, Intensity profiles of corresponding images, on another sample. Scale bar, 50 μm, 5 μm (zoom-in regions in **a-c**), 9 μm (zoom-in regions in **g-i**).

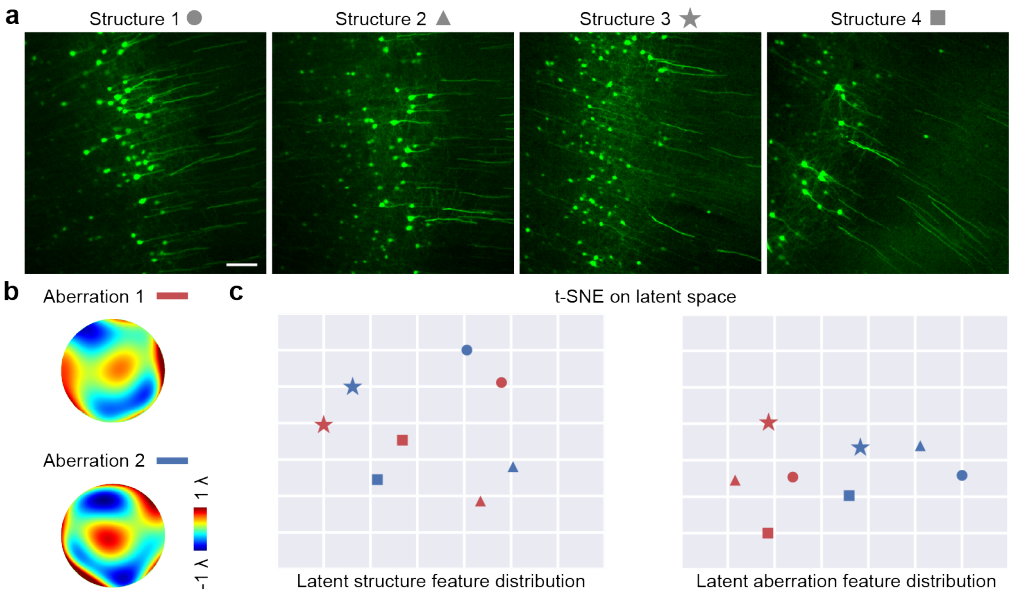

Supplementary Fig. 14 | Disentanglement measurement of LEAO on experimental data of a mouse brain slice. **a**, Four different regions from a mouse brain slice. **b**, Two induced aberration wavefronts from the two designed phase masks. **c**, t-distributed Stochastic Neighbor Embedding (t-SNE) analysis of latent features extracted from 8 measurements, comprising 4 types of sample structures shown in **a**, each contaminated by 2 different aberrations shown in **b**. Scale bar, 20 μm.

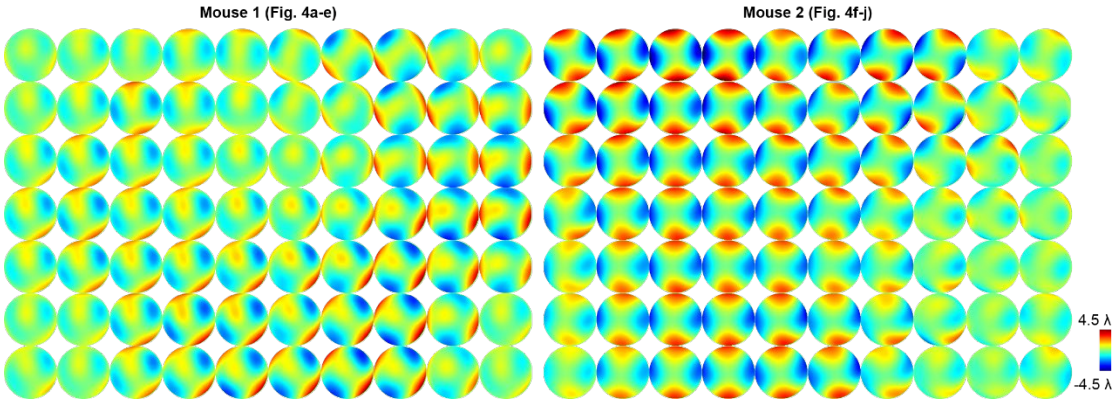

Supplementary Fig. 15 | Estimated phases by LEAO on two mice imaged by the same system. Mouse 1 is the source of Fig. 4a-e. Mouse 2 is the source of Fig. 4f-j.

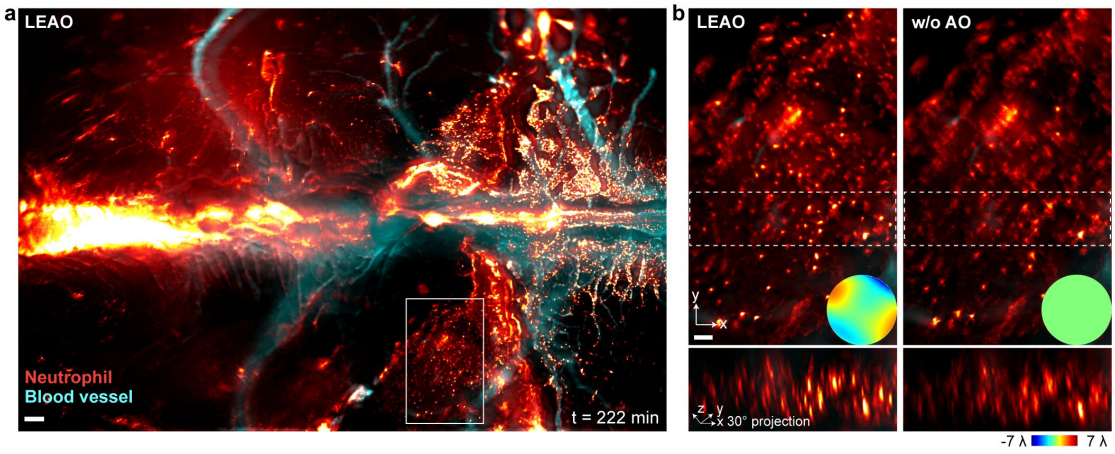

Supplementary Fig. 16 | Comparison of TIS imaging results of neutrophils and blood vessels with and without LEAO correction. **a**, MIP of intact mouse brain after TBI obtained by LEAO. **b**, Two directional MIPs of the area marked by white box in **a**. Estimated wavefronts are shown in the insets. Scale bar, 200 μm in **a**, 70 μm in **b**.

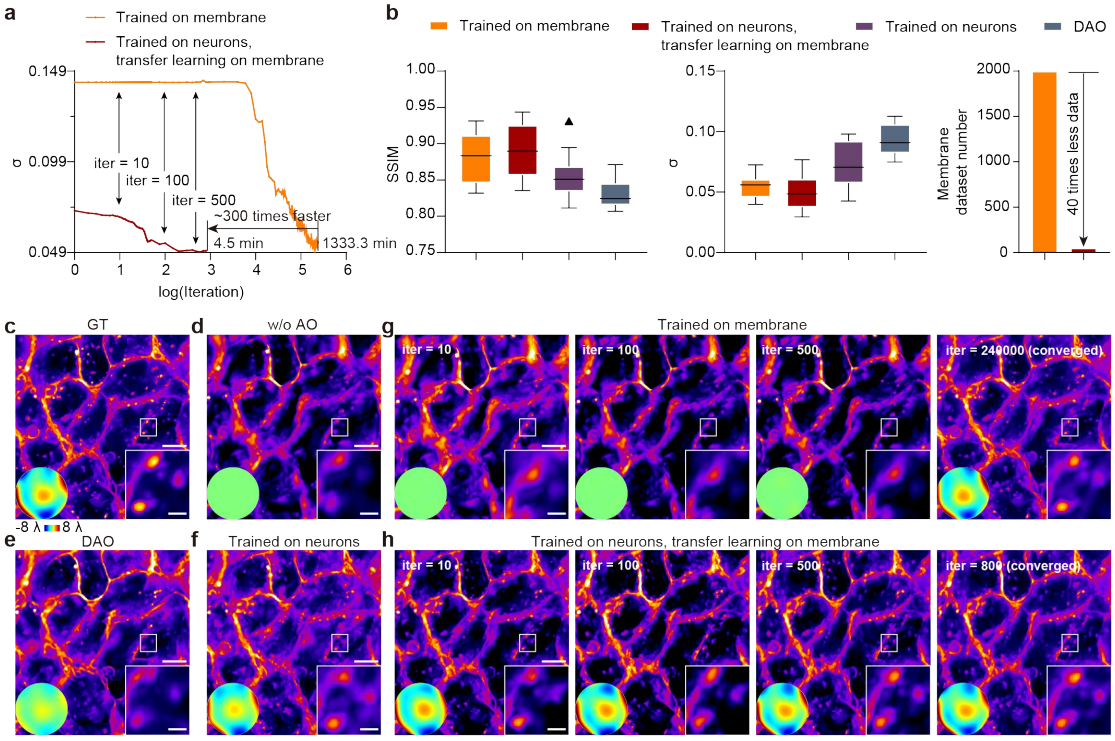

Supplementary Fig. 17 | Rapid transfer learning of LEAO to a new sample type with a small training dataset. a, Convergence curves of normalized residual aberration σ versus the number of iterations on a membrane test dataset. The iterations are presented on a logarithmic scale, with values of 10, 100 and 500 marked by arrows. The model trained on membrane dataset (grey line) took ~1333.3 minutes to converge, while the model first trained on simulated neuron dataset and then finetuned on membrane data (red line) converged in ~4.5 minutes. **b**, Boxplots showing SSIM and normalized residual aberration σ obtained by different LEAO models and DAO (n = 10 membrane data stacks). Boxplot format: center line, medians; limits, 75% and 25%; whiskers, the larger value between the largest data point and the 75th percentiles plus 1.5× the interquartile range (IQR), and the smaller value between the smallest data point and the 25th percentiles minus 1.5× the IQR; outliers, data points larger than the upper whisker or smaller than the lower whisker. The number of membrane data used for training is also plotted on the right, showing the LEAO model using transfer learning achieved performance comparable to that from training-from-scratch while using only 2.5% of the membrane data. **c-h**, The representative MIPs for the ground truth (**c**), the results without AO (**d**), the results with DAO (**e**), the results with different LEAO models (**f-h**). Ground truth and estimated aberration wavefronts are shown in the insets. Scale bar, 40 μm, 10 μm (zoom-in regions).

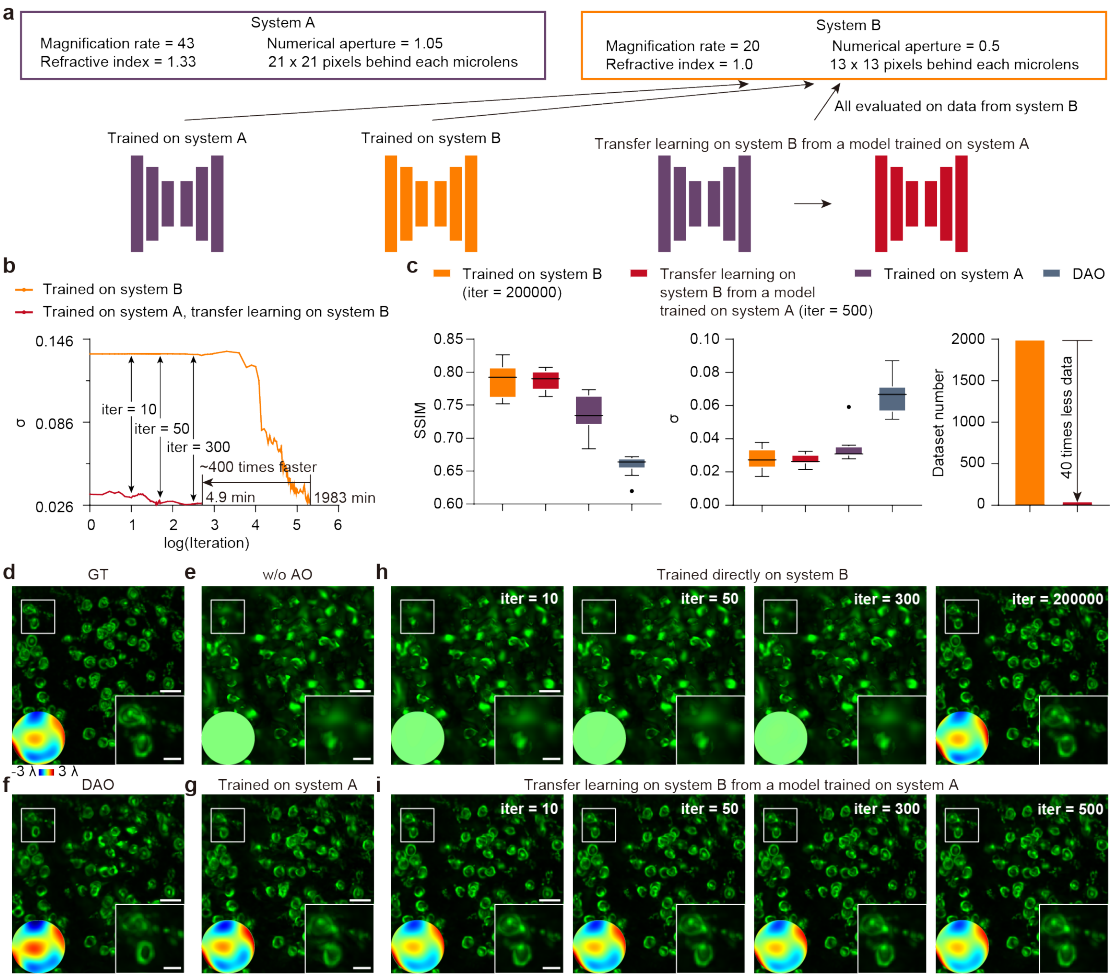

Supplementary Fig. 18 | Rapid transfer learning of LEAO to a new system with a small training dataset. a, Schematic of the experiment. Two distinct systems are used. The transfer learning of system A to system B was studied. All evaluations were conducted on data acquired from system B. **b**, Normalized residual aberration curve on test dataset by one model trained on system B and one model trained on system A then transferred to system B. The transfer learning was 400 times faster even with a conservative estimate that considers the transfer learning process to be converged at iteration 500. If we consider the transfer learning to be converged at iteration 50, which is reasonable given that the test loss at iteration 50 is similar to that at iteration 500, the process would even be 4000 times faster. **c**, Evaluation of SSIM and normalized residual aberration σ on test dataset by one model trained on system B, one model with transfer learning on system B from a model trained on system A, one model trained on system A, and DAO (n = 10 data stacks). Dataset number used by the model trained on system B and the model with transfer learning on system B are also shown on the right, showing that the transfer learning needs much fewer training data stacks compared to training from scratch. **d-i**, MIPs of ground truth (**d**), without AO (**e**), DAO (**f**), model trained on system A (**g**), model trained directly on system B (**h**), and model with transfer learning on system B from a model trained on system A (**i**). In **h** and **i**, results from key iterations are shown. The corresponding iterations are marked by black arrow in **b**. Ground truth (**d**) and estimated aberration wavefronts (**e-i**) are shown on the left bottom. Enlarged images of the region marked by white box are shown on the right bottom. Scale bar, 20 μm, 8 μm (zoom-in regions).

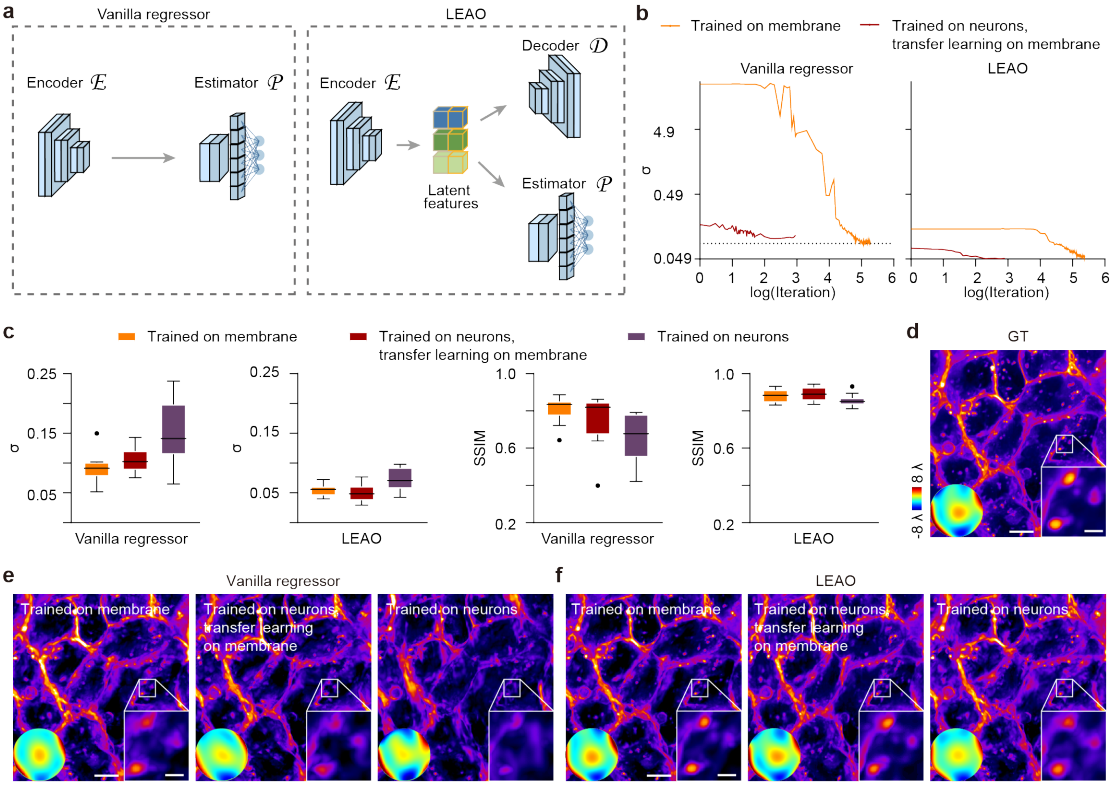

Supplementary Fig. 19 | Ablation study to evaluate the transfer-learning capability of LEAO compared with a vanilla regressor. a, The architecture of the vanilla regressor and LEAO. **b**, Convergence curves of normalized residual aberration σ versus the number of iterations on a membrane test dataset, by the vanilla regressor and LEAO, respectively. For the vanilla regressor, the model first trained on simulated neuron dataset and then finetuned on membrane data (red line) cannot reach the same accuracy level as the model trained on membrane dataset itself (orange line). For LEAO, the model trained on membrane dataset took ~1333.3 minutes to converge, while the finetuned model converged to the same accuracy level in ~4.5 minutes. **c**, Boxplots showing SSIM and normalized residual aberration σ obtained by different vanilla regressor models and different LEAO models (n = 10 data stacks). All used models were converged. Boxplot format: center line, medians; limits, 75% and 25%; whiskers, the larger value between the largest data point and the 75th percentiles plus 1.5× the interquartile range (IQR), and the smaller value between the smallest data point and the 25th percentiles minus 1.5× the IQR; outliers, data points larger than the upper whisker or smaller than the lower whisker. **d-f**, The representative MIPs for the ground truth (**d**), the results with different vanilla regressor models (**e**), and the results with different LEAO models (**f**). Ground truth and estimated aberration wavefronts are shown in the insets. Scale bar, 40 μm, 10 μm (zoom-in regions).

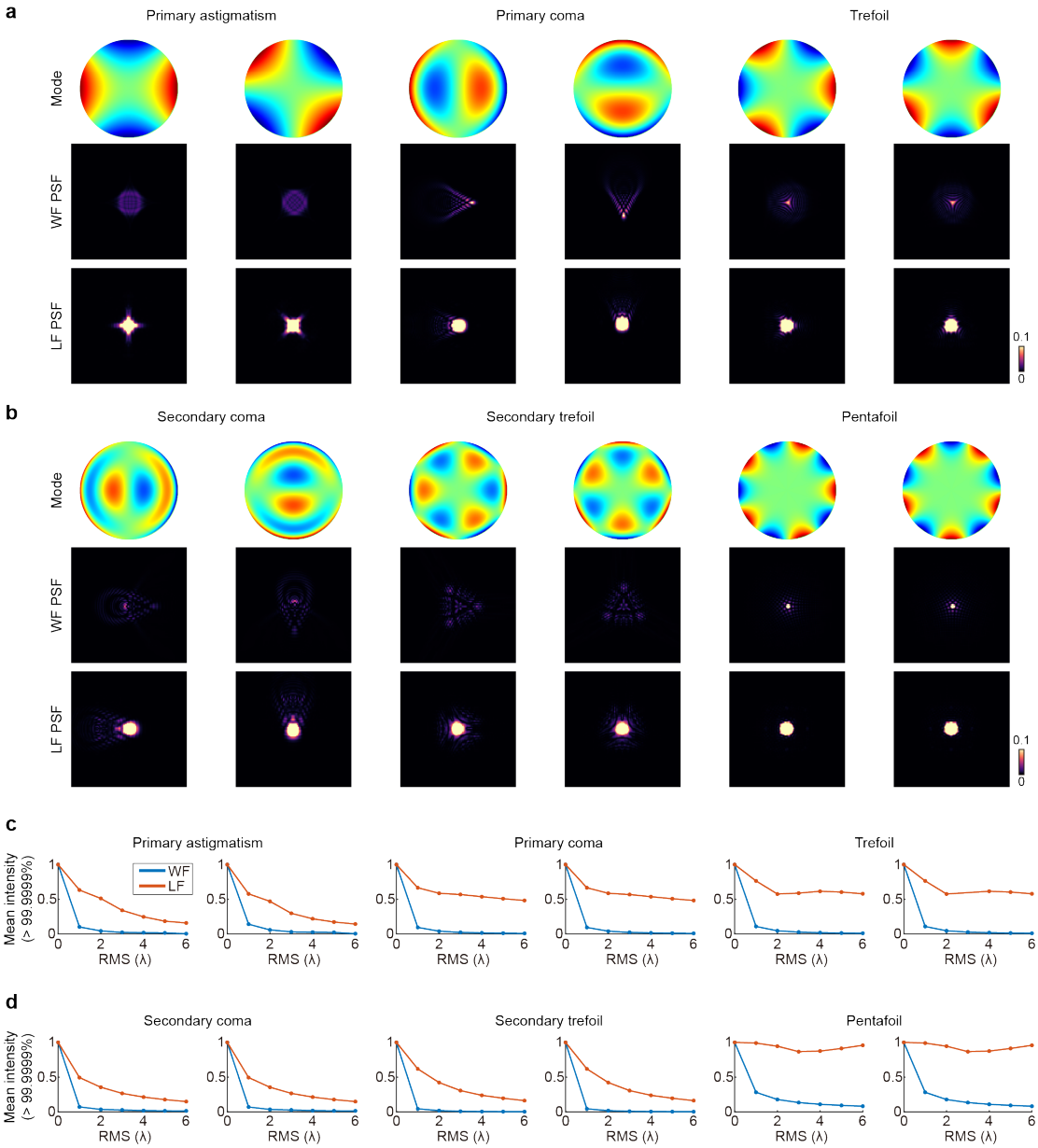

Supplementary Fig. 20 | Comparison of wide-field and light-field PSFs' intensity robustness to aberrations. a, **b**, Added aberration wavefronts (first row), MIPs of simulated WF PSFs (second row), and MIPs of the center angular component of simulated LF PSFs (third row) for Zernike modes of r = 2, 3 (**a**) and r = 5 (**b**). The aberration magnitude is 1 λ. **c**, **d**, The curve of normalized mean intensity (>99.9999 %) of WF and LF PSFs with increasing aberration magnitude from 0 to 6 λ for Zernike modes of r = 2, 3 (**c**) and r = 5 (**d**). The mean intensity (>99.9999 %) of a PSF is computed as the mean of all pixels exceeding the 99.9999 % intensity threshold in said PSF. Then this value is normalized so that it is 1 when without aberration.

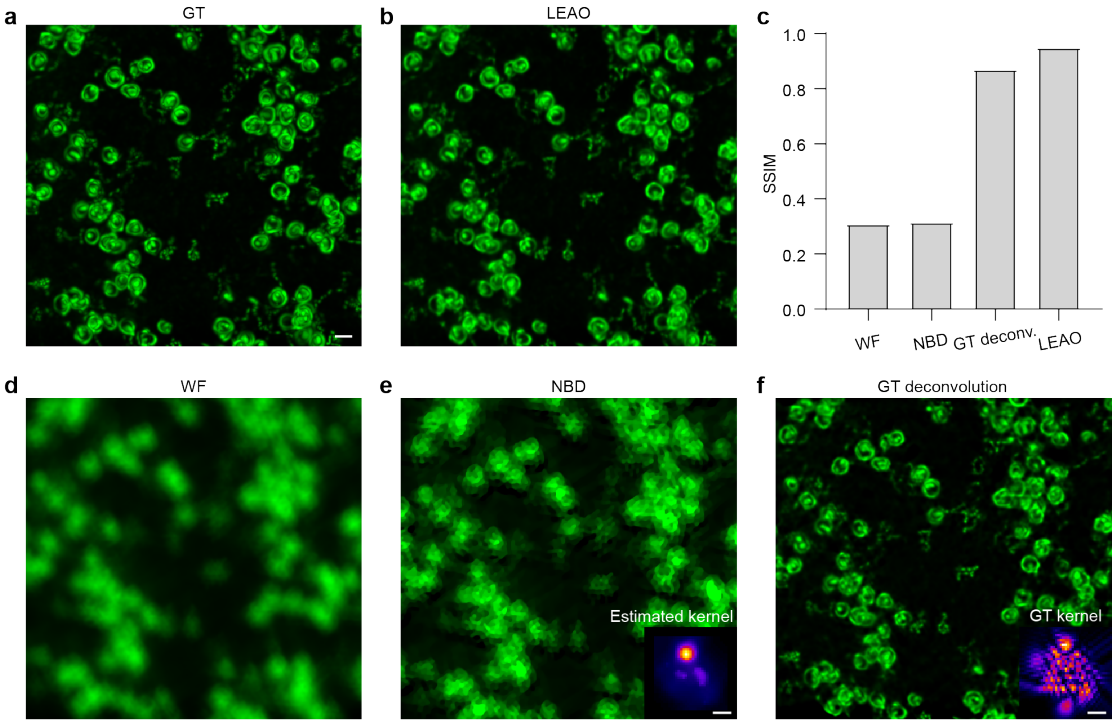

Supplementary Fig. 21 | Comparison of LEAO and wide-field blind deconvolution. a, Ground truth sample. **b**, LEAO reconstruction of aberrated light-field image. **c**, SSIM evaluation on images in **b**, **d**, **e**, **f**. **d**, Wide-field image of aberrated sample. **e**, NBD result of **d**. Estimated kernel by NBD is shown in the inset. **f**, Deconvolution with GT kernel on **d**. GT kernel is generated using the GT aberration wavefront. Scale bar, 10 μm, 3 μm (insets in **e**, **f**).

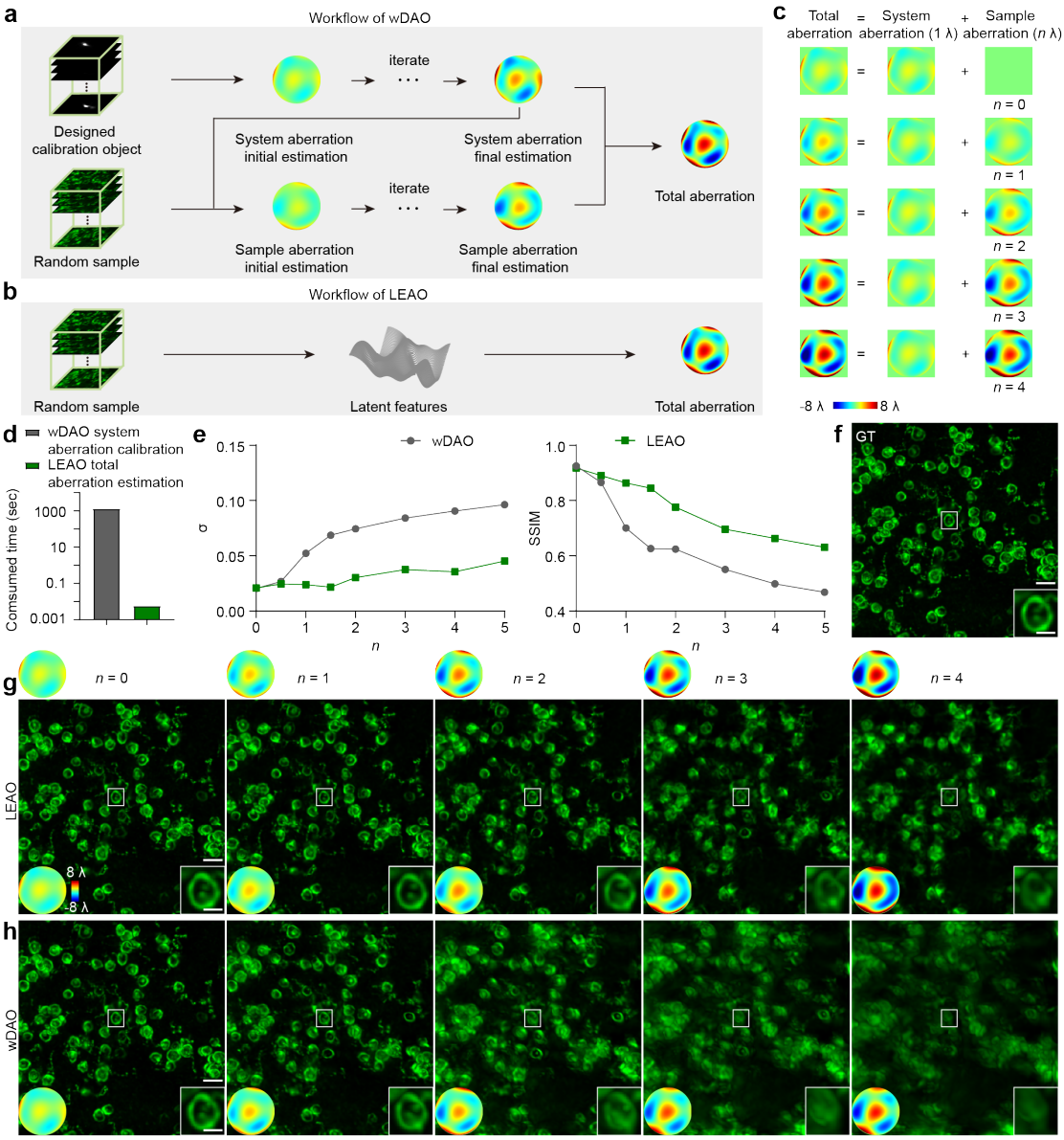

Supplementary Fig. 22 | Comparison of LEAO with wDAO. a, **b**, Workflows of wDAO (**a**) and LEAO (**b**). wDAO requires a specific, well-defined calibration object, typically a calibration chart or fluorescent beads, to iteratively perform calibration of the system aberration. Complex biological samples do not provide sufficiently clear features, so wDAO cannot converge reliably. When processing real biological samples that exhibit additional sample-specific aberrations, DAO will replace wDAO for aberration estimation, as it is more practical and avoids long-time recalibration for each new sample. In contrast, LEAO can simultaneously estimate both system and sample aberration on any samples with unknown aberration profiles. **c**, Illustration of total aberrations including system aberration (fixed) and increasing sample aberrations. **d**, Computation time of system aberration estimation by wDAO and total aberration estimation by LEAO. LEAO possesses a speed advantage of 5 orders of magnitude. **e**, Normalized residual aberration σ and SSIM obtained by wDAO and LEAO. **f**, MIP of ground truth. **g**, **h**, Corresponding LEAO and wDAO results for different sample aberration levels. Aberration wavefronts estimated by wDAO and LEAO are shown in the insets. Scale bar, 20 μm, 7 μm (zoom-in regions).

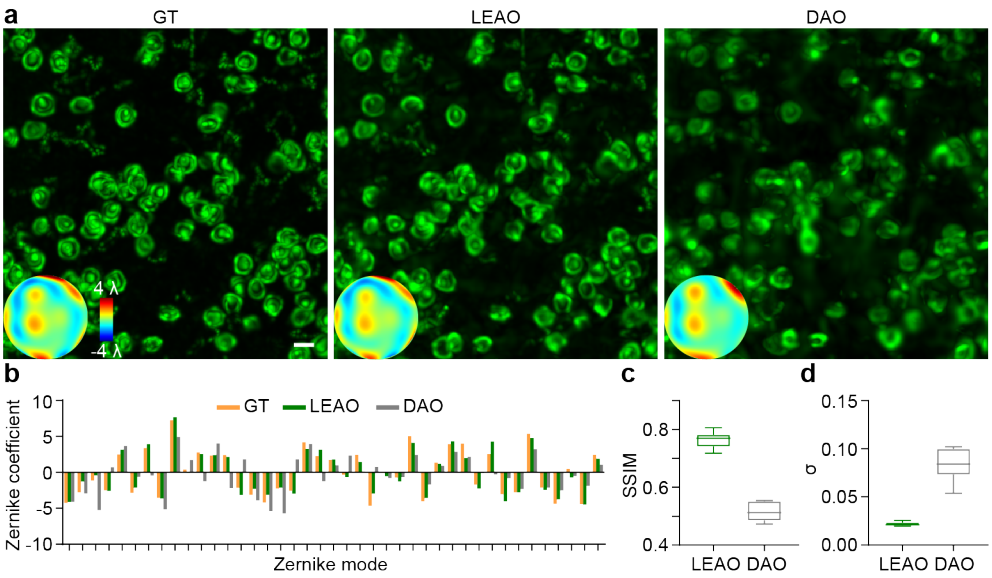

Supplementary Fig. 23 | Evaluation of LEAO on aberrations with higher Zernike order. a, MIPs of ground truth (first column), LEAO (second column) and DAO (third column). Ground truth and estimated aberration wavefronts are shown in the insets. **b**, Zernike coefficients of the aberration wavefronts shown in **a**, in ANSI order. A total of 41 modes were used, corresponding to the 0~8 radial order, except for piston, tip, tilt, and defocus. **c**, **d**, Evaluation of SSIM (**c**) and normalized residual aberration σ (**d**) on LEAO and DAO (n = 10 data stacks). Scale bar, 10 μm.

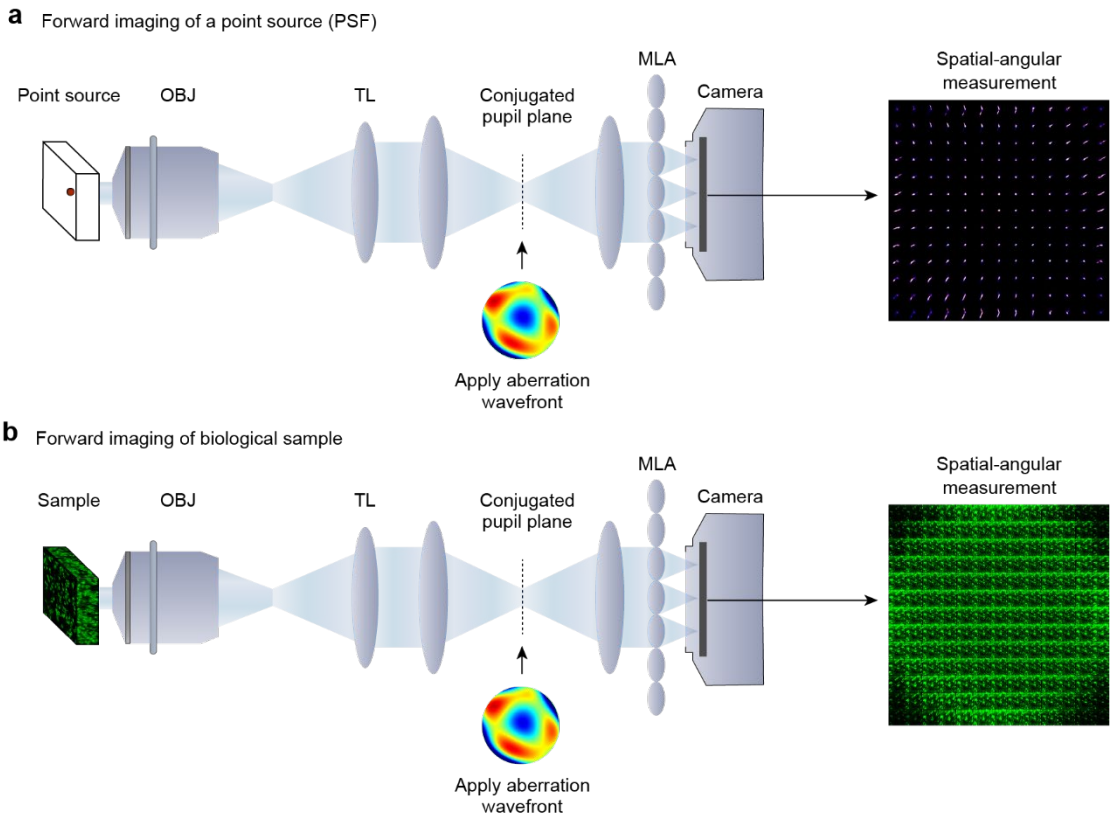

Supplementary Fig. 24 | Diagram of wave-optics forward imaging model for LEAO. a, **b**, Forward imaging of a point source (**a**) and biological sample (**b**). OBJ, objective lens. TL, tube lens. MLA, microlens array.

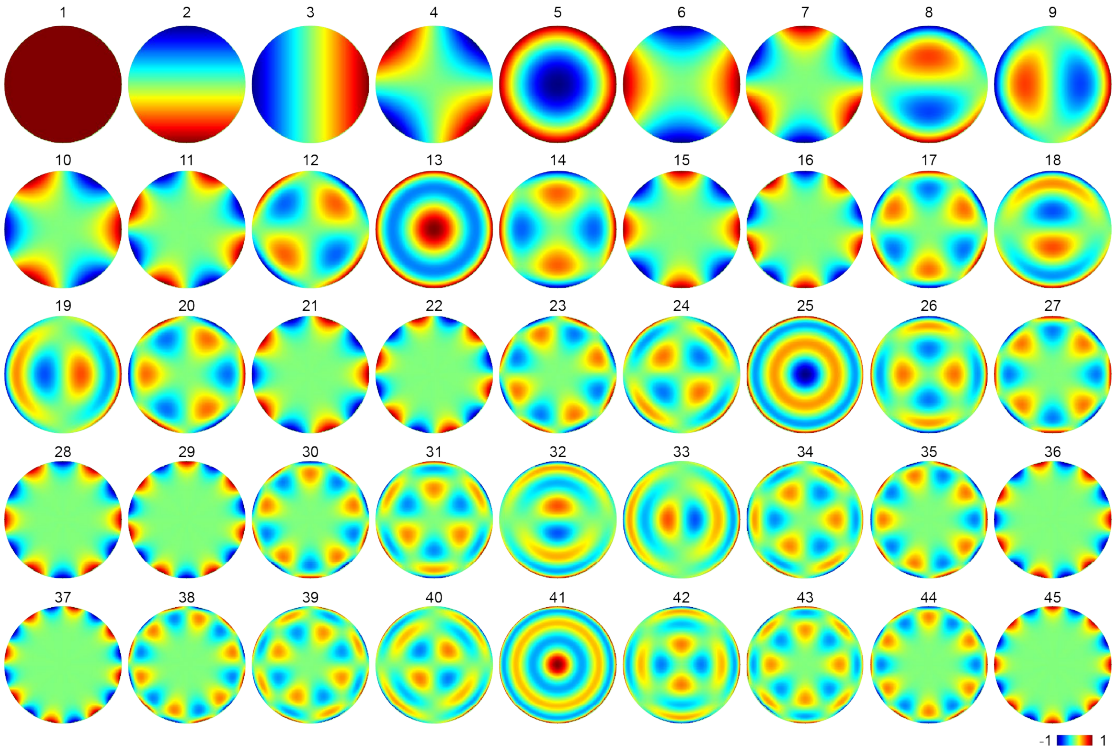

Supplementary Fig. 25 | Zernike convention used in LEAO. The sign, sequencing order and relative magnitude of the used Zernike polynomials are listed.

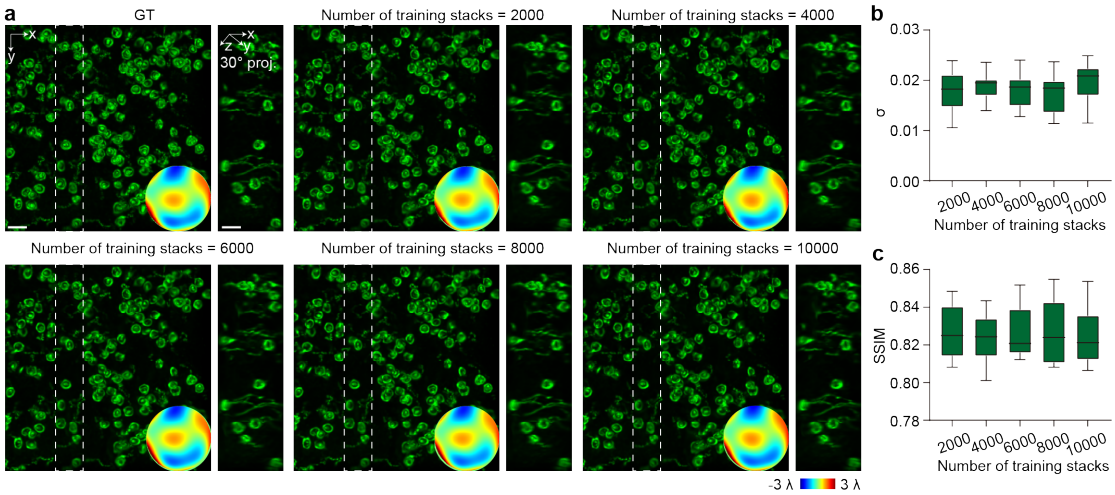

Supplementary Fig. 26 | Performance of LEAO with increasing number of training data stacks. a, Two directional MIPs obtained by LEAO models trained with 2000, 4000, 6000, 8000 and 10000 data stacks. GT is displayed at the left top for reference. Estimated aberration wavefronts are shown in the insets. **b**, **c**, Evaluation of normalized residual aberration σ (**b**) and SSIM (**c**) on the same test dataset (n = 10 data stacks for each training stack number). The evaluation validated that our choice of 2000 data stacks is sufficient for the training. Boxplot format: center line, medians; limits, 75% and 25%; whiskers, the larger value between the largest data point and the 75th percentiles plus 1.5× the interquartile range (IQR), and the smaller value between the smallest data point and the 25th percentiles minus 1.5× the IQR; outliers, data points larger than the upper whisker or smaller than the lower whisker. Scale bar, 20 μm.

Supplementary Tables

Supplementary Table 1. Implementation details of LEAO

	Training patch size	Training data number	Total training epochs	Training time (hours)	Inference patch size	Inference time (ms / patch)
Fig. 1 Supplementary Figs. 6, 12a	240 × 240 × 113	50	20 (transfer learning from a pre-trained model)	0.075	240 × 240 × 113	5.04
Fig. 2a, e, f Supplementary Figs. 1, 3, 7, 8a, 9, 10	280 × 280 × 113	2000	165	54.2	280 × 280 × 113	5.69
Fig. 2k, Supplementary Fig. 12c		2000	8 (transfer learning from a pre-trained model)	2.6		
Supplementary Fig. 8b		6000	100	98.7		
Supplementary Fig. 21		2000	40 (transfer learning from a pre-trained model)	13.2		
Fig. 2h, Supplementary Fig. 11	280 × 280 × 33	2000	165	22.3	280 × 280 × 33	4.78
	280 × 280 × 43			22.9	280 × 280 × 43	4.99
	280 × 280 × 53			24.9	280 × 280 × 53	5.23
	280 × 280 × 63			24.7	280 × 280 × 63	5.23
	280 × 280 × 73			30.9	280 × 280 × 73	5.31
	280 × 280 × 83			35.7	280 × 280 × 83	5.37
	280 × 280 × 93			44.5	280 × 280 × 93	5.40
	280 × 280 × 103			46.7	280 × 280 × 103	5.65
	280 × 280 × 113			54.2	280 × 280 × 113	5.69
Fig. 3	192 × 192 × 81	2000	400	34.5	800 × 800 × 81	7.09
Fig. 4, Supplementary Fig. 5	280 × 280 × 49	2000	120	18.1	500 × 500 × 49	5.74
Fig. 5, Supplementary Fig. 16	304 × 304 × 49	2000	1 (transfer learning from a pre-trained model)	0.33	304 × 304 × 49	5.60
Supplementary Fig. 2	ER: 256 × 256 × 113	100	3 (transfer learning from a pre-trained model)	0.048	ER: 256 × 256 × 113	5.22
	Beads: 248 × 248 × 113			0.048	Beads: 248 × 248 × 113	5.12

Supplementary Figs. 13, 14	$248 \times 248 \times 49$	1000	85	6.37	$248 \times 248 \times 49$	5.03
Supplementary Fig. 20	$280 \times 280 \times 113$	2000	55 (transfer learning from a pre-trained model)	18.1	$280 \times 280 \times 113$	5.69
Supplementary Fig. 22	$280 \times 280 \times 113$	6000	75	66.2 (large model)	$280 \times 280 \times 113$	33.5 (large model)
Supplementary Fig. 25	$280 \times 280 \times 113$	2000	165	54.2	$280 \times 280 \times 113$	5.69
		4000		108.4		
		6000		162.6		
		8000		216.8		
		10000		271		

Supplementary Table 2. Imaging conditions of live-cell experiments

	Sample	Label	Excitation NA	Excitation λ (nm)	Exposure time (ms)	Illumination intensity (mW/mm^2)	Cycle time (sec)	Time points
Fig. 3 Supplementary Video 2	T cells in mouse inguinal lymph node	Red-expressing OT-II T cells	0.5	561	180	0.62	30	76
Fig. 4 Supplementary Video 3	Neuronal signal in mouse cortex	GCaMP6f	0.5	488	160	0.19	2.25	500
Fig. 5 Supplementary Video 4	Neutrophils and blood vessels through intact mouse skull	PE-Ly6G Cy5.5	0.5	561, 640	160	561:1.02 640:0.21	60	633
Supplementary Figs. M, N	Neuronal structures in mouse brain slice	Thy1-YFP	0.5	488	100	1.45	0.9	1

Captions for Supplementary Videos

Supplementary Video 1	The principle of LEAO enables it to correct not only inter-angle disparities but also intra-angle distortions based on wave-optics modeling, whereas DAO is limited to correcting only the former under a ray-optics framework.
Supplementary Video 2	LEAO enables high-fidelity recording and large-scale tracking of ~ 5000 T cells across an entire mouse lymph node.
Supplementary Video 3	LEAO enables high-fidelity mesoscale recording of multiregional neural activity in mouse cortex after correcting spatially non-uniform aberration.
Supplementary Video 4	LEAO effectively combats severe aberration induced by the thick skull and polymer gel in TIS imaging, enabling continuous observation of neutrophil inflammatory response and repair process for over 10 hours after TBI in mouse intact skull.

Supplementary References

1. Lu, Z. *et al.* Phase-space deconvolution for light field microscopy. *Opt Express* **27**, 18131–18145 (2019).

2. Jin, M., Roth, S. & Favaro, P. Normalized Blind Deconvolution. In *Computer Vision – ECCV 2018* (eds Ferrari, V., Hebert, M., Sminchisescu, C. & Weiss, Y.) vol. 11211 694–711 (Springer International Publishing, Cham, 2018).

nature portfolio

Peer Review File

High-fidelity intravital imaging of biological dynamics via latent-space-enhanced digital adaptive optics

Corresponding Author: Professor Qionghai Dai

Parts of this Peer Review File have been redacted as indicated as we could not obtain permission to publish the reports from one of the peer reviewers.

This file contains all reviewer reports in order by version, followed by all author rebuttals in order by version.

Version 0:

Reviewer comments:

Reviewer #1

(Remarks to the Author)
In the manuscript, Yunmin Zeng et al present a new learning-based method called Latent-space-enhanced Digital Adaptive Optics (LEAO) for light-field imaging of biological structures and dynamics. LEAO addresses the challenge of optical aberrations caused by heterogeneous refractive indices in tissues, which degrade imaging performance and hinder downstream analyses. The method integrates wave optics modeling with deep learning to provide a robust solution for estimating and correcting large aberrations, which is supposed to have advancements over existing approaches, especially in challenging conditions such as low signal-to-noise ratios (SNR) and varying aberration magnitudes. The authors demonstrate their method via simulations and experiments, including large-scale tracking of T cells in lymph nodes, multiregional neural activity recording in the mouse cortex, and long-term monitoring of neutrophil responses after traumatic brain injury (TBI).
In general, the methodology itself represents a scalable and versatile framework to me, and it is interesting to see that the use of such a latent-space approach allows for the disentanglement of structural and aberration information, leading to improved accuracy and reliability in imaging.

Major comments:
(1) Clarification of technical details.
a) The wave-optics model and physical priors constitute a key part of the method, but it is unclear how these are exactly implemented, as the authors only provide a conceptual description. The authors should specify more details, e.g, the PSF and forward imaging model, so readers can understand the underlying mechanics of the proposed method.
b) The authors demonstrate the method on five different systems. How are the systems set, and what samples are used? What kind of aberrations are used in Fig. 2n? A more detailed explanation should be provided.
c) How is ground truth obtained?

(2) Consolidation of the performance over existing methods.
a) The authors mostly benchmark LEAO against DAO, which works under the simplified ray optics approximations while only showing one experiment against wDAO (S. Fig. 12), which is also based on wave optics. However, the evidence in S. Fig. 12, as I see, is not sufficient because the performance of LEAO over wDAO seems more marginal in this figure. I would suggest that the authors perform a more thorough performance analysis against wDAO.
b) In S Video 2, the structures in the LEAO images (13 s, right part) have an astigmatism shape? Are these structures true? Or are there residual aberrations? Could the authors comment on it?

Minor comments:
(3) What Zernike convention does the authors use? Please specify.
(4) Line 51, refs 11 & 12 are senorless AO but not based on wavefront sensor.
(5) Line 94, please spell out the full name of TBI at first use.

(Remarks on code availability)

Reviewer #2

(Remarks to the Author)
Summary & Novelty
The authors introduce LEAO, a latent-space-enhanced digital adaptive optics method for light-field microscopy (LFM) that explicitly separates sample structure from aberration wavefront information in the latent space of an autoencoder. Key innovations include:
1. Latent-space factorization — Encoder features are split into structure and aberration halves.
2. Customized latent loss — A triplet-style loss enforces invariance of each latent to changes in the other factor.
3. Dedicated aberration estimator — The aberration latent feeds a regression head predicting Zernike coefficients for PSF generation.
4. Physics-based training — Synthetic triplets generated with a wave-optics PSF model provide ground-truth supervision for aberration estimation.
This integration of disentangled representation learning with physics-based modeling is novel within computational adaptive optics.

LEAO is validated across diverse scenarios: in vivo mouse cortex two-photon calcium imaging, fixed T-cell imaging, and synthetic 3D bead/biological phantoms. Results consistently show improved resolution and contrast over uncorrected reconstructions and competing computational AO methods (DAO, CoCoA). The method demonstrates robustness across sample types and aberration strengths, with reconstructions that recover fine structural details otherwise lost in uncorrected data.

Limitations
1. Dependence on generalization of the estimator
The method operates in an open-loop fashion: the estimated aberration is used once to generate a PSF for reconstruction, but there is no closed-loop correction mechanism. Reconstruction errors due to misestimation do not feed back into improving the aberration estimate. This makes robustness heavily dependent on the trained estimator's generalization to unseen experimental conditions.
2. Simulation-to-real gap
While the authors describe their physical modeling as "anchoring" the features to diffraction physics, prior work has shown that reconstruction artifacts can still emerge from simulation–experiment mismatches. LEAO inherits this vulnerability because its training relies entirely on synthetic triplets, and the manuscript does not deeply address the sim-to-real gap or mitigation strategies (e.g., domain adaptation, fine-tuning with real data).
3. No explicit benchmark against closed-loop hardware AO comparison
• The method is benchmarked against other computational AO approaches (one from this group, another from a different group). However, it does not have a direct comparison with physical AO result, and thus it is unclear whether the CAO result is comparable to physical AO results.
4. Disentanglement assurance
• The success of latent factorization depends on the independence of structure and aberration variations in the training triplets. While this is controlled in simulation, real samples may exhibit correlations (e.g., structure-dependent scattering) that could challenge the separation. The manuscript does not discuss measures of disentanglement quality in real experimental data.

(Remarks on code availability)

Reviewer #3

(Remarks to the Author)
The paper presented a deep-learning based image processing method and the method was demonstrated on large volumetric long-duration data collected in diverse biological applications including tracking T cells across a mouse lymph node and imaging through intact skull of mice to compensate aberrations digitally. The neural network method involves latent space training, which is intuitive. However, the technique has its drawbacks and limitations, especially with its versatility when the training is limited to the selected sample structures and some level of retraining is needed when change to a different sample structure.

I have following questions that would like clarification from the authors.

1. For long duration animal imaging, I would assume sample motion as a typical issue. Does random sample motion cause issues to the technique? How it was tackled?

2. In both figure 4 and 5, authors included images of w/o AO, which still have excellent signal to background / signal to noise ratio, only with distorted PSFs. I would think those images can be processed using some deconvolution-based methods. I would like to see authors comment on the deconvolution-based methods and how LEAO is different and stands out.

3. LEAO was trained and limited to wavefronts consisting 17 Zernike modes, which only allow the system to process rather smooth aberrations. However, one would imagine scattering as a dominant factor especially for applications such as imaging through an intact skull. Can LEAO deal with data when wavefront distortions containing higher order uncorrectable modes?

4. In figure 3 e, close to the right end, the features look sharper and brighter with better signal without AO when comparing to LEAO. The processed LEAO no longer captures the strctures which could be seen originally in the w/o AO. Does this suggest some limitations of LEAO when it can actually make image looks worse? How this affect the data integrity of the LEAO processed images?

5. In Figure 1 f and 4c, the wavefront generated by DAO seems to have the same shape to the ground truth wavefront, but only off by amplitudes (in a consistent way). Is this discrepancy due to any fundamental limitation of DAO or it is more to do with how it was set up and operated? As the latter reason can affect the fairness of the comparison.

6. I do not fully understand Figure 4 when a 4.6 mm x3.4 mm x0.6 mm volumetric imaging is processed on 3x5 spatial tiles. Does this mean that for each spatial tiles, it is much wider in x direction but much narrower in y direction? Does this also mean that the isoplanatic patch is in mm level? Does it also mean that there is no change of aberration throughout the 600 um imaging depth? This sounds a bit too large to me especially this demonstration imaged dynamic activations in mouse cortex and green fluorescence was used. Do the authors think the aberrations were mainly sample-induced or optical system-induced? In 4c, it seems to suggest that the wavefront aberration is huge, with a peak to valley amplitude of 9 wavelengths. The fluorescence intensity, on the other hand, still seems to be descent despite the large aberration. I would like to see the authors comments on this.

7. In the method section, the authors suggested that a total of 17 Zernike modes were involved and a total of 2000 dataset were used for training. If we say each Zernike modes can be either positive and negative, the total combinations of these 17 Zernike modes are 217. 2000 dataset sounds way too small to me. I would like the authors comments on this.

(Remarks on code availability)
The programme seems to be documented with clear instructions on how to install packages and run training. Examples were also provided. However, as the training requires GPUs, I was unable to test the programme.

Author Rebuttal letter:

Response to Reviewers
We are grateful for the reviewers' insightful comments and suggestions, which have substantially improved our manuscript. We believe we have addressed all of the major and minor comments. The revised and added texts have been highlighted in red in the manuscript and supplementary materials. Please find below a point-by-point response to each comment.

Reviewer #1
Remarks to the Author:
In the manuscript, Yunmin Zeng et al present a new learning-based method called Latent-space-enhanced Digital Adaptive Optics (LEAO) for light-field imaging of biological structures and dynamics. LEAO addresses the challenge of optical aberrations caused by heterogeneous refractive indices in tissues, which degrade imaging performance and hinder downstream analyses. The method integrates wave optics modeling with deep learning to provide a robust solution for estimating and correcting large aberrations, which is supposed to have advancements over existing approaches, especially in challenging conditions such as low signal-to-noise ratios (SNR) and varying aberration magnitudes. The authors demonstrate their method via simulations and experiments, including large-scale tracking of T cells in lymph nodes, multiregional neural activity recording in the mouse cortex, and long-term monitoring of neutrophil responses after traumatic brain injury (TBI).
In general, the methodology itself represents a scalable and versatile framework to me, and it is interesting to see that the use of such a latent-space approach allows for the disentanglement of structural and aberration information, leading to improved accuracy and reliability in imaging.
Response: We are grateful for the reviewer's positive comments on our work and the precise summary of our advantages. The key to our innovations lies in the design of a wave-optics-based latent space that explicitly disentangles the aberration and structure representations, leading to aberration estimation with higher accuracy and robustness. LEAO demonstrates advantages in challenging conditions such as large aberration, low signal-to-noise ratios and large field of view.
With the help of the reviewer's advice, we explained how our mechanism makes

use of the wave-optics priors by describing the formation of aberrated images from a wave-optics perspective. Namely, an aberration could be represented as a phase modulation in the back pupil plane, which modulates the Fourier space of the system PSF and leads to distorted profile and aberrated samples. We exploited the correlation between aberration and the aberrated image by extracting features in their spatial-angular measurements. As instructed by the reviewer, we added more detailed technical clarifications in the text, legends of figures, and Methods about the specification of the system setup, the acquirement of ground truth, and so on. We believe these details would resolve the concerns regarding the specific implementations of our LEAO and stress out the theoretical foundation of the proposed method.
The reviewer also suggested that we conduct a more thorough experiment about the comparison of our method against existing wave-optics method like wDAO, which we have addressed by adding experiments on data with larger sample aberrations. LEAO holds significant superiority over wDAO both visually and statistically on such cases, because wDAO degenerates into DAO when dealing with dynamic sample aberrations.
At last, we have further improved the lymph node experiment in Fig. 3 with a denser tiling scheme to alleviate the residual astigmatism the reviewer mentioned. Previously, for time-efficient computation, we neglected the strong spatial nonuniformity of the aberrations in this sample, resulting in degraded performance in some spatial regions. By increasing the tiling number of LEAO, the reconstruction performance is improved.
We believe the revisions based on the reviewer's constructive comments have brought substantial improvement to our work.

Major comments:
(1) Clarification of technical details.
a) The wave-optics model and physical priors constitute a key part of the method, but it is unclear how these are exactly implemented, as the authors only provide a conceptual description. The authors should specify more details, e.g, the PSF and forward imaging model, so readers can understand the underlying mechanics of the proposed method.
Response: We thank the reviewer for this constructive advice. We have added a diagram (Fig. R1) to demonstrate how aberrated PSF is generated through the forward imaging model, and how arbitrary biological sample undergoes the forward imaging model to form aberrated spatial-angular measurements. When simulating data based on this forward imaging model, the wave-optics aberration information flows into the training data, and then is utilized by LEAO. Specifically, LEAO takes the wave-optics aberrated data as the input, and Zernike coefficients of the aberration wavefront as the supervised learning target, to form a latent space in which wave-optics aberration information is distilled and exploited to give a high accuracy aberration estimation.
In the meantime, we have provided a mathematical description of this process.
Without aberration, light from a point source ($pp1$, $pp2$, $pp3$) forms the light field below at the image plane:

$$UUiiiiiiiii\,(xx, pp3) = \frac{MMssssss^2}{ffooooooo^2}\,eeeeee^{-ii\cdot pp}\int_0^{\alpha\alpha} 4\pi\pi pp3\;ssssss2\,(\theta\theta/2)\;2\pi\pi\;ssssss(\theta\theta)\;\sqrt{cccccc\;\theta\theta}\;eexxxx^{-ii}\;JJ0\left(\frac{2\pi\pi}{\lambda\lambda}(xx1-pp1)2+(xx2-pp2)2\right)ssssss(\theta\theta)\,dddd, \quad (1)$$

where $xx = (xx1 , xx2)$ is the position on the image plane, $MMssssss$ is the magnification rate of the optical system, $ffooooooo$ is the focal length of the objective lens, $\lambda\lambda$ is the emission wavelength, $JJ0\,(\cdot)$ is the 0th order Bessel function of the first kind, $\alpha\alpha$ is the half-angle of the numerical aperture, and $\theta\theta$ is the angle between the light ray and the optical axis. To take the effect of aberration $\phi\phi$ into consideration, we need to apply it to the phase of the Fourier transformation of $UUiiiiiiiii$, for this is equivalent to applying a continuous wavefront distortion at the pupil plane:

$$UUaaaaaaaaaaaaaaaaaa = \mathcal{F}^{-1}\left\{\mathcal{F}(UUiiiiiiiii)\,ee^{iiii}\right\}, \quad (2)$$

where $\mathcal{F}^{-1}$ and $\mathcal{F}$ are reverse Fourier transform and Fourier transform. After that, following the configuration of a typical light-field system, the light will go through a microlens array $tt(xx)$ and propagate to the detector plane:

$$UUddddddddddddddddd\,(xx', pp3) = \frac{2\pi\pi\pi\pi}{ee^{ii}\,\lambda\lambda\,ffiiiiiiiiiiii^{2}}\int UUaaaaaaaaaaaaaaaaaa\,(xx, pp3)\cdot tt(xx)\cdot eeeeee^{\frac{jj}{2\pi\pi\pi\pi\,\lambda\lambda ff}\|xx'-xx\|22}\,dddd, \quad (3)$$

where xx' is the position on the detector plane, n is the refractive index, and $ffμμμμμμμμμμμμ$ is the focal length of the microlens array. Each pixel xx' has a relative lateral shift $uu0$ with respect to one of the microlens array with a center position $xx0$. Thus, the aberrated PSF can be formed as:

$$PPPPPP(xx0, pp3, uu0) = \iint UUddddddddddddddddd(xx', pp3)rrrrrrrr \iiint ddxx', \quad (4)$$

where $ddss$ is the sensor pixel size and rect() is the rectangle function.

Fig. R1 (Supplementary Fig. 23) | Diagram of wave-optics forward imaging model for LEAO. a, b, Forward imaging of a point source (a) and biological sample (b). The former is equivalent to the PSF generation. OBJ, objective lens. TL, tube lens. MLA, microlens array.

Aberrated LFM spatial-angular measurements were further obtained by

$$LLLLmm,nn(xx, uu) = \int VVnn(xx, zz) * PPPPPPmm(xx, zz, uu)dddd, 1 \le mm \le MM, 1 \le nn \le NN, \quad (5)$$

where $PPPPPPmm$ is the mth aberrated PSF, $VVnn$ is the nth 3D volume, and * is the two-dimensional convolution with respect to x. M = 200 for all our experiments except for Supplementary Fig. 22, in which a higher number of PSFs (M = 600) is needed to train a model capable of processing higher order aberrations. N depends on the accessible data amount, typically in the range of 60 to 200. The wave-optics aberration information is encoded in the spatial-angular measurements, waiting to be extracted by LEAO.

We have added the above detailed description of the generation of aberrated PSF, and how the PSF is applied in the imaging process in Simulation of aberrated spatial-angular measurements in the Methods section. We believe in this way the readers can understand how the aberration phase affects the wavefront of the light beam and the importance of building the algorithm on a wave-optics basis.

b) The authors demonstrate the method on five different systems. How are the systems set, and what samples are used? What kind of aberrations are used in Fig. 2n? A more detailed explanation should be provided.

Response: We thank the reviewer for this advice. We added a list of all key parameters for five different optical systems in Experimental Setup in the Methods section. The LFM has a 1.05 NA objective with refractive index of 1.33, a microlens array of 136.5 μm pitch, 2800 μm focal length, 21×21 angular resolution, and a system magnification rate of 43.067. The configuration of sLFM is the same as that of LFM except for adding a 3×3 scanning scheme. The configuration of csLFM is the same as that of sLFM except for adding a line-confocal illumination with a slit size of 11-times Airy units of the whole-objective numerical aperture to reject background fluorescence. The RUSH3D has a 0.5 NA objective with refractive index of 1, a microlens array of 69 μm pitch, 393.3 μm focal length, an angular resolution of 15×15 with scanning of 3×3, and a system magnification rate of 5.761. The 2pSAM has a 1.05 NA objective with refractive index of 1.33, a pinhole size of 50 μm ($\alpha\alpha$=0.1), an angular resolution of 13, and a system magnification rate of 18.

The samples used for Fig. 2m, n are simulated neurons generated by an open-source package named Neural Anatomy and Optical Microscopy, or NAOMi (Song, A. et al. J. Neurosci. Methods 358, 109173, 2021), which we have added in the corresponding figure legend. As for the aberrations used, they follow the same simulation rules we adopted throughout the paper (Methods). Briefly, Zernike coefficients up to five orders (17 modes, discarding piston, tip, tilt and defocus) are randomly generated to form random aberration wavefronts used for training or testing, respectively.

c) How is ground truth obtained?

Response: Ground truth aberration wavefronts were generated by randomly sampling Zernike coefficients up to five orders. For the experiments on real data (Supplementary Figs. 13, 14), the randomly generated ground truth aberration wavefronts were introduced to the optical system by inserting phase masks at the pupil plane. Ground truth volumes were reconstructed from aberration-free samples captured by the system without any phase masks. For other simulation experiments, the source of ground truth structures was stated in Data Availability. Briefly, ground truth structures are either artificially generated (neurons, by NAOMi) or downloaded from a website offering high-resolution three-dimensional volumes (https://www.allencell.org/data-downloading.html#DownloadImageData). We have added these descriptions in the revised manuscript.

(2) Consolidation of the performance over existing methods.
a) The authors mostly benchmark LEAO against DAO, which works under the simplified ray optics approximations while only showing one experiment against wDAO (S. Fig. 12), which is also based on wave optics. However, the evidence in S. Fig. 12, as I see, is not sufficient because the performance of LEAO over wDAO seems more marginal in this figure. I would suggest that the authors perform a more thorough performance analysis against wDAO.
Response: We thank the reviewer for this insightful advice. In the original Supplementary Fig. 12, we put emphasis on the complexity difference and accessibility of wDAO and LEAO. wDAO requires specially designed samples like fluorescent beads or calibration charts for the iterative calibration of system aberration, and then proceeds to use ray-optics-based DAO when processing sample aberration. Wave-optics property is manifested in the iterative process of generating the system PSF, but it cannot be used to correct the sample aberrations caused by any biological samples. LEAO puts no limits on the type of samples and is fast to produce a hybrid estimation of both the system and sample aberration. Therefore, as the sample-induced aberration increases, LEAO can exhibit performance that is markedly superior to wDAO, which has not been clearly demonstrated previously. Thanks to your advice, we extended the sample aberration from 2 $\lambda\lambda$ to 5 $\lambda\lambda$ (Fig. R2 (Supplementary Fig. 21 in the revised manuscript)). The accuracy of wDAO underwent a sharper decrease than LEAO, and the corresponding reconstruction images became significantly blurrier and more distorted with increasing sample aberration, showing that wDAO's performance degrades more when processing large sample aberration as it deals mainly with system aberration and reduces to ray-optics-based correction when facing sample aberration. This advantage is quite important since sample aberration gets significantly larger during in vivo imaging of deep tissue.
Fig. R2 (Supplementary Fig. 21) | Comparison of LEAO with wDAO. a, b, Workflows of wDAO (a) and LEAO (b). wDAO requires a specific, well-defined calibration object, typically a calibration chart or fluorescent beads, to iteratively perform calibration of the system aberration. Complex biological samples do not provide sufficiently clear features, so wDAO cannot converge reliably. When processing real biological samples that exhibit additional sample-specific aberrations, DAO will replace wDAO for aberration estimation, as it is more practical and avoids long-time recalibration for each new sample. In contrast, LEAO can simultaneously estimate both system and sample aberration on any samples with unknown aberration profiles. c, Illustration of total aberrations including system aberration (fixed) and increasing sample aberrations. d, Computation time of system aberration estimation by wDAO and total aberration estimation by LEAO. LEAO possesses a speed advantage of 5 orders of magnitude. e, Normalized residual aberration $\sigma\sigma$ and SSIM obtained by wDAO and LEAO. f, MIP of ground truth. g, h, Corresponding LEAO and wDAO results for different sample aberration levels. Aberration wavefronts estimated by wDAO and LEAO are shown in the insets. Scale bar, 20 μm, 7 μm (zoom-in regions).
b) In S Video 2, the structures in the LEAO images (13s, right part) have an astigmatism shape? Are these structures true? Or are there residual aberrations? Could the authors comment on it?
Response: We are grateful for the reviewer to point out this problem. Based on the visual performance we can deduce that there are residual aberrations especially astigmatism in the right part since we have prior knowledge of the morphology of T cells. This is because the peripheral regions have larger aberration and the effect of such aberrations could be more obvious when presented by three-dimensional rendering software. To address the distortion, we increased the field-of-view partitioning to 10×7 patches, as the earlier 2×2 scheme was likely too coarse, causing each patch to span a large region where the aberration is spatially non-uniform. After re-doing relevant statistics and figures, we found out that the performance of LEAO improved (Fig. R3). In the new Figure, LEAO still brought our clearer contours and restored more information than DAO, as shown in Fig. R3c, d.

Fig. R3 (Fig. 3) | LEAO enables high-resolution imaging of ~5000 T cells across an entire mouse lymph node. a, MIP of T cells in a 4 × 3 mm2 mouse lymph node with LEAO, with DAO and without AO. b, Estimated aberration wavefronts by LEAO and DAO. The whole FOV was divided into 10 × 7 tiles. c, d, e, Enlarged images of the areas marked by white dashed box in a. f, Intensity profiles along the lines marked by white arrow in e. LEAO can

separate adjacent T cells distorted by aberration with higher peak values, while DAO and w/o AO reconstructions cannot. g, Directional MIPs of the area marked by yellow dashed box in a. h, Color-coded temporal tracks of T cells across a duration of 38 minutes estimated from results with LEAO, with DAO and without AO. i, A representative trajectory of a single cell from LEAO, overlaid on the timelapse MIPs. The region is marked by white dashed box in h. j, Identified trajectory number obtained by the methods with LEAO, with DAO and without AO. k, l, Histogram of track mean velocity (k) and track length (l) obtained by LEAO. Scale bar, 140 μm (a, h), 70 μm (c, d, g, i), 20 μm (e).

We then proceed to test the visual performance from a three-dimensional perspective. When rendered by Imaris, the astigmatism shape in the right part becomes less significant with our new tiling scheme (Fig. R4).

Fig. R4 | Three-dimensional rendering image of 10×7 tiled LEAO (new) and 2×2 tiled LEAO (old). The astigmatism shape becomes less significant with a denser tiling scheme. Scale bar, 140 μm, 70 μm (zoom-in region).

Minor comments:

(1) What Zernike convention does the authors use? Please specify.

Response: We thank the reviewer for this advice. We used a custom Zernike convention before. Now for better readability we have added statements in Methods and relevant figure legends that we used the American National Standards Institute (ANSI) convention, gave the formulas for sequencing index and Zernike polynomials, and modified all relevant figures to accommodate the new convention. Below is the list of Zernike polynomials we used in the revised manuscript.

Fig. R5 (Supplementary Fig. 24) | Zernike convention used in LEAO. The sign, sequencing order and relative magnitude of the used Zernike polynomials are listed.

(2) Line 51, refs 11 & 12 are sensorless AO but not based on wavefront sensor.

Response: We thank the reviewer for the comment. We apologize for the mistakes in our descriptions. We have corrected it to “without a wavefront sensor” now.

(3) Line 94, please spell out the full name of TBI at first use.

Response: Thank you for the notice. We have clarified the full name of TBI at first use. We have checked other abbreviations as well and modified them if they are not complete at first use.

Reviewer #2

Remarks to the Author:

Summary & Novelty

The authors introduce LEAO, a latent-space-enhanced digital adaptive optics method for light-field microscopy (LFM) that explicitly separates sample structure from aberration wavefront information in the latent space of an autoencoder. Key innovations include:

1. Latent-space factorization — Encoder features are split into structure and aberration halves.
2. Customized latent loss — A triplet-style loss enforces invariance of each latent to changes in the other factor.
3. Dedicated aberration estimator — The aberration latent feeds a regression head predicting Zernike coefficients for PSF generation.
4. Physics-based training — Synthetic triplets generated with a wave-optics PSF model provide ground truth supervision for aberration estimation.

This integration of disentangled representation learning with physics-based modeling is novel within computational adaptive optics.

LEAO is validated across diverse scenarios: in vivo mouse cortex two-photon calcium imaging, fixed T-cell imaging, and synthetic 3D bead/biological phantoms. Results consistently show improved resolution and contrast over uncorrected reconstructions

and competing computational AO methods (DAO, CoCoA). The method demonstrates robustness across sample types and aberration strengths, with reconstructions that recover fine structural details otherwise lost in uncorrected data.
Response: We thank the reviewer for the concise and accurate summary of our innovations in methodology, and for acknowledging our efforts in simulated and experimental validations. The three key performance gains of LEAO lie in accuracy robustness, and processing speed, like the reviewer said “The method demonstrates robustness across sample types and aberration strengths, with reconstructions that recover fine structural details otherwise lost in uncorrected data”.
We believe the reviewer is most concerned about the performance (generalization, fidelity, disentanglement assurance) of LEAO under experimental conditions. We agree with the reviewer on the importance of this aspect and summarize our efforts to address all these issues as below:
Firstly, the reviewer pointed out that there is no closed-loop mechanism to feed the reconstruction error back into the network. We admit this limitation and explained the reason why LEAO cannot be modified as a closed-loop method in the response below. We would like to clarify that it is not our initial intention to make LEAO an iterative closed-loop method. On the contrary, we wanted it to be a fast framework that has little dependence on the sample type. Although being an open-loop method, LEAO outperforms computational closed-loop algorithm in accuracy, noise resilience, and time consumption, as comprehensively validated in the revised manuscript.
Nevertheless, we agree with the reviewer that our robustness is “dependent on the trained estimator’s generalization to unseen experimental conditions”. To further prove the estimator’s generalization ability, we demonstrated two experiments centering the transferring to a new sample type and to a new system setup. The accuracy of LEAO could be maintained with a fast fine-tuning process on small dataset of less than 50 stacks. Even without any fine-tuning, the performance on the completely new conditions still surpasses DAO, a closed-loop algorithm.
Secondly, we have demonstrated LEAO’s improved performance in various in vivo experiments, but without an explicit ground truth, because it is impossible to obtain in real biological imaging. The reviewer noticed this issue and questioned about the sim-to-real gap and comparison with a hardware-based compensation. To address these points, we built a new light-field microscopy system, in which custom-made phase masks corresponding to certain aberration phases could be optionally inserted, providing aberrations with known ground truth. By doing so, we can directly compare LEAO and aberration-free reconstruction by removing the inserted phase mask, providing strong evidence on our performance in real scenario. We also simulated a typical closed-loop hardware AO setup, wide-field imaging with a deformable mirror (DM), to perform comparison. Even with high-precision wavefront sensing technique, the accuracy of hardware AO is still limited by the insufficient actuator number of correction device, while LEAO theoretically has better correction precision with its wave-optics design.
Thirdly, we analyzed the disentanglement on real experimental data. We captured 4 different regions of a brain slice, each with 2 different phase masks, using the system described above. t-SNE analysis on these data validated the disentanglement quality of LEAO on real data.
We believe the revised version of our manuscript presented more convincing evidence on LEAO’s experimental performance advantage, and clearly stated the limitations as well.

Limitations
1. Dependence on generalization of the estimator
The method operates in an open-loop fashion: the estimated aberration is used once to generate a PSF for reconstruction, but there is no closed-loop correction mechanism. Reconstruction errors due to misestimation do not feed back into improving the aberration estimate. This makes robustness heavily dependent on the trained estimator’s generalization to unseen experimental conditions.
Response: We thank the reviewer for commenting and advising on generalization problem. After careful consideration, we have to admit that a closed-loop mechanism is intrinsically not available in LEAO. If we have a reconstruction with residual errors, and then simulate a forward imaging process on said reconstruction to feed it back to the network, the network cannot correctly identify the residual aberration. Although residual aberration introduces structural distortion in the feedback that can assist aberration identification, the angular distribution (e.g., disparities across angular observations) is still identical to that of aberration-free data, as the forward imaging step on reconstructed volumes can only employ an ideal aberration-free PSF. This would confuse the network, leading to unreliable results. If LEAO is purely dependent on sample structures, closed-loop scheme would be possible. However, a brute-force mapping from sample structures to estimated aberrations is not what we intended to do.

On the contrary, we tried our best to minimize the effect of different sample structures on aberration estimation by designing a latent-space-enhanced scheme to disentangle aberration and structure. Meanwhile, we developed LEAO to be a fast, physical-based method that can produce robust and high-fidelity aberration estimations in one go on new samples after thorough training, as opposed to closed-loop methods that are time-consuming. Actually, LEAO outperforms computational iterative closed-loop methods such as DAO and wDAO in many ways. For example, LEAO exhibits stronger robustness to multiple experimental conditions such as noise, aberration magnitude, angle number and sampling rate (Fig. 2). The time cost of LEAO is also orders of magnitude lower (Supplementary Fig. 21 in the revised manuscript). Our response to question 3 also demonstrates LEAO's advantages compared with closed-loop hardware AO in terms of wave-optics correction and spatially varying aberration.

Still, inspired by the reviewer's concern for LEAO's generalization ability to unseen experimental conditions, we dug deeper into the generalization problem. We agree that the robustness of LEAO is "dependent on the trained estimator's generalization to unseen experimental conditions", so we comprehensively tested the generalization ability of the estimator. After careful consideration, we categorized "unseen experimental conditions" into two aspects: unseen samples and unseen systems. For unseen samples, e.g., model was trained on bead-like structures but is to be applied to line-like structures. To demonstrate this, we directly applied the LEAO model trained on the neuron dataset to the membrane dataset and found that its performance was already superior to DAO. However, there was still a residual aberration of approximately 0.07 σ. A short fine-tuning process of less than five minutes on a small dataset (at most 50 data stacks) further reduced the residual aberration to around 0.05 σ, achieving performance comparable to an LEAO model fully trained on the membrane dataset (at ~ 2,000 data stacks) (Fig. R6 (Supplementary Fig. 17 in the revised manuscript)).

Fig. R6 (Supplementary Fig. 17) | Rapid transfer learning of LEAO to a new sample type with a small training dataset. a, Convergence curves of normalized residual aberration $\sigma\sigma$ versus the number of iterations on a membrane test dataset. The iterations are presented on a logarithmic scale, with values of 10, 100 and 500 marked by arrows. The model trained on membrane dataset (grey line) took ~1333.3 minutes to converge, while the model first trained on simulated neuron dataset and then finetuned on membrane data (red line) converged in ~4.5 minutes. b, Boxplots showing SSIM and normalized residual aberration $\sigma\sigma$ obtained by different LEAO models and DAO (n = 10). Boxplot format: center line, medians; limits, 75% and 25%; whiskers, the larger value between the largest data point and the 75th percentiles plus 1.5× the interquartile range (IQR), and the smaller value between the smallest data point and the 25th percentiles minus 1.5× the IQR; outliers, data points larger than the upper whisker or smaller than the lower whisker. The number of membrane data used for training is also plotted on the right, showing the LEAO model using transfer learning achieved performance comparable to that from training-from-scratch while using only 2.5% of the membrane data. c-h, The representative MIPs for the ground truth (c), the results without AO (d), the results with DAO (e), the results with different LEAO models (f-h). Ground truth and estimated aberration wavefronts are shown in the insets. Scale bar, 40 μm, 10 μm (zoom-in regions).

For unseen systems, we added a new experiment simulating this condition (Fig. R7 (Supplementary Fig. 18 in the revised manuscript)). Two distinct systems with different optical parameters are simulated, marked as system A and B. System A has a magnification rate of 43.067, numerical aperture of 1.05, microlens pitch size of 136.5 μm, microlens focal length of 2800 μm, refractive index of 1.33, and 21×21 pixels behind each microlens. System B is used as the test model and has a magnification rate of 20, numerical aperture of 0.5, microlens pitch size of 100 μm, microlens focal length of 2100 μm, refractive index of 1.0, and 13×13 pixels behind each microlens. We want to explore the generalization performance from system A to B. Firstly, a model was trained and evaluated on data acquired by system B to benchmark the LEAO performance. Then, a model trained on dataset acquired from system A was tested using the same dataset acquired by system B. The aberration estimation accuracy decreased slightly. To further improve the performance, we fine-tuned this model with a small dataset containing 50 data stacks from system B for less than 5 minutes (Fig. R7a). This transfer learning process brought the performance to the same level as that fully trained on data from system B, but with much smaller dataset generation cost and 400 times less time (Fig. R7b, c). The reconstruction results also validated that the performance

of the fine-tuned model is equal to that trained from scratch (Fig. R7d-i). Fine-tuned model and normally-trained model can both restore the intricate details resembling that of ground truth when converged, but the former could converge much more quickly (Fig. R7d, h, i). It should also be noted that even without transfer learning, the performance of LEAO is comparable or even better than DAO (Fig. R7f, g).

Fig. R7 (Supplementary Fig. 18) | Rapid transfer learning of LEAO to a new system with a small training dataset. a, Schematic of the experiment. Two distinct systems are used. The transfer learning of system A to system B was studied. All evaluations were conducted on data acquired from system B. b, Normalized residual aberration curve on test dataset by one model trained on system B and one model trained on system A then transferred to system B. The transfer learning was 400 times faster even with a conservative estimate that considers the transfer learning process to be converged at iteration 500. If we consider the transfer learning to be converged at iteration 50, which is reasonable given that the test loss at iteration 50 is similar to that at iteration 500, the process would even be 4000 times faster. c, Evaluation of SSIM and normalized residual aberration $\sigma\sigma$ on test dataset by one model trained on system B, one model with transfer learning on system B from a model trained on system A, one model trained on system A, and DAO (n = 10). Dataset number used by the model trained on system B and the model with transfer learning on system B are also shown on the right, showing that the transfer learning needs much fewer training data stacks compared to training from scratch. d-i, MIPs of ground truth (d), without AO (e), DAO (f), model trained on system A (g), model trained directly on system B (h), and model with transfer learning on system B from a model trained on system A (i). In h and i, results from key iterations are shown. The corresponding iterations are marked by black arrow in b. Ground truth(d) and estimated aberration wavefronts (e-i) are shown on the left bottom. Enlarged images of the region marked by white box are shown on the right bottom. Scale bar, 20 μm, 8 μm (zoom-in regions).

In summary, the accuracy of LEAO outperforms DAO when directly generalized to unseen conditions for both unseen samples and systems, and could be further improved with only a small amount of training dataset and less than 5 minutes time consumption. We have added corresponding results and discussion in the revised manuscript.

2. Simulation-to-real gap

While the authors describe their physical modeling as “anchoring” the features to diffraction physics, prior work has shown that reconstruction artifacts can still emerge from simulation–experiment mismatches. LEAO inherits this vulnerability because its training relies entirely on synthetic triplets, and the manuscript does not deeply address the sim-to-real gap or mitigation strategies (e.g., domain adaptation, fine-tuning with real data).

Response: We thank the reviewer for raising this concern. It is true that LEAO relies entirely on synthetic triplets, which is also the advantage of our method, because it does not require obtaining real training dataset that is very costly. For example, obtaining real training dataset needs to utilize spatial light modulator or other wavefront shaping devices to artificially introduce hundreds of known aberration wavefronts and capture their corresponding data stacks. For some sample types, e.g., highly dynamic samples, it is impossible even if we have the time and budget. For the same reason, sim-to-real mitigation strategies are not very practical because they would require certain amount of real dataset nonetheless.

However, we tried our best to make the simulations as close to experimental conditions as possible. Firstly, for each experiment in Figs. 3-5, we used 3D volumes of the same sample type as in the experiments to be the ground truth structures, and computationally introduced aberrations to generate the training dataset. Of course, we did not specifically conduct any imaging sessions only to obtain these sample volumes because it is easy to access such data in typical biological labs or open-source websites. So, many of the training data are actually semi-synthetic. Secondly, we addressed realistic problems such as noise, system setup, sampling rate (Fig. 2) to thoroughly investigate conditions that may occur in real experiments. From our experimental results (Figs. 3-5), it is validated that LEAO holds superior performance over other computational adaptive optics methods.

To further alleviate the reviewer’s concern, we conducted a new experiment to characterize LEAO’s performance on real data. In previous experiments, it is impossible to know the ground truth aberration of a deep tissue in vivo, so the reviewer might be doubtful of LEAO’s actual performance on real scenarios since it is synthetically trained. In our new experiment, however, we introduced known aberrations via inserted phase masks at the Fourier plane of the optical system, and imaged thin mouse brain slices labelled by Thy1-YFP which could be seen as without

additional sample aberration, as is shown in Fig. R8 (Supplementary Fig. 13 in the revised manuscript). Specifically, we designed two phase masks made of Corning 7980 glass, each producing a predefined and fully known aberration wavefront pattern. Ground truth structures were obtained by using data captured without phase mask. Aberration wavefronts estimated by LEAO closely resembled the patterns of phase masks, proving the fidelity of LEAO on real data. The image quality of LEAO was also comparable to that of ground truth structures.

Fig. R8 (Supplementary Fig. 13) | LEAO on thin brain slices with artificially induced aberrations. a-c, MIPs of ground truth (a), LEAO (b) and w/o AO (c). Zoom-in regions are shown on the right top of each image. Ground truth images were reconstructed from aberration-free samples captured without any induced aberrations. Ground truth or estimated aberration wavefronts are shown on the left bottom. d, Intensity profiles of the structures marked by yellow (profile 1) and white (profile 2) arrows in a. e, Intensity profiles of the structures marked by yellow (profile 1) and white (profile 2) arrows in b. f, Intensity profiles of the structures marked by yellow (profile 1) and white (profile 2) arrows in c. g-i, MIPs of ground truth (g), LEAO (h) and w/o AO (i), on another sample. j-l, Intensity profiles of corresponding images, on another sample. Scale bar, 50 μm, 5 μm (zoom-in regions in a-c), 9 μm (zoom-in regions in g-i).

3. No explicit benchmark against closed-loop hardware AO comparison
The method is benchmarked against other computational AO approaches (one from this group, another from a different group). However, it does not have a direct comparison with physical AO result, and thus it is unclear whether the CAO result is comparable to physical AO results.
Response: We thank the reviewer for the insightful suggestion. At first, we place our method not in the range to compare with physical AO, because its highlight is the ability to solve the spatially nonuniform aberrations across a large field during post processing, without adding complex optical components or prolonging the imaging session. Now that the reviewer has mentioned the issue, we realized that only comparing LEAO with computational AO methods on experimental data may not be convincing enough.
By answering question 2, we compared LEAO with the images obtained by removing the phase mask. Conceptually, removing the aberration source can be regarded as a hardware-based compensation and represents an almost ideal scenario, functionally analogous to programming a deformable mirror with a perfectly cancelling aberration wavefront, i.e., the theoretical upper limit of hardware AO performance. We believe the comparison of LEAO with this hardware AO provides strong evidence that LEAO is comparable to physical AO results.
However, hardware AO is not theoretically perfect and cannot fully compensate the aberrated wavefront. To further compare LEAO with a realistic hardware AO condition, we conducted a simulation using a typical closed-loop hardware AO setup for wide-field imaging with a deformable mirror (DM), as shown in Fig. R9. With a sufficiently bright guide star and well-designed looping strategy, the wavefront sensing precision of closed-loop hardware AO can be very high. However, the aberration compensation device could provide only ray-optics-based wavefront correction. Consequently, if the deformable mirror has an insufficient number of actuators, the aberration cannot be effectively compensated. For example, a typical deformable mirror with 10×10 actuators divides the estimated aberration wavefront into 10×10 tiles, within each tile an actuator can perform piston, tip and tilt to change the direction of incoming light. More finely divided deformable mirrors would require much higher price. Usually, deformable mirrors with over 1, 000 actuators are rare and expensive (e.g., over $ 300, 000). A spatial light modulator with finer wavefront divisions could serve as an alternative, but its slow switching speed makes it unsuitable for fast correction in closed-loop AO and is therefore not considered here. Specifically, we simulated the compensating aberration wavefronts of deformable mirrors with 10×10 and 50 × 50 actuators, respectively, and further performed deconvolution on the resulting images after closed-loop hardware AO (Fig. R9b, c, f, g). Simultaneously, aberration correction was also performed using LEAO. We found that the visual quality of images obtained by LEAO, hardware AO (with a 10×10 deformable mirror array, deconvolved), and hardware AO (with a 50×50 deformable mirror array, deconvolved) was similar. Quantitatively, the residual aberration of LEAO was comparable to that of hardware AO, and the PSNR was marginally higher than that of hardware AO (with a 10×10 deformable mirror array, deconvolved) but slightly lower than hardware AO

(with a 50×50 deformable mirror array, deconvolved). Therefore, after correction, LEAO showed comparable image quality to the deconvolution result of closed-loop hardware AO.

Fig. R9 (Supplementary Fig. 1) | Comparison of LEAO with closed-loop hardware adaptive optics. a-h, MIPs of the ground truth (a), wide-field results of hardware AO by 50×50 (b) and 10×10 (c) deformable mirror (DM) and raw aberrated image (d), LEAO result (e) and the deconvolved wide-field results of 50×50 (f), 10×10 (g) hardware AO and raw aberrated image (h). Reference ground truth aberration wavefront and aberration wavefronts estimated by each method are shown in the insets. Simulation details of hardware AO could be found in Methods. i, PSNR evaluation of the images in b-h. j, Normalized residual aberration $\sigma\sigma$ of the aberration wavefronts in b, c, e. Scale bar, 20 μm.

In addition, it should also be noted that hardware AO could not process spatially-varying aberrations, which can be achieved by LEAO, as demonstrated in Figs. 3-5. Together with the experiments above, we validated the performance of LEAO could be comparable to that of hardware AO, and even outperforms it in certain scenarios such as large field-of-view imaging with spatially nonuniform aberrations.

4. Disentanglement assurance

The success of latent factorization depends on the independence of structure and aberration variations in the training triplets. While this is controlled in simulation, real samples may exhibit correlations (e.g., structure-dependent scattering) that could challenge the separation. The manuscript does not discuss measures of disentanglement quality in real experimental data.

Response: We thank the reviewer for this insightful suggestion. First, we would admit that the problem of scattering cannot be fully modelled by LEAO. According to the multilayer scattering model, the intensity field of scattered photons $II\,(ss)$ follows the equation

$$II\,(ss)\,(rr) = \int\int FF(rr')II\,(ii)\,(rr')\,dd3\,rr', \quad (6)$$
$$2\,VV\|rr - rr'\|22$$

where FF is a distribution related to the scattering potential energy, $II\,(ii)$ is the intensity field of the emission fluorescence, and the integral is performed on the whole sample volume range (Zhang, Y. et al. Nature Communications 12, 6391, 2021). The above model is different from an aberration model, where the influence of aberration wavefront on an ideal field $UUiiiiiiiii$ is modelled as phase changes in the pupil plane:

$$UUaaaaaaaaaaaaaaaaa = \mathcal{F}\,{-1}\,\mathcal{F}(UUiiiiiiiii)ee\,iiii\,\phi, \quad (7)$$

where $UUaaaaaaaaaaaaaaaaa$ is the aberrated field, $\mathcal{F}\,{-1}$ and $\mathcal{F}$ are reverse Fourier transform and Fourier transform, and $\phi\phi$ is the aberration wavefront. This means that the complicated change of light propagation path, phase and amplitude in a scattering model cannot be fully described by aberrations in the pupil plane, so the aberration physical model used for LEAO differs from a suitable model for correcting scatterings, which constitutes a limitation of our study, and has been stated in detail in the Discussion section.

Following the reviewer's suggestion, we agree that evaluating the disentanglement quality in experimental data is necessary, though it is not a simple task. We need to collect a special dataset that includes data stacks with the same aberration but different structures, and data stacks with the same structure but different aberrations. Such a dataset does not naturally exist in real experiments, so we have to artificially introduce designed aberrations to ideal samples. Luckily, the system we set up to answer questions 2 and 3 is capable of acquiring such datasets. Specifically, we introduced 2 different aberrations by inserting 2 customized phase masks with distinct patterns, and imaged 4 different regions of a brain slice for each aberration, forming a dataset consisting of 8 data stacks. The t-SNE analysis on the latent features of this dataset exhibits the same characteristics as that on simulated dataset: latent features encoding aberration form clusters depending on aberrations, and latent features encoding structure form clusters depending on structures (Fig. R10). Therefore, LEAO's disentanglement ability on real experimental data is well validated. We have added the corresponding results in the revised version, which helps to validate the design concept of our method.

Fig. R10 (Supplementary Fig. 14) | Disentanglement measurement of

LEAO on experimental data of a mouse brain slice. a, Four different regions from a mouse brain slice. b, Two induced aberration wavefronts from the two designed phase masks. c, t-distributed Stochastic Neighbor Embedding (t-SNE) analysis of latent features extracted from 8 measurements, comprising 4 types of sample structures shown in a, each contaminated by 2 different aberrations shown in b. Scale bar, 20 μm.

Reviewer #3
Remarks to the Author:
The paper presented a deep-learning based image processing method and the method was demonstrated on large volumetric long-duration data collected in diverse biological applications including tracking T cells across a mouse lymph node and imaging through intact skull of mice to compensate aberrations digitally. The neural network method involves latent space training, which is intuitive. However, the technique has its drawbacks and limitations, especially with its versatility when the training is limited to the selected sample structures and some level of retraining is needed when change to a different sample structure.
Response: We thank the reviewer for the time and efforts spent on reviewing this manuscript, and for acknowledging our latent-space-enhanced methodology.
Actually, the first two reviewers also expressed particular concern about the generalizability of our method. To address this, we conducted extensive additional experiments on generalization, demonstrating that LEAO already outperforms DAO even under unseen conditions (Figs. R5, 6). Furthermore, we have added new results to demonstrate that a fast fine-tuning process with less than 5 minutes on small dataset with maximally 50 data stacks can further improve the performance to the level comparable to complete retraining and is easy to implement. All these results demonstrate the practical usability of LEAO in biological experiments.
The reviewer has also offered many constructive advice on the benchmarking of LEAO, and raised several concerns about our experimental performance. We have made our best efforts to answer them point by point below. Here is a brief summary of our response to the reviewer's concern:
Firstly, we have added experiments to further investigate LEAO's performance in terms of higher Zernike modes and larger training datasets. We tested LEAO's performance on data with 41 Zernike modes (i.e., the Zernike modes of the 0~8 radial order, except for piston, tip, tilt and defocus), and the accuracy is consistent with that on aberrations of lower order. As for the training dataset scale, we added experiments and detected no significant performance gain when using more data stacks for training. So, we conclude empirically that 2, 000 is a sufficient number.
Secondly, we conducted simulations to better explain the phase accuracy drop of DAO compared to LEAO. The accuracy of DAO estimation is heavily dependent on the sample structure complexity, the noise level, and the background fluorescence, etc. We used the exact same code on one simple sample and one complicated sample, and found while DAO performance varies prominently, LEAO remains stable, demonstrating its improved robustness over ray-optics-based methods, proving that a wave-optics approach is beneficial to adaptive optics.
Thirdly, as instructed by the reviewer, we adjusted the tiling schemes in Figs. 3 and 4. With a denser tiling, the performance of LEAO improved, and the loss of fidelity the reviewer mentioned in question (4) is solved. We sincerely apologize for our inconsiderable tiling scheme and have re-done all relevant experiments, statistics, figures and videos. For more analysis, please see the response to questions (4) and (6) below.
Other questions were all addressed carefully below. With the help and advice of the reviewer, we believe the added experiments, the revised implementations and the more detailed discussions could more convincingly demonstrate LEAO's accurate, robust, and fast implementation in long-term in vivo imaging.

I have following questions that would like clarification from the authors.
1. For long duration animal imaging, I would assume sample motion as a typical issue. Does random sample motion cause issues to the technique? How it was tackled?
Response: We thank the reviewer for this comment. There are two main types of sample motion: displacement of the field of view (e.g., due to mouse movement during in vivo imaging), and fast movement of the imaging target relative to the field of view (e.g., neutrophil migration in inflammation imaging). The first one could be mitigated by stabilizing the sample as effectively as possible using strong head bar for fixation or putting on anesthesia, without implementing dedicated motion-registration techniques, since addressing this problem is beyond the primary scope of our work. The second one may induce motion blur and degrade imaging quality, if the motion is too fast compared to the imaging frequency. However, light-field imaging is fast compared to other three-

dimensional imaging techniques thanks to its ability to reconstruct one volume from one snapshot within millisecond exposure time. Meanwhile, LEAO can estimate and correct the spatially nonuniform aberrations in post-processing. So, we can achieve high-fidelity imaging even when the sample moves across a long distance.

2. In both figure 4 and 5, authors included images of w/o AO, which still have excellent signal to background / signal to noise ratio, only with distorted PSFs. I would think those images can be processed using some deconvolution-based methods. I would like to see authors comment on the deconvolution-based methods and how LEAO is different and stands out.
Response: We thank the reviewer for this comment. Firstly, we are sorry for causing confusion about the relationship between LEAO and deconvolution-based methods. We would like to clarify that both LEAO and w/o AO results have actually already undergone a deconvolution process to reconstruct volumes from spatial-angular measurements. Specifically, after estimating the aberration wavefront with LEAO, the wavefront will be applied at the pupil plane to generate corrected PSFs (lines 127-129 of the revised manuscript) for reconstruction. In the absence of AO, the wavefront is zero and is used to generate the ideal PSFs for reconstruction. The reconstruction process is based on the phase-space deconvolution method proposed by Lu, Z. et al. in 2019 (Lu, Z. et al. Opt. Express 27, 18131–18145, 2019). In summary, both LEAO and w/o AO results were obtained after deconvolution, as is shown in Fig. R11a.

Fig. R11 (Supplementary Fig. 5) | Deconvolution pipeline and further deblurring results on reconstruction image. a, The deconvolution pipeline of LEAO and w/o AO. w/o AO utilizes ideal 4D phase-space PSFs without aberration, while LEAO puts estimated aberration wavefront into the generation of PSFs. Example PSFs (MIP, center view) of w/o AO and LEAO are shown. With the PSFs, phase-space deconvolution is performed on the aberrated spatial-angular measurements to produce reconstruction results. b, MIPs of reconstruction results on mouse cortex from Fig. 4 by LEAO and w/o AO, and Normalized Blind Deconvolution (NBD) on the reconstruction MIPs. This demonstrates blind deblurring techniques can be applied on the reconstruction results obtained through the pipeline in a to further enhance the image quality. Scale bar, 20 μm.
Secondly, like the reviewer observed, the reconstruction result of w/o AO “still have excellent signal to background / signal to noise ratio, only with distorted PSFs” and “can be processed using some deconvolution-based methods”, due to the aberration-robust nature of light-field imaging. In fact, both w/o AO and LEAO images can be further improved by deconvolution to enhance visual quality, although the true convolution kernels are unknown. To this end, we applied a blind deblurring method termed Normalized Blind Deconvolution (NBD) (Jin, M., Roth, S. & Favaro, P. Computer Vision – ECCV 2018. vol. 11211, 694–711, 2018) on the reconstruction results of LEAO and w/o AO on mouse cortex from Fig. 4, as is shown in Fig. R11b. NBD enhanced the resolution and contrast of both methods, while LEAO still outperformed w/o AO, because some neuronal structures in w/o AO image were too distorted for blind deconvolution methods to restore.

Fig. R12 (Supplementary Fig. 20) | Comparison of LEAO and wide-field blind deconvolution. a, Ground truth sample. b, LEAO reconstruction of aberrated light-field image. c, SSIM evaluation on images in b, d, e, f. d, Wide-field image of aberrated sample. e, NBD result of d. Estimated kernel by NBD is shown in the inset. f, Deconvolution with GT kernel on d. GT kernel is generated using the GT aberration wavefront. Scale bar, 10 μm, 3 μm (insets in e, f).
Thirdly, we also conducted a direct comparison of LEAO on light-field data and blind deconvolution on wide-field data (Fig. R12). The experiment is carried out on 2D neuronal samples. Light-field and wide-field images of the same ground truth sample contaminated with the same ground truth aberration were generated. LEAO image was obtained by correcting and reconstructing the light-field image. NBD image was obtained by performing Normalized Blind Deconvolution on the wide-field image. GT deconvolution image was obtained by performing Richardson-Lucy deconvolution with a ground truth kernel on the wide-field image. Said ground truth kernel was generated via applying the ground truth aberration to the wide-field imaging model. The visual

and statistical results both show that LEAO is significantly better than NBD, and even outperforms the GT deconvolution on wide-field image. This is because wide-field imaging is sensitive to aberration, and blind deconvolution, being a severely ill-posed problem, could not resolve clear structures from the contaminated wide-field image. Therefore, LEAO incorporated with light-field microscope provides a robust fluorescence imaging framework that is resilient to aberrations.

3. LEAO was trained and limited to wavefronts consisting 17 Zernike modes, which only allow the system to process rather smooth aberrations. However, one would imagine scattering as a dominant factor especially for applications such as imaging through an intact skull. Can LEAO deal with data when wavefront distortions containing higher order uncorrectable modes?
Response: We appreciate the reviewer's thoughtful suggestion on making LEAO deal with higher order Zernike modes. Firstly, we would like to explain why we chose 17 Zernike modes for the experiments in our manuscript. After dropping the piston, tilt and defocus modes, which are too low-order and already corrected by our system (Methods), there remain 17 Zernike modes in 0~5 radial orders. Most computational adaptive optics methods also dealt with aberrations under the 5th radial order. For example, Kang, I. et al. used low-order Zernike modes in most of the experiments and only conducted one simulation with high order Zernike modes (the 5th radial order) in their recently proposed self-supervised adaptive optics method (Kang, I., Zhang, Q., Yu, S. X. & Ji, N. Nature Machine Intelligence 6, 714–725, 2024). Guo, M. et al. claimed that the improvements offered by their adaptive optics method past order 4 is negligible (Guo, M. et al. Nature Communications 16, 313, 2025). However, LEAO does have the ability to deal with higher order aberration, as shown in the added experiment below. In this experiment, we simulated aberrations with radial orders of 0~8, a total of 41 Zernike modes (after discarding the piston, tip, tilt and defocus). LEAO restored finer neuronal details compared to DAO (Fig. R13a) on data with aberration of 41 Zernike modes (Fig. R13b). The numerical evaluations demonstrated an SSIM of around 0.8 with residual aberration of ~0.02 σ (Fig. R13c, d), consistent with the LEAO performance on low order aberrations.
Fig. R13 (Supplementary Fig. 22) | Evaluation of LEAO on aberrations with higher Zernike order. a, MIPs of ground truth (first column), LEAO (second column) and DAO (third column). Ground truth and estimated aberration wavefronts are shown in the insets. b, Zernike coefficients of the aberration wavefronts shown in a, in ANSI order. A total of 41 modes were used, corresponding to the 0~8 radial order. c, d, Evaluation of SSIM (c) and normalized residual aberration $\sigma\sigma$ (d) on LEAO and DAO (n = 10). Scale bar, 10 μm.
At last, to answer the reviewer's another concern, we would admit that scattering is a complicated issue which LEAO cannot fully solve. According to the multilayer scattering model, the intensity field of scattered photons $II\ (ss)$ follows the equation

$$II\ (ss)\ (rr) = \frac{1}{2}\frac{1}{VV\|rr - rr'\|22}\int FF(rr')II\ (ii)\ (rr')\ dd3\ rr', \quad (8)$$

where FF is a distribution related to the scattering potential energy, $II\ (ii)$ is the intensity field of the emission fluorescence, and the integral is performed on the whole sample volume range (Zhang, Y. et al. Nature Communications 12, 6391, 2021). The above model is different from an aberration model, where the influence of aberration wavefront on an ideal field $UUiiiiiiiii$ is modelled as phase changes in the pupil plane:

$$UUaaaaaaaaaaaaaaaaa = \mathcal{F}\ -1\ \mathcal{F}(UUiiiiiiiii)ee^{iiii}, \quad (9)$$

where $UUaaaaaaaaaaaaaaaaa$ is the aberrated field, $\mathcal{F}\ -1$ and $\mathcal{F}$ are reverse Fourier transform and Fourier transform, and $\phi\phi$ is the aberration wavefront. This means that the complicated change of light propagation path, phase and amplitude in a scattering model cannot be fully described by aberrations in the pupil plane, so the aberration physical model used for LEAO differs from a suitable model for correcting scatterings. This is a limitation of our study, and has been stated in the Discussion section.

4. In figure 3e, close to the right end, the features look sharper and brighter with better signal without AO when comparing to LEAO. The processed LEAO no longer captures the structures which could be seen originally in the w/o AO. Does this suggest some limitations of LEAO when it can actually make image looks worse? How this affect the data integrity of the LEAO processed images?
Response: We sincerely apologize for producing a less than satisfactory result in Fig. 3 and we have updated the figure with a new tiling scheme (Fig. R14).

Fig. R14 (Fig. 3) | LEAO enables high-resolution imaging of ~5000 T cells across an entire mouse lymph node. a, MIP of T cells in a 4 × 3 mm2 mouse lymph node with LEAO, with DAO and without AO. b, Estimated aberration wavefronts by LEAO and DAO. The whole FOV was divided into 10 × 7 tiles. c, d, e, Enlarged images of the areas marked by white dashed box in a. f, Intensity profiles along the lines marked by white arrow in e. LEAO can separate adjacent T cells distorted by aberration with higher peak values, while DAO and w/o AO reconstructions cannot. g, Directional MIPs of the area marked by yellow dashed box in a. h, Color-coded temporal tracks of T cells across a duration of 38 minutes estimated from results with LEAO, with DAO and without AO. i, A representative trajectory of a single cell from LEAO, overlaid on the timelapse MIPs. The region is marked by white dashed box in h. j, Identified trajectory number obtained by the methods with LEAO, with DAO and without AO. k, l, Histogram of track mean velocity (k) and track length (l) obtained by LEAO. Scale bar, 140 μm (a, h), 70 μm (c, d, g, i), 20 μm (e).

Previously, we did not take full notice of the importance of spatially varying aberration. The degradation in reconstruction quality is due to the sparse tiling scheme adopted for this figure during our initial processing. We have corrected it and re-done the whole experiment. In our previous experiment, for memory efficient computation, we divided the whole field of view into 2×2 tiles, which at first glance is enough for aberration correction, but lacks accuracy especially around the peripheral regions. The problem the reviewer pointed out is a consequence of the tiling scheme. At the right end of previous Fig. 3e, the actual aberration is relatively small. If we apply the large aberration wavefront estimated mainly from the central region, the LEAO-processed image will become worse than the one without AO. We felt deeply sorry for this mistake and re-performed the experiment with a 10×7 tiling scheme. Now in our updated Fig. 3, the performance of LEAO in the region of interest improved with better contrast and sharper features (Fig. R14g). We also re-designed some panels in Fig. 3 with the new data to better show the advantage of LEAO over DAO.

5. In Figure 1f and 4c, the wavefront generated by DAO seems to have the same shape to the ground truth wavefront, but only off by amplitudes (in a consistent way). Is this discrepancy due to any fundamental limitation of DAO or it is more to do with how it was set up and operated? As the latter reason can affect the fairness of the comparison.

Response: We thank the reviewer for this comment. We have revised the two mentioned parts carefully. For Fig. 1f, we sincerely apologize for the mistake we made during figure composing. We forgot to multiply the DAO phase by a calibrated coefficient when outputting the visualization, resulting in the off-amplitude representation. The coefficient is used to correct the amplitude after the integration process that generates DAO phase from DAO shift maps. It differs in different systems. We have now corrected this mistake (Fig. R15f (Fig. 1f in the revised manuscript), Fig. R16a (Supplementary Fig. 6 in the revised manuscript)). However, the relevant statistics in the original manuscript were conducted correctly with the calibrated coefficient, so the graphical mistake did not affect the accuracy of the metrics.

Fig. R15 (Fig. 1) | Methodology and performance of LEAO. a, b, c, The ideal model (a), ray-optics model (b) and wave-optics model (c) of imaging wavefront affected by aberrations. d, Framework of LEAO. Through optimization in the latent space using latent loss, feature distances are minimized for inputs sharing the same aberration or structure, and maximized for those with different aberrations or structures. e, t-distributed Stochastic Neighbor Embedding (t-SNE) analysis of latent features extracted from 9 measurements, comprising 3 types of sample structures, each contaminated by 3 different aberrations. f, Two directional maximum intensity projection (MIP) of ER images without AO (first column), with DAO (second column), and with LEAO (third column). Zoomed-in regions of the yellow solid box are shown on the right bottom. Regions corresponding to the 30° projection are marked by yellow dashed line. Estimated aberration wavefronts are displayed in the insets. The ground truth image is shown in the right column. g, Peak signal-to-noise ratio (PSNR) of images obtained by methods without AO, with DAO and with LEAO on three types of structures including cell membrane, ER and MT (n = 10). h, Normalized residual aberration $\sigma\sigma$ (Methods) estimated by DAO and LEAO (n = 10). Boxplot format: center line, medians; limits, 75% and 25%; whiskers, the larger value between the largest data point and the 75th percentiles plus 1.5× the interquartile range (IQR), and the smaller value between the smallest data point and the 25th percentiles minus 1.5× the IQR; outliers, data points larger than the upper whisker or smaller than the lower whisker. Scale bar, 20 μm (f), 4 μm (zoom-in regions in f).

Fig. R16 (Supplementary Fig. 6) | Evaluation of LEAO on data of punctate

and tubular structure. a, Two directional MIPs of cell membrane (first row) and MT (second row) images without AO (first column), with DAO (second column), and with LEAO (third column). Zoomed-in regions of the yellow solid box are shown on the right bottom. Regions corresponding to the 30°projection are marked by yellow dashed line. Estimated aberration wavefronts are displayed in the insets. The ground truth images are shown in the right column. Scale bar, 30 μm, 10 μm (zoom-in). b, c, SSIM (b) and PSNR (c) of images obtained by methods without AO, with DAO and with LEAO on three types of structures including cell membrane, ER and MT (n = 10). d, Normalized residual $\sigma\sigma$ estimated by DAO and LEAO (n = 10). Boxplot format: center line, medians; limits, 75% and 25%; whiskers, the larger value between the largest data point and the 75th percentiles plus 1.5× the interquartile range (IQR), and the smaller value between the smallest data point and the 25th percentiles minus 1.5× the IQR; outliers, data points larger than the upper whisker or smaller than the lower whisker.

As for Fig. 4c, we have already multiplied the DAO phases by a correct coefficient calibrated by simulations. Because there is no ground truth in real experiments, we cannot conduct calibration with this sample. After calibration, there may still exists a discrepancy between DAO phases and ground truth phases. This discrepancy is due to the ray-optics nature of DAO. We conducted a new simulation regarding this issue. Using the same open-source code (https://github.com/bbncWLG/DAOSLIMIT) provided in the original manuscript of DAO (Wu, J. et al. Cell 184, 3318-3332.e17, 2021), the phases estimated by DAO on fluorescent beads and ER are different, though the two samples were contaminated with the same aberration wavefront, assuming the same optical system. DAO performs disparity estimation by aligning every angular measurement with the center angle image and outputs a shift map. During iterative process, the shift map gets constantly updated. When the algorithm reaches a maximum iteration, the reconstruction is complete, yielding a final shift map. The shift map has to be integrated along two angular dimensions and multiplied by a calibrated coefficient to get an aberration phase estimation. Then to improve the resemblance of the integrated phase to the ground truth, we fit the phase by Zernike polynomials, resulting in a smooth phase consisting of multiple Zernike modes. In this process, the shift map may not be accurately estimated, especially with complicated structures, noise and background fluorescence. In Fig. R16, the fluorescent beads are simple, clean, background-free structures simulated using MATLAB script. The ER sample is real data captured by microscopy, downloaded from open-source datasets (https://www.allencell.org/data-downloading.html#DownloadImageData). It possesses higher structure complexity, more background fluorescence, and lower signal-to-noise ratio, leading to a wrong shift map estimation by DAO. This is the major problem affecting the accuracy of DAO. The likeliness of failure increases with aberration magnitude and sample complexity. LEAO can effectively solve this problem and alleviate this uncertainty with better accuracy of aberration estimation.

Fig. R17 (Supplementary Fig. 2) | The estimated phases by DAO and LEAO on two samples with different complexity. a, Both DAO and LEAO accurately yield a phase highly resembling the ground truth. b, DAO fails to accurately estimate the shift map of ER with more complicated structure, noise distribution and background fluorescence, leading to off-amplitude phase estimation, while LEAO preserves the accuracy.

Furthermore, we would like to emphasize that the reconstruction process of DAO does not require the integrated phase. No matter what phase is obtained by integrating the shift maps estimated by DAO, the reconstruction output by DAO will not change. Judging from the degraded image quality in Fig. 1f and 4c, DAO has not estimated the aberration phases as accurately as LEAO.

6. I do not fully understand Figure 4 when a 4.6 mm x 3.4 mm x 0.6 mm volumetric imaging is processed on 3x5 spatial tiles. Does this mean that for each spatial tiles, it is much wider in x direction but much narrower in y direction? Does this also mean that the isoplanatic patch is in mm level? Does it also mean that there is no change of aberration throughout the 600 um imaging depth? This sounds a bit too large to me especially this demonstration imaged dynamic activations in mouse cortex and green fluorescence was used.

Response: We thank the reviewer for this comment and apologize for the misunderstanding caused by our inaccurate description in the main text. In our previous experiment, the 3×5 phases correspond to only the central areas of the entire field of view, spanning around 2×3.3 mm2 . Also, we made a typo where it should be 3.4×4.6 mm2 , not 4.6×3.4 mm2 . In the meantime, we agree with the reviewer that the previous

tiling is not dense enough for spatially nonuniform aberrations in this case. We have divided the mouse brain into denser patches and replaced all figures and statistics to alleviate the reviewer's concern. For selected regions, multiple phases were used for correction (Fig. 4e, f), leading to improved statistics (Fig. 4h-j).
As for the aberrations along axial direction, we would admit that our aberration estimation is depth-irrelevant, because in essence LEAO takes angular projections of three-dimensional data as input, making it impossible to differentiate between different depths. Meanwhile, the 600 μm is the axial range of the point-spread-function used for reconstruction. We made the range large enough to make sure no structure is left out. Moreover, the detection NA of this system is 0.5, which will also increase the aberration robustness across depths.
Fig. R18 (Fig. 4) | LEAO enables high-fidelity mesoscale recording of multiregional neural activities in mouse cortex with spatially nonuniform aberrations. a, MIPs of the Standard Deviation (STD) volume of a 4.6 × 3.4 × 0.6 mm3 mouse cortex with LEAO, with DAO and without AO. b, Regions of the area marked by white box I in a, displayed as two directional MIPs. c, Estimated aberration wavefronts by DAO and LEAO on the 10 × 7 spatial tiles, and by LEAO (untiled) on the whole FOV. d, The representative neuronal patterns from different spatial regions processed without AO, with LEAO (untiled) and with LEAO. e, Enlarged regions of the area marked by white boxes II and III in a. The regions marked by red line in area II correspond to the right-bottom regions marked by red line in d. The regions marked by yellow line in area III correspond to the central regions marked by yellow line in d. Aberration wavefronts are shown in the insets. f, Two directional MIPs of STD volumes over a time of 1,122.5 s, obtained by methods without AO and with LEAO, respectively. Five neurons are manually selected and marked by white arrow. Estimated aberration wavefronts, corresponding Fourier spectrums and enlarged regions are shown in the insets. g, $\Delta FF/FF$ traces of the neurons in f. h, Identified neuron number from the area in f by CNMF algorithm. i, Histogram of extracted spikes from the area in f by CNMF algorithm. j, All neuronal traces extracted from the area in f. Scale bar, 140 μm (a, b, e, f), 40 μm (d, zoom-in regions in b, f).

Do the authors think the aberrations were mainly sample-induced or optical system-induced?
Response: We think the aberrations were mainly sample-induced. The mice from Fig. 4a-e and f-j are two different mice imaged by the same system. As is shown in Fig. R19, the estimated phases vary significantly from one another. This suggests that the aberration changes with sample. We have added corresponding results in the revised manuscript to clarify this point.

Fig. R19 (Supplementary Fig. 15) | Estimated phases by LEAO on two mice imaged by the same system. Mouse 1 is the source of Fig. 4a-e. Mouse 2 is the source of Fig. 4f-j.

In 4c, it seems to suggest that the wavefront aberration is huge, with a peak to valley amplitude of 9 wavelengths. The fluorescence intensity, on the other hand, still seems to be descent despite the large aberration. I would like to see the authors comments on this.
Response: We thank the reviewer for raising this interesting question. Robustness to aberration is intrinsically one of the advantages of light-field (LF) imaging. We chose to build LEAO on light-field microscopy not only because it is able to provide spatial-angular information as important physical priors to estimate aberrations, but also due to its intrinsic capability to maintain the fluorescence intensity with the existence of strong aberrations, unlike common wide-field (WF) microscopy with a much higher aberration sensitivity. To prove this, we conducted simulations on the PSFs of both the light-field microscopy and the wide-field microscopy sharing the same set of system parameters (Fig. R20 (Supplementary Fig. 19 in the revised manuscript). At lower Zernike modes (r = 2, 3), the peak intensity of wide-field microscopy quickly drops with increasing aberration magnitude, whereas the peak intensity of light-field microscopy experiences only a slight decrease. The same simulation is repeated for higher Zernike modes (r = 5) and the result is similar. This experiment has demonstrated the robustness of light-field imaging to the increasing aberration magnitude. This is also one of the reasons that LEAO's performance surpasses that of CoCoA, which is a WF-based method.

Fig. R20 (Supplementary Fig. 19) | Comparison of wide-field and light-field PSFs' intensity robustness to aberrations. a, b, Added aberration wavefronts (first row), MIPs of simulated WF PSFs (second row), and MIPs of the center angular component of simulated LF PSFs (third row) for Zernike modes of r = 2, 3 (a) and r = 5 (b). The aberration magnitude is 1 $\lambda\lambda$. c, d, The curve of normalized mean intensity of WF and LF PSFs with increasing aberration magnitude from 0 to 6 $\lambda\lambda$ for Zernike modes of r = 2, 3 (c) and r = 5 (d). The mean intensity (>99.9999 %) of a PSF is computed as the mean of all pixels exceeding the 99.9999 % intensity threshold in said PSF. Then this value is normalized so that it is 1 when without aberration.

7. In the method section, the authors suggested that a total of 17 Zernike modes were involved and a total of 2000 dataset were used for training. If we say each Zernike modes can be either positive and negative, the total combinations of these 17 Zernike modes are 217. 2000 dataset sounds way too small to me. I would like the authors comments on this.
Response: We thank the reviewer for this constructive advice. First, we would like to explain the generation of Zernike coefficients in the training dataset. Like the reviewer stated, a total of 17 Zernike modes will be used when generating Zernike coefficients. For each mode, the corresponding coefficient $cckk$ is sampled from a uniform distribution $cckk \sim UU([aakk\ ,\ bbkk\ ])$ ($1 \le kk \le 21$, in ANSI ordering), and the coefficient for piston, tilt and defocus modes are set to 0 as they were already corrected during system setup. In theory there will be infinite combinations of these 17 Zernike modes because their coefficients are continuous. Since we cannot generate infinite training data, we have to determine the optimal data stack number empirically, and 2000 is a number chosen that is sufficient for training. We are deeply sorry that we previously did not include experiments to validate our choice of 2000 data stacks. Now with the constructive advice from the reviewer, we conducted an experiment in which LEAO models trained by increasing number of data stacks are tested on the same test dataset. As shown in Fig. R21, there is no significant performance gain when increasing the dataset number, and the reconstruction quality seems similar for any dataset number larger than 2000. We think this is mainly because the aberration information is physically embedded in the spatial-angular measurements of light field. Therefore, it's not an ill-posed problem for neural network to fit, thus does not require a large number of training data.

Fig. R21 (Supplementary Fig. 25) | Performance of LEAO with increasing number of training data stacks. a, Two directional MIPs obtained by LEAO models trained with 2000, 4000, 6000, 8000 and 10000 data stacks. GT is displayed at the left top for reference. Estimated aberration wavefronts are shown in the insets. b, c, Evaluation of normalized residual aberration $\sigma\sigma$ (b) and SSIM (c) on the same test dataset (n = 10). The evaluation validated that our choice of 2000 data stacks is sufficient for the training. Boxplot format: center line, medians; limits, 75% and 25%; whiskers, the larger value between the largest data point and the 75th percentiles plus 1.5× the interquartile range (IQR), and the smaller value between the smallest data point and the 25th percentiles minus 1.5× the IQR; outliers, data points larger than the upper whisker or smaller than the lower whisker. Scale bar, 20 μm.

Remarks on code availability:
The programme seems to be documented with clear instructions on how to install packages and run training. Examples were also provided. However, as the training requires GPUs, I was unable to test the programme.
Response: We appreciate that the reviewer has carefully examined our open-source code and acknowledged our efforts to provide detailed instructions and example results. We are sorry that the majority of the functionality is accessible only with GPUs. However, we have sent the code to different users for multiple times of testing and we believe it is readily available.

Version 1:

Reviewer comments:

Reviewer #1

(Remarks to the Author)
The authors have addressed all my comments in the last round of review, and I don't have any other concerns.

(Remarks on code availability)

Reviewer #3

(Remarks to the Author)
Sorry for the slightly delayed comments during this festive season. I would like to thank the authors for the 36-page-long response letter.

Most of my comments were properly addressed, and the authors also modified and corrected their experimental results based on my queries.

However, for the comment regarding network translatability and generalisability, it was still not clear to me how a network trained on one experimental setting on one type of sample can be easily used to process data generated using a different experimental setting on a different type of sample. The authors suggested a fast fine-tuning process that only requires 50 sets of data and five minutes of training. However, I would be surprised if it works when the optical system is designed differently and images a totally different type of sample. I would like the authors to correct me if otherwise. I would also hope the authors would make it clear in the paper whether the method needs to be retrained for each imaging scenario.

For the comment about the sample motion, the authors suggested that sample motion is not an issue for their experimental methodology. However, considering sample motion is a typical issue for long duration in-vivo imaging, I would hope the authors to make it clear in the paper that their method does not have a mechanism to correct sample motions.

(Remarks on code availability)

Author Rebuttal letter:

Response to Reviewers

We are grateful for the reviewers' insightful comments and suggestions, which have substantially improved our manuscript. We believe we have addressed all of the major and minor comments. The revised and added texts have been highlighted in red in the manuscript and supplementary materials. Please find below a point-by-point response to each comment.

Reviewer #1

Remarks to the Author:
The authors have addressed all my comments in the last round of review, and I don't have any other concerns.
Response: We thank the reviewer for the previous helpful suggestions and are glad that our reply was satisfactory.

Reviewer #3

Remarks to the Author:
Sorry for the slightly delayed comments during this festive season. I would like to thank the authors for the 36-page-long response letter.
Most of my comments were properly addressed, and the authors also modified and corrected their experimental results based on my queries.
However, for the comment regarding network translatability and generalisability, it was still not clear to me how a network trained on one experimental setting on one type of sample can be easily used to process data generated using a different experimental setting on a different type of sample. The authors suggested a fast fine-tuning process that only requires 50 sets of data and five minutes of training. However, I would be surprised if it works when the optical system is designed differently and images a totally different type of sample. I would like the authors to correct me if otherwise.
Response: We thank the reviewer for raising this concern. The fast fine-tuning process

mentioned was indeed conducted on different types of sample and differently designed systems. After pointed out by the reviewer, we realized that we only showed the fine-tuning results but ignored the reason and support as to why it can be carried out successfully. To alleviate the possible doubt, we conducted an experiment to unveil the mechanism behind this performance. An intuitive explanation would be that LEAO's specially designed architecture and training paradigm encouraged the formation of a disentangled latent space beneficial to the generalization ability. To confirm this, we compared LEAO with the vanilla regressor, which maps the spatial-angular measurements from light-field microscopy directly to the aberrations (Fig. R1).

Fig. R1 (Supplementary Fig. 19) | Ablation study to evaluate the transfer-learning capability of LEAO compared with a vanilla regressor. a, The architecture of the vanilla regressor and LEAO. b, Convergence curves of normalized residual aberration $\sigma\sigma$ versus the number of iterations on a membrane test dataset, by the vanilla regressor and LEAO, respectively. For the vanilla regressor, the model first trained on simulated neuron dataset and then finetuned on membrane data (red line) cannot reach the same accuracy level as the model trained on membrane dataset itself (orange line). For LEAO, the model trained on membrane dataset took ~1333.3 minutes to converge, while the finetuned model converged to the same accuracy level in ~4.5 minutes. c, Boxplots showing SSIM and normalized residual aberration $\sigma\sigma$ obtained by different vanilla regressor models and different LEAO models (n = 10). All used models were converged. Boxplot format: center line, medians; limits, 75% and 25%; whiskers, the larger value between the largest data point and the 75th percentiles plus 1.5× the interquartile range (IQR), and the smaller value between the smallest data point and the 25th percentiles minus 1.5× the IQR; outliers, data points larger than the upper whisker or smaller than the lower whisker. d-f, The representative MIPs for the ground truth (d), the results with different vanilla regressor models (e), and the results with different LEAO models (f). Ground truth and estimated aberration wavefronts are shown in the insets. Scale bar, 40 μm, 10 μm (zoom-in regions).

The vanilla regressor's architecture is the same as LEAO except for the discarded decoder that constitutes the auto-encoder branch (Fig. R1a). Without this branch, the vanilla regressor does not possess a meaningful latent space. We trained the vanilla regressor on the same dataset as LEAO, without implementing the data triplet strategy designed for the disentanglement of the latent space. When trained on membrane structures, the vanilla regressor took similar time as LEAO to converge, but reached worse test accuracy. When fine-tuned with a pre-trained model trained on neuronal structures, the vanilla regressor could not achieve the same test accuracy as that trained with membrane structures from scratch (Fig. R1b). Further statistical analyses on converged models confirmed that the direct generalization of the vanilla regressor across different sample structures was much worse than LEAO, and that the fast fine-tuning of the vanilla regressor with a small dataset could not restore the accuracy as well as LEAO (Fig. R1c). The reconstruction image quality was also in accordance with the above observation (Fig. R1d-f). The restored image by the vanilla regressor trained on membrane itself already showed slight distortion compared to LEAO. Direct generalization from neuronal structures or fast fine-tuning on a small dataset of membrane by vanilla regressors could not produce images with comparable quality as that from the model trained from scratch. In conclusion, we resolved the underlying key to LEAO's generalization ability and proved that the translatability of LEAO is markedly enhanced by its latent space disentangling scheme which distills aberration priors from unwanted information such as structure patterns.

Meanwhile, we would like to explain the intentions and reasonings behind our two fast fine-tuning experiments. Due to the unlimited possible designs of optical systems and patterns of sample structures, we would not be able to test the amount of data and time required to achieve satisfactory fine-tuning on all of them. We believe the required data and time would increase with the level of discrepancy between the pre-trained model and the target model, as the reviewer would expect, and we have added this explanation into the Discussion section (Lines 388-390). However, the two fine-tuning experiments could offer guidance on approximately how much cost should be invested in transfer learning, and could prove the strong translatability of LEAO.

I would also hope the authors would make it clear in the paper whether the method needs to be retrained for each imaging scenario.

Response: We thank the reviewer for this advice. Although we stated that the direct

generalization of LEAO could already surpass DAO, in reality, to ensure performance, for each imaging scenario we either trained the method from scratch or fine-tuned it with a pre-trained model. We have added this clarification in the Discussion section (Lines 353-355). We have also listed the training details for every experiment, including whether transfer learning was conducted, in Supplementary Table 2.

For the comment about the sample motion, the authors suggested that sample motion is not an issue for their experimental methodology. However, considering sample motion is a typical issue for long duration in-vivo imaging, I would hope the authors to make it clear in the paper that their method does not have a mechanism to correct sample motions.
Response: We thank the reviewer for this thoughtful suggestion to aid the readers. We have added in the Discussion that we do not have a mechanism to correct sample motions (Lines 401-402).

Reviewer 1 comments on Reviewer 2's concerns:

1. Dependence on the generalization of the estimator
The authors justified the generalization ability of LEAO by conducting two additional experiments – one for unseen samples and one for unseen systems. In both cases, while there are still residual aberrations, LEAO shows superior performance over the current DAO method, and further fine-tuning or transferring learning helps further improve LEAO performance. I think these results have mostly addressed the generalization concern, and of course, their conclusions make sense to me, as do most DL methods for cross-sample/cross-system.
Response: We thank the reviewer for acknowledging our efforts to address the generalization ability.

2. Simulation-to-real gap
The authors explained that they have tried their best to mimic experimental conditions and validated the performance with a new experiment by physically introducing aberrations with phase masks. While I appreciate the authors' efforts to better understand the simulation-to-real gap and I am convinced by the results to some extent with this specially designed experiment, I somehow feel the concern about the simulation-to-real gap is unlikely to be fully eliminated in realistic scenarios (e.g., complex scattering effect). It is good to see the authors have included a discussion on it in the text for better justification (Lines 381-384), but it might be better if the authors make it as general as model mismatch, rather than only scattering – scattering is one example.
Response: We thank the reviewer for this advice. We admit that the simulation-to-real gap cannot be completely eliminated. Although we have tried our best to accommodate LEAO to various experimental factors, a mismatch of simulated and experimental conditions would still exist. Degradations caused by factors outside of LEAO's design cannot be corrected. For example, it cannot fully recover resolution or imaging depth loss due to scattering, because the scattering model is different from our physical model of aberration formation. This issue may be addressed by adopting multi-photon excitation or imaging strategies that incorporate scattering models. Also, LEAO does not correct degradations that cannot be modeled as phase changes in the pupil plane. For example, motion blur caused by sample movement or image degradation resulting from evaporation in water-immersion objectives falls outside the correction capability of LEAO. As instructed by the reviewer, we added these statements in the Discussion section (Lines 392-397).

3. No explicit benchmark against closed-loop hardware AO comparison
Instead of a direct comparison to hardware-based closed-loop AO, the authors used the same experiment with physical masks in Question #2 and additional simulations of closed-loop AO. While these experiments are not fully equivalent to hardware AO, I feel they logically address the concerns to some extent, and would not ask more especially considering the ability to correct spatially-varying aberrations otherwise not practical for hardware AO.
Response: We deeply appreciate the reviewer's understanding of the difficulty of implementing spatially-varying closed-loop hardware AO and our logic to equivalently address this problem. In our experiment with designed phase masks, we proved LEAO's resemblance to experimental data corrected by removing the introduced phase mask. In the simulation comparison, we proved that LEAO is comparable with closed-loop

hardware AO and holds superiority when processing spatially-varying data.

4. Disentanglement assurance
Similar to the above concern about the simulation-to-real gap, I think the authors should admit this point as they have done in the Discussion section.
Response: We thank the reviewer for this advice. We admit that structure-dependent distortions may interfere with the disentanglement and have addressed this issue in the Discussion section (Lines 405-407).

Version 2:

Reviewer comments:

Reviewer #3

(Remarks to the Author)
I would like to thank the authors for their response. I am happy to say that all my comments were properly addressed.

(Remarks on code availability)